Fermilab FERMILAB-THESIS-1998-39

# Measurement of Bottom Quark-Antiquark Rapidity Correlations in Proton-Antiproton Collisions at $\sqrt{s} = 1.8$ TeV

By

**James D. Olsen**

A dissertation submitted in partial fulfillment of the requirements for the degree of

Doctor of Philosophy

(Physics)

at the

**UNIVERSITY OF WISCONSIN – MADISON**

1998

# The CDF Collaboration

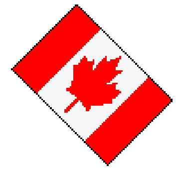

Argonne, Bologna, Brandeis,
UCLA, Chicago, Duke, FNAL,
Florida, Frascati, Geneva,
Harvard, Hiroshima, Illinois,
IPP/Canada, Johns Hopkins,
Karlsruhe, KEK, LBL, MIT,
Michigan, Michigan State, New
Mexico, Ohio, Osaka City, Padova,
Pennsylvania, Pisa, Pittsburgh,
Purdue, Rochester, Rockefeller,
Rutgers, Academia Sinica, Texas
A&M, Texas Tech, Tsukuba,
Tufts, Wisconsin, Yale

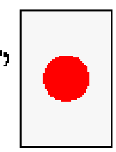

460+ people, 39 institutions,
7 countries

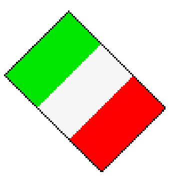

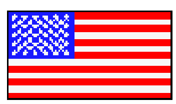

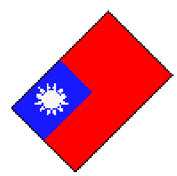

# Abstract

I report the first measurement of $b\bar{b}$ rapidity correlations in $p\bar{p}$ collisions at $\sqrt{s} = 1.8\,\mathrm{TeV}$. Events are selected with a high transverse momentum muon correlated with a jet, and a second jet associated with a secondary decay vertex. The $b\bar{b}$ fraction is determined by fitting the muon momentum transverse to the muon-jet axis and the transverse decay length of the secondary vertex. The ratio of forward to central $b\bar{b}$ production is measured to be $0.361 \pm 0.033\,(\mathrm{stat})^{+0.015}_{-0.031}\,(\mathrm{syst})$, in good agreement with the next-to-leading order QCD prediction using the MRSA$'$ parton distribution set, $0.338^{+0.014}_{-0.097}$.

# Acknowledgements

I would like to thank my advisor, Duncan Carlsmith, for recommending a thesis topic that turned out to be much more interesting than I thought it would, and for allowing me the freedom to pursue my own ideas. I would also like to thank Lee Pondrom for his constant support and interest in this thesis, and for always having an open door for a physics discussion on any topic. I would not have any data if it were not for the tireless efforts of George Ott, Bob Handler, and Joe Steele, who kept the detector up and running. Chris Wendt, in the early years, and more recently Sergei Lusin provided support, expertise, and amusement. Jim Bellinger deserves many thanks for assisting me with the (seemingly) infinite number of tape mounts needed to perform the luminosity calculation in Chapter 4.

Many thanks go to all of the members of the CDF $B$ physics group who have commented on, and constructively criticized, the work presented in this thesis. Several physicists at Fermilab were critical to the success of this analysis. I would like to thank Paris Sphicas for his crucial support in the very early days, and for his continued interest in my career as a physicist. I would also like to thank Joe Kroll, who helped me in many different ways, not least of which was introducing me to my future boss. Jonathan Lewis deserves a great deal of credit for many of the good ideas in this thesis (the bad ones are all mine!).

On a personal note, I want to thank my friend, Brendan Bevensee, who I have known since sophomore physics and was a fellow collaborator on CDF, for all of the fun times and physics conversations. Finally, to my wife Jen, who has been with me longer than physics, this is just as much your thesis as it is mine, and I dedicate it to you.

# List of Figures

# List of Tables

# Contents

# Chapter 1

# Introduction and Overview

Over the past century, scattering experiments at ever-higher energies have produced a wealth of information on the fundamental constituents of matter and their interactions. Just as an optical microscope reveals fine detail hidden from the human eye, the kinematic and angular distributions of particles scattered in high energy collisions can reveal details of the target structure not discernable with lower energy projectiles. Referring to the $\alpha$-particle scattering experiments of Geiger and Marsden [1], Ernest Rutherford wrote in the introduction to his classic 1911 paper on the structure of the atom [2]:

> "...It should be possible from a close study of the nature of the deflexion to form some idea of the constitution of the atom to produce the effects observed. In fact, the scattering of high-speed charged particles by the atoms of matter is one of the most promising methods of attack of this problem."

By observing the frequency of large angle scattering of 8 MeV $\alpha$-particles from a thin metal foil, Rutherford deduced that the atom consisted of a dense positive core (nucleus) surrounded by a diffuse cloud of negative charge, and set the template for future scattering experiments investigating the fundamental structure of nature.

A half century after Rutherford, a series of electron-proton scattering experiments at the Stanford Linear Accelerator Center (SLAC) provided the first conclusive evidence of proton substructure. Using 185 MeV electrons elastically scattered from a hydrogen target, McAllister and Hofstadter [3] observed deviations from the Mott formula[1] indicating a proton rms size comparable to the de Broglie wavelength of the beam electrons ($10^{-13}$ cm). By 1969, the Stanford accelerator was producing electron beams up to 18 GeV, initiating a new class of experiments referred to as "deep inelastic scattering". By studying the kinematic and angular distributions of inelastically scattered electrons, the MIT-SLAC collaboration [4] confirmed the "scaling"[2] behavior of the proton structure function predicted by Bjorken's current algebra analysis of lepton-hadron scattering [5]. Independently, Feynman provided a simple explanation of scaling in terms of pointlike constituents (partons) carrying a fraction $x$ of the proton's momentum [6]. Partons were eventually identified with the quarks and gluons of quantum chromodynamics (QCD), leading to the currently accepted picture of a proton consisting of three valence quarks plus a "sea" of gluons and quark-antiquark pairs.

High energy collisions have also provided information on the fundamental interactions through the production of previously unobserved particles. The advent of proton synchrotrons in the 1950's (in particular, the Bevatron at Berkeley and the Cosmotron at Brookhaven) led to a proliferation of new particles, some with lifetimes so short ($10^{-25}$ s) they could only be detected in the form of "resonances" in the scattering cross section[3]. Attempts to organize the "zoo" of new particles led to the identification of conserved quantities, which, from Noether's theorem, revealed the internal symmetries of the underlying interactions. The ultimate result was the classification of all known hadrons into a multiplet structure based on the flavor SU(3) symmetry group, whose fundamental representations are the three light quarks: up ($u$), down ($d$), and strange ($s$) [8, 9].

[1]The Mott cross section is an extension of the Rutherford scattering formula for collisions involving particles with nonzero magnetic moments.

[2]Scaling refers to the high energy dependence of the proton structure function on the ratio of the energy loss by the electron and the square of the four-momentum transferred in the collision, rather than on either variable separately.

[3]For a discussion of this period, including reprints of major articles, see Ref. [7].

In 1979, the study of event topology in electron-positron ($e^+e^-$) annihilation at the 30 GeV Petra collider led to the discovery of the gluon and the firm establishment of QCD as the theory of strong interactions [10]. Four years later, the discovery of the $W^\pm$ [11, 12] and $Z^0$ [13, 14] intermediate vector gauge bosons in 540 GeV proton-antiproton ($p\bar{p}$) collisions at the CERN Superproton Synchrotron ($Sp\bar{p}S$) dramatically confirmed the validity of the electroweak theory developed independently by Glashow [15], Weinberg [16], and Salam [17] (GWS). With this discovery, the Standard Model of particle physics, comprising the GWS and QCD theories, was established. The predictions of the Standard Model have since stood the test of time. However, the theory is known to be incomplete, most notably in the area of fundamental fermion masses. The primary goal of the future Large Hadron Collider (LHC) is to verify the theory of spontaneous symmetry breaking (Higgs mechanism) believed to be responsible for the mass splittings of the quarks and leptons. Thus, throughout the current century, and into the next, the experimental technique of high energy scattering represents a powerful tool for the study of the fundamental particles and interactions.

Following in the tradition outlined above, in this thesis I describe a measurment of the angular correlation between bottom quark-antiquark ($b\bar{b}$) pairs produced in $p\bar{p}$ collisions at a center-of-mass energy of 1.8 TeV. This measurement represents the first direct test of the strong rapidity correlation predicted by QCD, which plays a central role in the design of small angle forward spectrometers seeking to study $CP$ violation in $b$ decays. In addition, measurement of the $b$ quark production cross section at small angles with respect to the colliding beams can play an indirect role in determining whether quarks themselves are composite objects. In this opening chapter I first discuss in more detail the motivation behind the measurement, and then close with an overview of the analysis method and organization of the thesis.

## 1.1 Introduction

The study of $b\bar{b}$ production in high energy $p\bar{p}$ collisions has proven to be a valuable tool for the quantitative testing of perturbative QCD. The $b$ quark mass is considered large enough[4] that the production cross section can be expressed as a series expansion in the strong coupling $\alpha_s$; while the large semileptonic branching fraction (10%) and long lifetime ($c\tau \approx 470\mu$m) of $b$ hadrons provide convenient experimental signatures that serve to separate $b\bar{b}$ production from the large QCD jet backgrounds at a hadron collider. In this thesis I present the first measurement of $b\bar{b}$ rapidity ($y$) correlations in $p\bar{p}$ collisions at $\sqrt{s} = 1.8\,\mathrm{TeV}$. Specifically, I measure the ratio [5]

$$R \equiv \frac{\sigma(p\bar{p} \rightarrow b_1 b_2 X;\ 2.0 < |y_{b_1}| < 2.6)}{\sigma(p\bar{p} \rightarrow b_1 b_2 X;\ |y_{b_1}| < 0.6)}, \tag{1.1}$$

given that the second quark $b_2$ is observed in the central rapidity range $|y_{b_2}| < 1.5$, and both quarks have transverse momentum $p_T > 25\,\mathrm{GeV}/c$ and are separated by an azimuthal opening angle $> 60°$. The small angle (large rapidity) region is referred to as "forward", while the angular region $|y| \approx 0$ is referred to as "central". Table 1.1 summarizes the forward and central cross section definitions. By measuring the ratio of cross sections I am able to significantly reduce the experimental uncertainty, while retaining the relevant physics information on the shape of the rapidity distribution.

[4]What constitutes a "large enough" mass will be explained in Sec. 2.1.1.

[5]Since charge identification is not performed, I will refer to the $b\bar{b}$ pair as $b_1$ and $b_2$ whenever specific cuts are given.

**Cross Section Definition**

| Parameter | Forward | Central |
|---|---|---|
| $p_T^{b_1,b_2}$ | $> 25\,\mathrm{GeV}/c$ | $> 25\,\mathrm{GeV}/c$ |
| $\lvert y_{b_1}\rvert$ | $(2.0, 2.6)$ | $< 0.6$ |
| $\lvert y_{b_2}\rvert$ | $< 1.5$ | $< 1.5$ |
| $\Delta\phi(b_1 b_2)$ | $> 60°$ | $> 60°$ |

Table 1.1: Summary of the forward and central cross section definitions.

### 1.1.1 Motivation

In the absence of a large contribution of collinear $b\bar{b}$ pairs from the gluon splitting process (Sec. 2.1), the rapidity correlation $\Delta y = y_b - y_{\bar{b}}$ is expected to be dominated by the lowest order scattering diagrams [18, 19]. The behavior at lowest order is determined by the relative contribution from $q\bar{q}$ annihilation ($q\bar{q} \to b\bar{b}$), which leads to a dependence $\sim (\cosh \Delta y)^{-2}$ at large $\Delta y$, and gluon fusion ($gg \to b\bar{b}$), which produces a somewhat broader rapidity correlation, falling off only as $(\cosh \Delta y)^{-1}$ [18]. For either process, the cross section is suppressed for sufficiently large $\Delta y$. It is therefore expected that the $b\bar{b}$ pair will be found closely separated in rapidity.

This strong rapidity correlation plays a central role in the design of dedicated forward $b$ detectors for the study of $CP$ violation at hadron colliders [20, 21]. $CP$ violation refers to the non-invariance of the weak interaction Hamiltonian under the combined operations of charge conjugation ($C$) and parity ($P$). Although $CP$ violation is not specifically forbidden in the Standard Model, the exact mechanism involved in the breaking of this symmetry might point the way to physics beyond the Standard Model. The observation of significant mixing between the neutral pseudoscalar $b$ mesons ($B^0$, $\bar{B}^0$) opened the door to $CP$ violation measurements in the $B$ system [22].

Hadron colliders provide the potential for high precision measurements due to the large total $b\bar{b}$ cross section ($50\,\mu$b). The forward region is of particular interest since the production spectrum is expected to peak at small angles. In addition, for a given transverse momentum, $b$ quarks produced at large rapidity have a larger total momentum and correspondingly smaller multiple scattering error on the trajectories of the decay products, than those produced in the central region. The better resolution aids in separating the $b$ hadron decay vertex from the primary interaction vertex, which is critical for precision $CP$ violation measurements.

Forward $b$ detectors planned for the Tevatron and LHC seek to efficiently collect these high momentum $b\bar{b}$ pairs by exploiting the forward cross section enhancement and the strong rapidity correlation between the $b$ and $\bar{b}$. Both of these properties of $b\bar{b}$ hadroproduction are illustrated in Fig. 1.1, which shows the laboratory production angle of one $b$ hadron with respect to the second in $p\bar{p}$ collisions at $\sqrt{s} = 1.8\,\mathrm{TeV}$, as predicted by the ISAJET [23] Monte Carlo program. By instrumenting a relatively small physical solid angle these experiments are able to minimize cost while retaining good acceptance for detecting the heavy quark pair. Since the validity of this approach rests on theoretical calculations, it is important to check that the rapidity correlation predicted by QCD is correct.

In addition to its dependence on the matrix elements, the shape of the rapidity distribution also depends on the parton distribution functions (PDFs) inside the proton. In particular, production of high momentum $b$ hadrons in the forward direction is sensitive to the PDFs at large momentum fraction $x$. Since the gluon fusion process dominates the $b\bar{b}$ production cross section (Sec. 2.2.1), the shape of the $b$ quark rapidity distribution at large $y$ should be sensitive to the shape of the gluon distribution $G(x, Q^2)$ at large $x$. The observation of an excess of high transverse energy jets reported by the CDF Collaboration at Fermilab has led to much speculation, as well as increased interest in the high-$x$ gluon content of the proton [24]. Such an excess is what one would expect to see if there exists a new

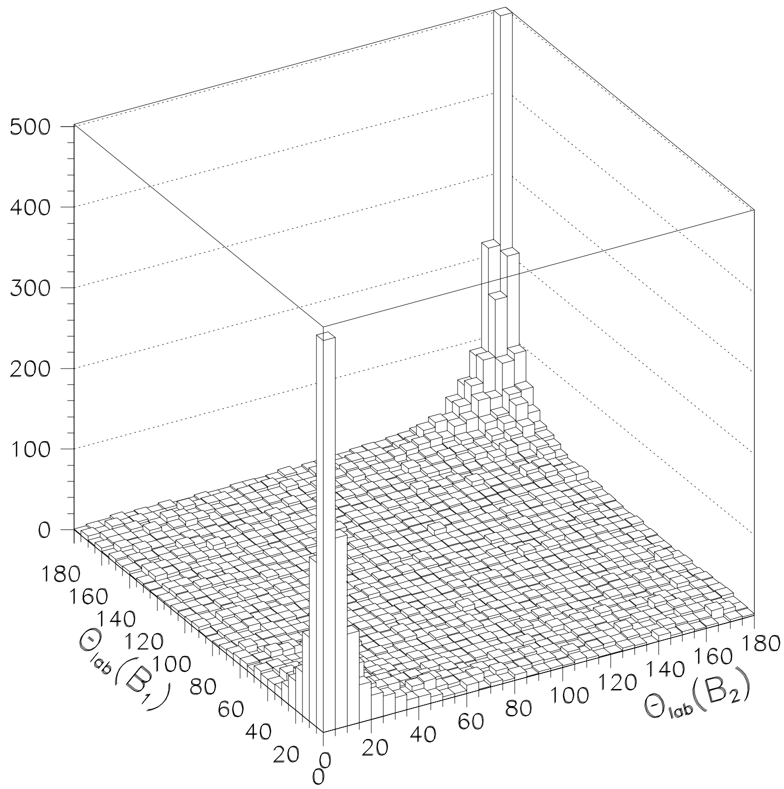


Figure 1.1: $B$ hadron production correlations in $p\bar{p}$ collisions at the Tevatron.

interaction associated with some large scale $\Lambda > 1$ TeV [25], and would imply that quarks are composite objects in the same way that the SLAC experiments showed that protons have structure. However, the excess could also be due to our limited knowledge of the gluon momentum distribution $G(x, Q^2)$ at high-$x$.

It has recently been demonstrated that $G(x, Q^2)$ in the region $x < 0.15$ is constrained to within 10% by Drell-Yan and deep inelastic scattering data, but is essentially unconstrained at higher values [26]. Historically, direct photon production, through the Compton scattering process $gq \rightarrow \gamma q$, has provided the only direct constraint on $G(x, Q^2)$ for $x > 0.15$. However, the full sensitivity of this process has yet to be realized due to uncertainty in the correct modeling of initial state transverse momentum ($k_T$) [27, 28]. An accurate measurement of forward $b$ production could therefore provide an important additional constraint on the gluon distribution at high-$x$.

### 1.1.2 Forward $b$ Production

Until recently, measurements of $b$ production at $p\bar{p}$ colliders have been restricted to the central region; $|y_b| < 1.5$ for the UA1 measurements at CERN [29, 30, 31], and $|y_b| < 1.0$ for the CDF [32, 33, 34, 35] and DØ [36] measurements at the Tevatron. The absence of precision track reconstruction capabilities in the forward region severely limits the techniques available for separating $b\bar{b}$ events from the large background of multijet events at a hadron collider. In addition, particles from the proton remnant and uncorrelated beam-gas collisions populate the region near the beam line, further complicating identification of the $b$ hadron decay products at large rapidity.

The DØ Collaboration was the first to report a forward $b$ production measurement at a hadron collider [37]. They identified muons in the rapidity range $2.4 < |y| < 3.2$ and determined the fraction of muons from $b$ decay by first subtracting the expected shape and normalization of the $p_T$ spectrum for muons from the decay of light mesons ($\pi, K$). The remaining events were attributed to bottom and charm production and the relative amount of each process was determined from Monte Carlo predictions.

The DØ result agrees in the shape of the $p_T$ spectrum, but with a normalization in excess of the central value predicted by next-to-leading order (NLO) QCD [19] by a factor of four, Fig. 1.2. This discrepancy is beyond current estimates of the theoretical uncertainty from perturbative effects, which amount to an overall factor of two. In contrast, the theoretical uncertainty is able to account for the smaller

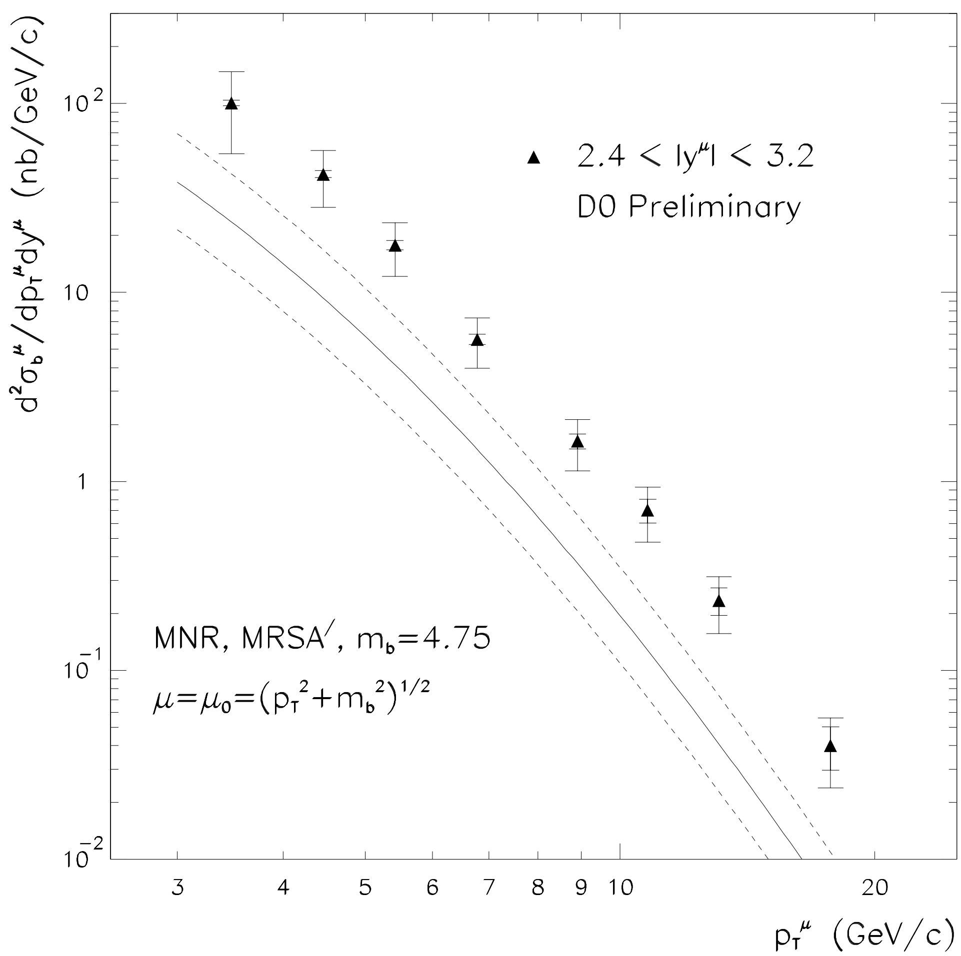


Figure 1.2: The differential cross section $d\sigma/dp_T$ for $b \to \mu$ decays in the rapidity range $2.4 < |y^\mu| < 3.2$ measured by the DØ Collaboration (points), compared with the QCD prediction (solid curve) and its uncertainty (dashed curves).

normalization excess observed in measurements of central production [38]. Recent studies by two separate groups show that an increase in the forward cross section can be obtained by modifying the heavy quark fragmentation function [39], or by employing the variable flavor number perturbative calculation [40] rather than the fixed flavor number scheme used in Ref. [19]. However, the increase in both cases is once again insufficient to account for the DØ result. Thus, an independent measurement in the forward region could help to resolve the discrepancy between data and theory observed by DØ.

## 1.2 Thesis Overview

In principle, cross section measurements are simple to perform. Given $N$ events detected with an efficiency $\epsilon$ from collisions involving particles with initial flux (luminosity) $\mathcal{L}$, the cross section $\sigma$ for the reaction is given by

$$\sigma = \frac{N}{\epsilon \cdot \mathcal{L}}. \tag{1.2}$$

However, the simplicity of Eq. 1.2 is deceptive. In the presence of background processes, $N$ must be corrected for the actual number of signal events in the sample. When measuring a quark-level cross section, the efficiency must account for the kinematic effect of the fragmentation and hadronization processes, which introduce a model-dependence into the experimental measurement. Finally, it is not always possible in practice to determine the initial luminosity with arbitrarily small error.

Although I also use the presence of a high-$p_T$ muon as the initial signature of $b$ decay, the analysis reported in this thesis takes a different approach to measuring the forward $b$ cross section than the DØ analysis. Rather than measuring the absolute forward cross section, I measure the relative rate of producing a $b$ quark in two separate rapidity intervals given that the second $b$ is produced in the central region. By simultaneously measuring the forward and central $b\bar{b}$ cross sections using similar data samples with identical kinematic requirements, I am able to eliminate or significantly reduce many of the experimental systematic uncertainties. Identification of the second $b$ in the central detector exploits the precision spatial resolution provided by silicon vertex detectors to suppress short lifetime (prompt) backgrounds, while facilitating a more direct test of the predicted $b\bar{b}$ rapidity correlation by positively identifying both heavy quarks.

The data used for this analysis correspond to $77\,\mathrm{pb}^{-1}$ of $1.8\,\mathrm{TeV}$ $p\bar{p}$ collisions collected by the Collider Detector at Fermilab (CDF) between January 1994 and July 1995 (Run 1B). The analysis method, illustrated in Fig. 1.3, exploits several convenient properties of $b$ decay to identify both the $b$ and the $\bar{b}$. I exploit the large semimuonic branching fraction by using the presence of a high $p_T$ forward or central muon as the initial signature of $b$ decay. The determination of the fraction of muons actually due to $b$ decay is facilitated by identifying the accomanying muon jet and fitting the muon transverse momentum relative to the jet axis, $p_T^{\mathrm{rel}}$. Due to the large mass of the $b$ quark relative to the four lighter quark flavors[6], muons from $b$ decay are more energetic and have a larger opening angle with respect to the recoiling jet than muons from charm and light quark decay. Finally, I exploit the long lifetime of the $b$ quark by identifying the second $b$ as a central jet associated with a secondary vertex displaced from the primary interaction vertex. An updated version of the $b$-tagging algorithm developed for the CDF top quark analyses is used to "tag" jets likely to contain a heavy quark. Real $b$-jets are separated from charm and non-heavy-flavor jets by fitting the transverse proper decay length $c\tau$ of the secondary vertex.

[6]The quark mass ratios are $m_t : m_b : m_c : m_s : m_d : m_u \approx 35000 : 1000 : 300 : 27 : 1 : 1$.

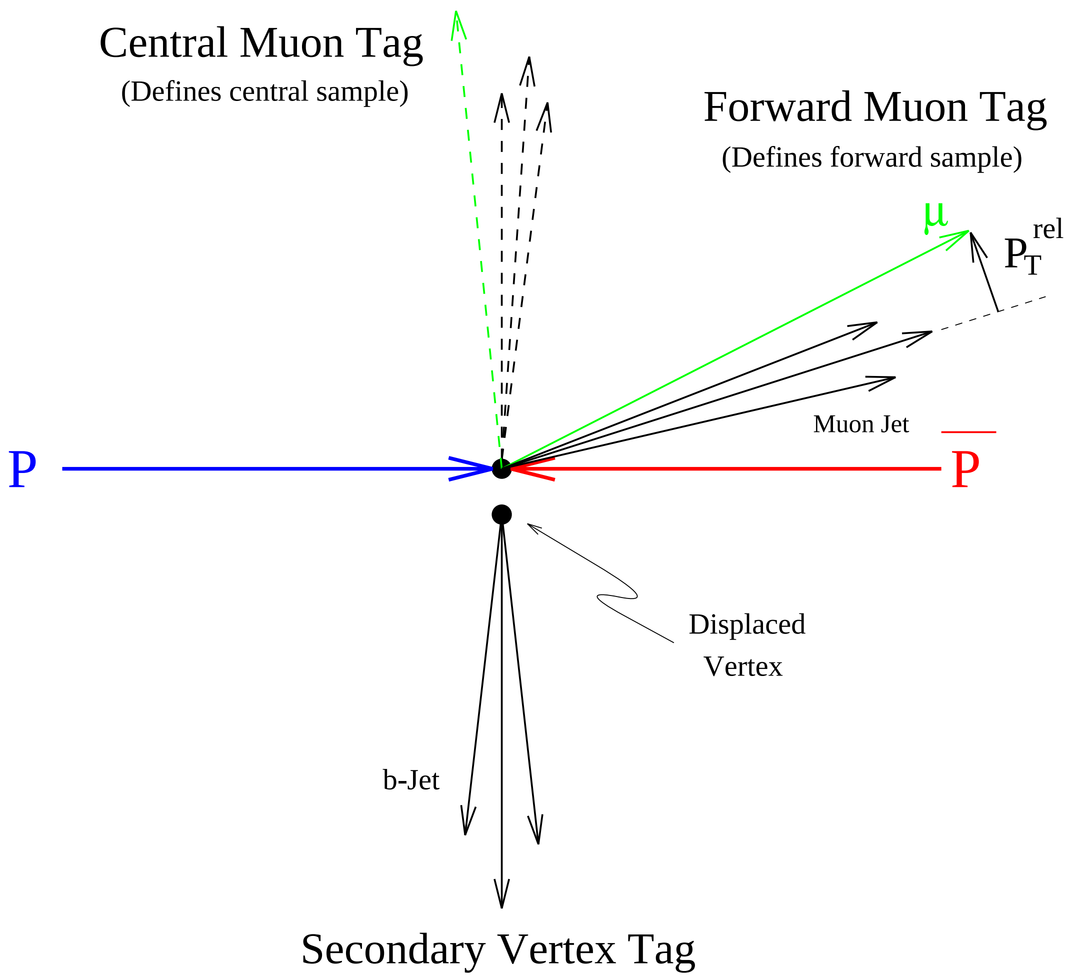


Figure 1.3: Illustration of the analysis method and topology of the event samples.

This thesis is organized as follows. The theory background necessary for an understanding of the experimental result is presented in Chapter 2, and the apparatus used to collect data is described in Chapter 3. In Chapter 4, I discuss the luminosity calculation for the datasets used in this analysis. In Chapter 5, I describe the selection criteria employed for the purpose of data reduction, and in Chapter 6 the total efficiency for detecting a $b\bar{b}$ pair passing these requirements is calculated. In Chapter 7, I describe the fitting procedure used to extract the signal fraction in the data, the cross section ratio result, and an analysis of the comparison between data and theory. Finally, in the closing chapter of this thesis I summarize the analysis results.

# Chapter 2

# Theory Background

In the introduction to the last chapter I briefly alluded to the complex structure of the proton, which, in addition to the three valence quarks ($uud$), consists of a sea of gluons and quark-antiquark pairs. Besides being a many-body problem, specification of the proton's internal state is complicated by the fact that the interactions between partons involve low (soft) momentum transfers and are therefore not calculable using perturbative QCD. Thus, for proton-antiproton collisions involving parton-parton interactions, the initial state is not well-defined. Similarly, the high $p_T$ partons produced in the collision must "dress" themselves into hadrons due to the confining nature of QCD. The hadronization process once again involves soft interactions that are not calculable from first principles.

From the above discussion, it would seem that the chance of learning anything about the short distance behavior of QCD from hadron collisions is slim. Fortunately, there exists a factorization theorem [41] for heavy quark hadroproduction which states that the soft interactions between partons in the initial state, and between the hadron constituents in the final state, can be separated from the hard scattering that produces the heavy quark pair. Thus, the cross section for production of hadrons $C$ and $D$ containing heavy quarks $c$ and $d$, from the hard scattering of partons $a$ and $b$ inside hadrons $A$ and $B$, is given schematically as

$$\sigma(AB \to CD) = \sum_{a,b} f_a^A(x_a) f_b^B(x_b) \otimes \hat{\sigma}(ab \to cd) \otimes F_c^C(z_c) F_d^D(z_d), \tag{2.1}$$

where the sum is over parton species and $\otimes$ denotes convolution. The functions $f$, referred to as parton distribution functions (PDF), parameterize the probability of finding a particular parton species inside the proton with momentum $xP_{\mathrm{proton}}$. The functions $F$, referred to as fragmentation functions, parameterize the probability of a quark fragmenting to a hadron with momentum $zP_{\mathrm{quark}}$. The parton-level cross section $\hat{\sigma}$ is calculated in perturbation theory as a series expansion in the strong coupling $\alpha_s$, and can be extracted from experiment given the set of functions $f$ and $F$. In this chapter I discuss each component of Eq. 2.1 in the context of bottom quark hadroproduction.

## 2.1 Perturbative QCD and Heavy Quark Production

I have already mentioned that quarks were introduced by Gell-Mann as the fundamental representations of the symmetry group SU(3) in order to explain the observed spectra of mesons and baryons. Quarks were postulated to be structureless particles satisfying Fermi-Dirac statistics that combined in sets of three to produce the baryon multiplets, or in quark-antiquark bound states to produce the meson multiplets. A statistics problem arose with the proposed quark structure of the $\Delta^{++}$ baryon, which from spin statistics should be a fermion, but supposedly consisted of three $u$ quarks in a totally symmetric bound state. The solution to this problem was to introduce an additional internal quark degree of freedom, referred to as color, which could take on one of three values (denoted red R, green G, and blue B). The three colors are fundamental representations of a color SU(3) symmetry group in analogy with the flavor symmetry of $u$, $d$, and $s$ quarks, with the exception that color SU(3) is believed to be an exact symmetry of the strong interaction. With the introduction of color, the $\Delta^{++}$ wavefunction could be made antisymmetric and the statistics problem was solved.

QCD is the gauge theory realization of the fundamental color interaction between quarks, and gluons are the massless spin-1 quanta of the color field. The application of perturbation theory (Feynman calculus) to the calculation of QCD scattering cross sections proceeds in analogy with quantum electrodynamics (QED). The Feynman rules for the calculation of scattering amplitudes are derived from the QCD Lagrangian, and the total amplitude $\mathcal{M}$ for a given process is the sum over all contributing Feynman diagrams. The differential cross section for a particle scattered into the phase space interval $d\mathcal{F}$ with initial flux $\mathcal{L}$ follows from Fermi's Golden Rule,

$$d\sigma = \frac{|\mathcal{M}|^2}{\mathcal{L}} d\mathcal{F}, \tag{2.2}$$

which is where theory meets experiment (cf. Eq. 1.2).

### 2.1.1 Renormalization and the Definition of "Heavy"

Ultraviolet divergences arise in the calculation of QCD amplitudes that are analogous to the infinities of QED, although with very different physical consequences due to the triplet nature of the color charge. The QCD singularities arise from the loop diagrams shown in Fig. 2.1, where a gluon propagating through the vacuum fluctuates into a quark-antiquark pair, or a pair of gluons. The later possibility is due to the nature of the color SU(3) group, which requires the gluons to be colored objects and therefore couple to other gluons. The loops in Fig. 2.1 result in the gluon propagator receiving an additional contribution in the form of an integral over the four-momentum circulating in the loop, $\int d^4p/p^2$. Since the internal lines making up the quark or gluon loops are not observable, the momentum can take on any value from 0 to $\infty$ and the integral becomes divergent.

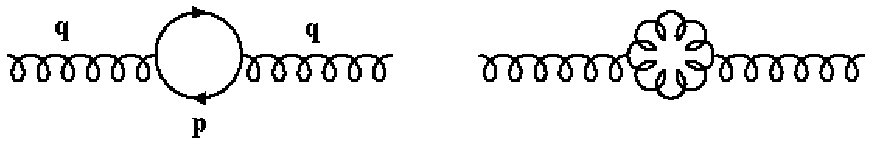


Figure 2.1: Examples of loop diagrams in QCD.

Because of the introduction of a second scale $p$ in the propagator, the coupling "constant" becomes a function of $q^2$, $\alpha_s = \alpha_s(p^2/q^2)$ [1]. The procedure for removing the divergence associated with $p \to \infty$ is referred to as renormalization, and involves a reparameterization of the color charge (coupling constant) in terms of its (finite) value at some reference scale $\mu$. The scale $\mu$ is an unphysical parameter, and therefore, the cross sections we measure cannot depend on it. This fact is expressed in a renormalization group equation (RGE),

$$\mu \frac{d\sigma(\alpha_s(\mu^2))}{d\mu} = 0, \tag{2.3}$$

the solution of which gives the dependence of $\alpha$ on $\mu$. At lowest order, corresponding to one loop, the result is

$$\alpha_s(\mu^2) = \frac{4\pi}{\beta \ln(\mu^2/\Lambda^2_{\rm QCD})}, \tag{2.4}$$

where $\beta = 11 - 2n_f/3$, with $n_f$ as the number of quark flavors, and the parameter $\Lambda_{\rm QCD}$ is the boundary condition for the differential equation (Eq. 2.3) and sets the scale for the running of $\alpha_s$ [43].

The scale $\mu$ is referred to as the renormalization scale ($\mu_R$) and there is no rigorous prescription for how to choose its value when comparing with a specific experimental measurement. The usual choice is to set it equal to the dominant

[1]This consequence can be understood in terms of a simple scaling argument, since if $\alpha$ is dimensionless, it can depend at most on the ratio of two dimensionful scales in the problem [42].

scale in the problem, generically referred to as $Q$. From Eq. 2.4 it follows that perturbation theory is applicable if $Q^2 >> \Lambda^2_{\mathrm{QCD}}$ so that $\alpha_s < 1$. The parameter $\Lambda_{\mathrm{QCD}}$ can be experimentally measured and the current estimate is $\sim 200\,\mathrm{MeV}$ [44]. This value is the natural scale of QCD and provides an operational definition for the term "heavy quark"; namely, quarks with $m >> \Lambda_{\mathrm{QCD}}$ are heavy, those with $m << \Lambda_{\mathrm{QCD}}$ are light. By definition then, heavy quark production is calculable in perturbative QCD (pQCD) since $\alpha_s << 1$. The top quark, weighing in at $175\,\mathrm{GeV}/c^2$, clearly qualifies for heavy quark status, as does the bottom quark ($m_b = 4.75\,\mathrm{GeV}/c^2$). There is continuing debate about whether the charm quark ($m_c = 1.5\,\mathrm{GeV}/c^2$) is sufficiently heavy to facilitate reliable perturbative predictions [38].

### 2.1.2 Heavy Quark Rapidity Correlations

At leading order, heavy quark (Q) pair production arises from quark-antiquark annihilation $q\bar{q} \to Q\bar{Q}$ and gluon fusion $gg \to Q\bar{Q}$, which I will collectively refer to as direct production[2]. The Feynman diagrams for these two processes are shown in Fig. 2.2, and the corresponding amplitudes have been known for some time [45]. Scattering cross sections are usually parameterized with the Mandelstam invariants:

$$\begin{aligned} \hat{s} &= (p_A + p_B)^2, \\ \hat{t} &= (p_A - p_C)^2, \qquad (2.5) \\ \hat{u} &= (p_A - p_D)^2, \end{aligned}$$

for a generic process $AB \to CD$. However, in the present context it will be more convenient to express the result in terms of variables that are actually measured in the lab. In terms of the rapidity variable $y$, defined as

[2]The leading order $Q\bar{Q}$ production processes are also referred to as "flavor creation".

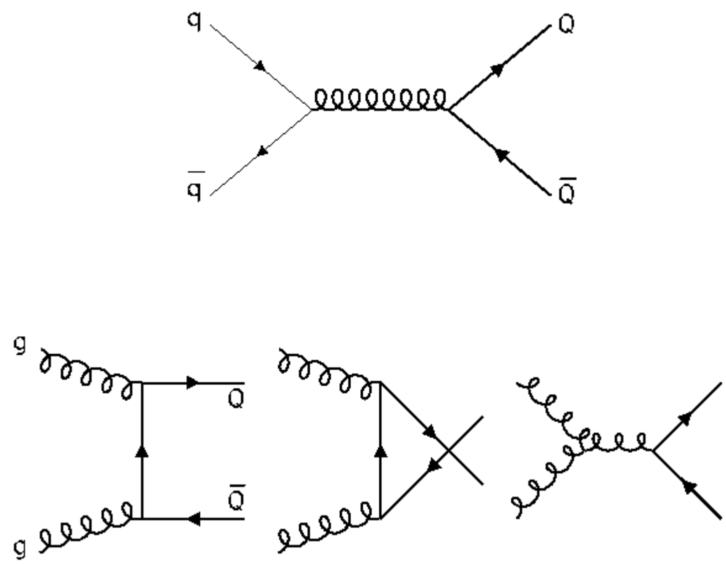


Figure 2.2: Lowest order Feynman diagrams for $q\bar{q} \rightarrow Q\bar{Q}$ and $gg \rightarrow Q\bar{Q}$.

$$y = \frac{1}{2} \ln \left( \frac{E + p_z}{E - p_z} \right), \tag{2.6}$$

and the transverse mass $M_T = \sqrt{m_Q^2 + p_T^2}$, the differential cross sections for $q\bar{q}$ annihilation and gluon fusion are [18]

$$\begin{aligned} \frac{1}{\pi}\frac{d\sigma}{d\hat{t}}(q\bar{q} \rightarrow Q\bar{Q}) &= \frac{1}{9}\frac{\alpha_s^2(\mu_R^2)}{M_T^4}\frac{\left[\cosh(\Delta y) + m_Q^2/M_T^2\right]}{\left[1+\cosh(\Delta y)\right]^3}, \qquad (2.7) \\ \frac{1}{\pi}\frac{d\sigma}{d\hat{t}}(gg \rightarrow Q\bar{Q}) &= \frac{1}{12}\frac{\alpha_s^2(\mu_R^2)}{M_T^4}\left[-\frac{1}{8} + \cosh(\Delta y)\right] \times \frac{\left[\cosh(\Delta y) + \frac{2m_Q^2}{M_T^2}\left(1 - \frac{m_Q^2}{M_T^2}\right)\right]}{\left[1+\cosh(\Delta y)\right]^3}, \end{aligned}$$

where $\Delta y \equiv y_b - y_{\bar{b}}$, and the renormalization scale is usually defined as $\mu_R = \sqrt{m_Q^2 + \langle p_T \rangle^2}$, with $\langle p_T \rangle = \frac{1}{2}(p_T^b + p_T^{\bar{b}})$. The cross sections depend on $\alpha_s^2$, since each vertex contributes a factor $\sqrt{\alpha_s}$ in the amplitude, and the cross section is proportional to the amplitude squared (cf. Eq. 2.2).

In Fig. 2.3 I compare the quantity $(M_T^4/\pi\alpha_s^2)d\sigma/d\hat{t}$ in the limit $p_T >> m_Q$ as a function of the rapidity difference $\Delta y$. The rapidity correlation differs significantly between the $q\bar{q}$ annihilation process, which has a dependence $\cosh(\Delta y)^{-2}$ at large $\Delta y$, and the gluon fusion process which falls off only as $\cosh(\Delta y)^{-1}$. This difference is directly related to the presence of the $\hat{t}$-channel exchange diagram in the gluon fusion process, which introduces terms like $1/\hat{t}$ and $1/\hat{u}$ into the cross section formula. These terms provide an enhancement in final states where the $Q$ and $\bar{Q}$ are produced at small angles with respect to the beam, leading to a large rapidity difference. In contrast, the annihilation diagram proceeds solely through the $\hat{s}$-channel, and therefore, produces a more isotropic final state. The heavy quark rapidity correlation is therefore directly sensitive to the difference between the two production mechanisms.

As illustrated in Fig. 2.4, entirely new production mechanisms enter into the cross section calculation if we consider all diagrams contributing to heavy quark production up to $\mathcal{O}(\alpha_s^3)$. In addition to the usual radiative corrections involving real gluon emission diagrams (a), heavy quarks can also be produced from the "decay" of a virtual gluon, the so-called "gluon splitting" process (b). Historically, if the heavy quark pair originates from the splitting of an initial state gluon the process is referred to as "flavor excitation" (c), since the corresponding leading order process for *inclusive* heavy quark production ($gQ \to gQ$) can be interpreted as "exciting" a heavy quark out of the parton sea of an incoming hadron [45]. The next-to-leading order (NLO) cross section cannot be expressed in closed form, but the exact result has been calculated numerically [19] and a FORTRAN program is available that allows the user to specify kinematic cuts on the heavy quark and antiquark, as well as the light parton (gluon or quark) [46]. In the context of rapidity correlations, the gluon emission and flavor excitation diagrams tend to broaden the $\Delta y$ distribution, while the gluon splitting process tends to produce a narrow peak at $\Delta y = 0$. Therefore, if one avoids regions of phase space where the

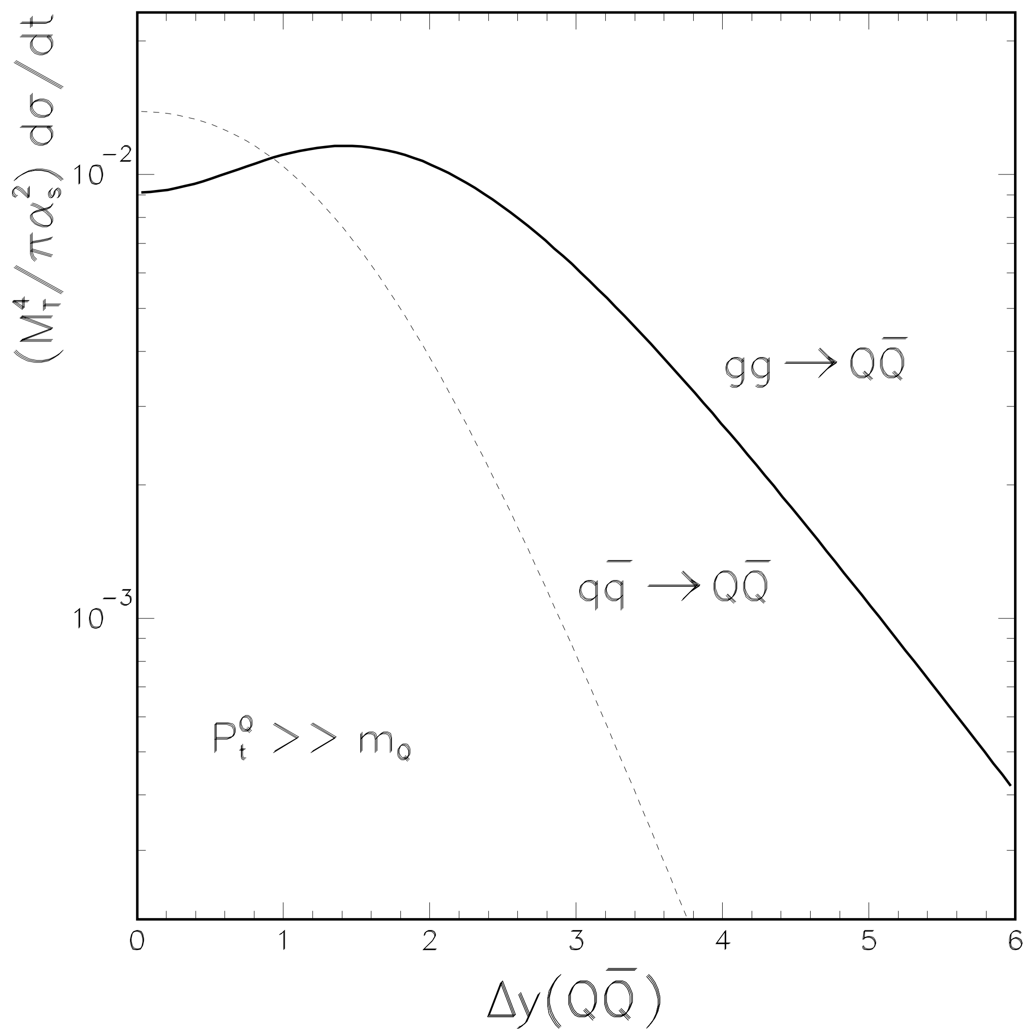


Figure 2.3: Comparison of the scaled differential cross section $d\sigma/d\hat{t}$ as a function of the heavy quark rapidity difference.

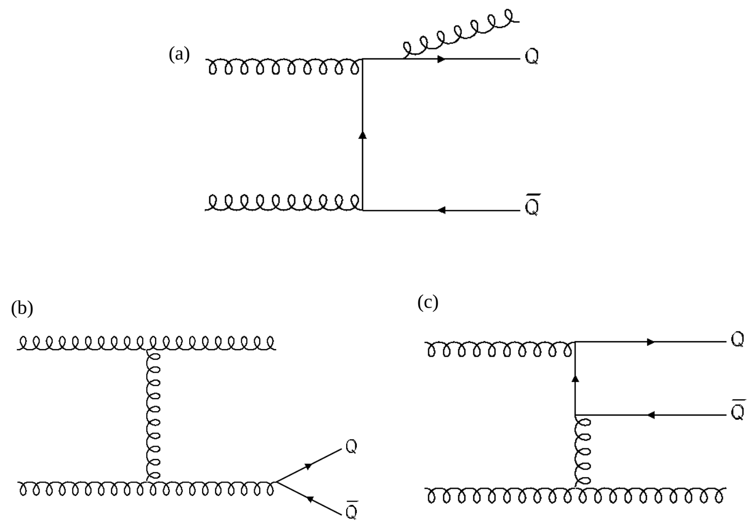


Figure 2.4: Some representative examples of next-to-leading order Feynman diagrams for $q\bar{q} \to Q\bar{Q}g$ and $gg \to Q\bar{Q}g$.

latter process is dominant, the rapidity correlation is expected to be very similar to the leading order result. Indeed, as we shall see in Chapter 7, this is the case.

## 2.2 Parton Distribution Functions

Before discussing the effect of the PDFs on the heavy quark rapidity distribution, I first review how the understanding of proton (or, in general, hadron) structure has evolved over the last 90 years, Fig. 2.5. After the scattering experiments of Rutherford, the proton was considered to be a structureless spin-1/2 particle. As we have seen, the experiments of McAllister and Hafstadter showed that the proton was an extended object described by electric ($G_E$) and magnetic ($G_M$) form factors, which specify the charge and magnetic moment distributions respectively. At higher energy, smaller wavelength, the SLAC deep-inelastic scattering experiments revealed behavior consistent with the electron scattering elastically from point particles

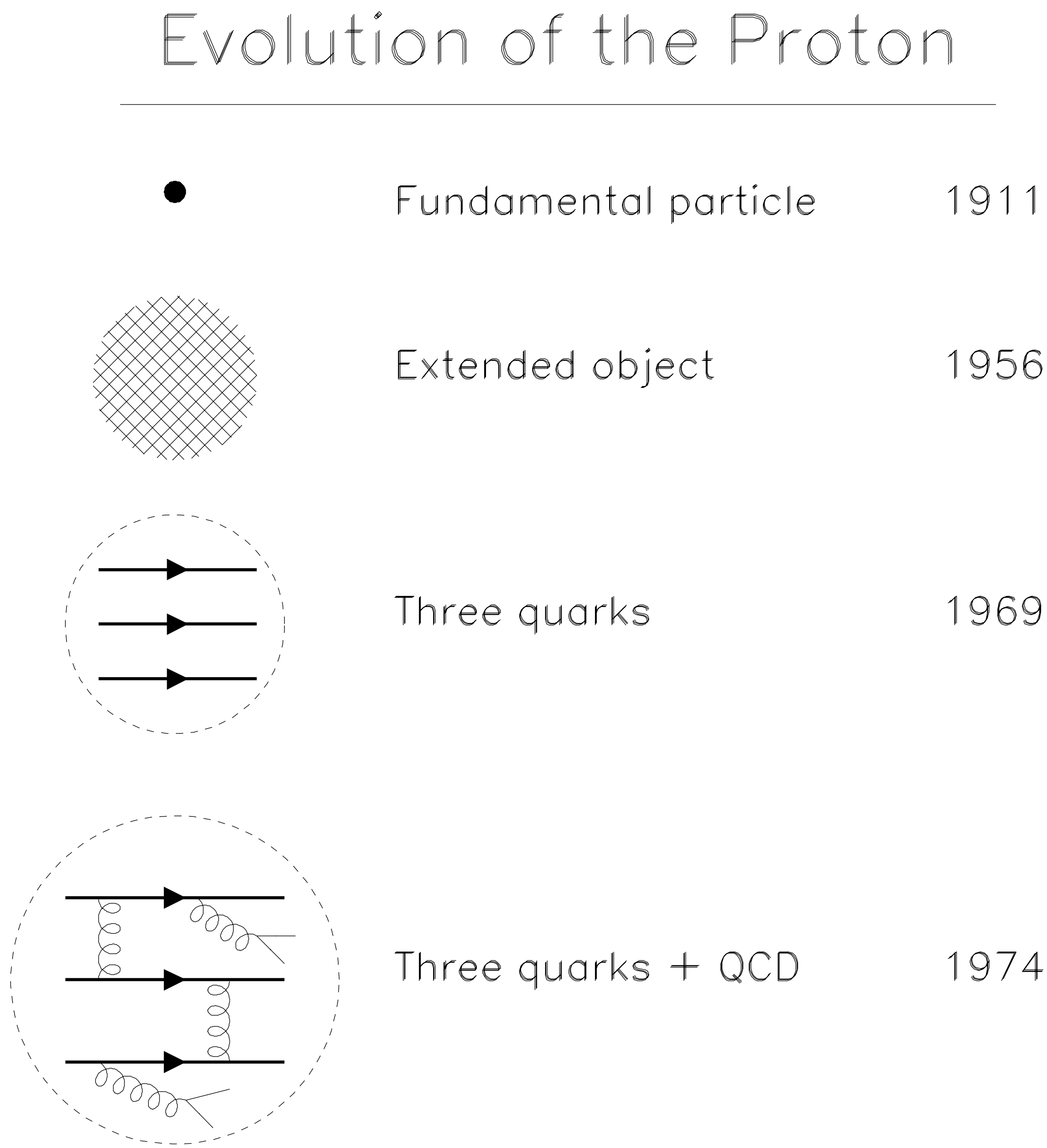


Figure 2.5: Illustration showing the evolution of the proton. (Adapted from Fig. 9.7 in *Quarks and Leptons*, F. Halzen and A. D. Martin, 1984.)

inside the proton. This observation led to what is now referred to as the naive parton model, which combines the infinite momentum frame formalism of Feynman, with the impulse approximation applied to lepton-hadron scattering by Bjorken and Pachos [47]. Briefly, the idea is that in a reference frame in which the proton has infinite momentum, the parton-parton interactions are "slowed down" due to relativistic time dilation. If the electron scatters in a time $\tau \sim P/Q^2$, where $P$ is the proton momentum in the center of mass and $Q$ is the four-momentum transfer, that is much less than the parton-parton interaction time $T \sim P/M_p^2$, then the partons can be considered free particles during the collision. The parton model is therefore only applicable if $Q^2 >> M_p^2 \approx 1\,\mathrm{GeV}^2$, which was satisfied by the SLAC experiments.

Although the parton model predicted the observed feature of scaling, it was already known in 1969 that the picture of the proton was incomplete, since approximately half of the proton's momentum appeared to be carried by neutral objects (*ie.*, not quarks). With the emergence of QCD as the most promising candidate theory of strong interactions, the structure of the proton changed once again [48]. If the quarks carry color then they can radiate gluons in a manner similar to the bremsstrahlung process in QED. Thus, a quark carrying a fraction $x$ of the proton's momentum can emit a gluon, becoming a quark with momentum $z < x$. This effect ruins the elastic nature of the electron-parton interaction, with the result that the cross section becomes a function of both $x$ and $Q^2$. In addition, gluons can split into $q\bar{q}$ pairs, which can themselves radiate other gluons, resulting in a parton sea of quarks and gluons. The physical interpretation of scaling violations[3] is that as $Q^2$ increases, the electron "sees" more partons from which to scatter. The parton distribution functions $f_a(x, Q^2)$ now describe the probability of finding a parton of type $a$ inside the proton with momentum fraction $x$, when probed with four-momentum $Q$.

[3] See Ref. [49] for further discussion.

In addition to introducing scaling violations, the emission of gluons depicted in Fig. 2.5 has a kinematic consequence that brings us back to the fractorization theorem, Eq. 2.1, and the separation of the soft parton-parton interactions within a hadron from the hard scattering which produces the heavy quark pair. The process $q \to qg$ gives rise to an integral over the emitted gluon's transverse momentum, $\int_0^{(p_T^2)_{\max}} dp_T^2/p_T^2$, that is logarithmically divergent as $p_T \to 0$. This "collinear" divergence is regularized by introducing a minimum cutoff $\mu$ in the integral, which then leads to a contribution $\alpha_s(Q^2)\log(Q^2/\mu^2)$ in the cross section that does not converge at large $Q^2$. The solution is to remove the $Q^2$ dependence from the perturbative calculation and absorb it into the proton via the parton distribution functions. A set of RGEs, the Altarelli-Parisi equations [50], govern the evolution of the PDFs in $Q^2$ just as Eq. 2.3 parameterizes the evolution of the strong coupling $\alpha_s(Q^2)$. We are left with a second arbitrary parameter, the factorization scale $\mu_F$, that sets the scale for evaluation of the evolution equations.

As a final comment[4], the complementary roles of $\mu_R$ and $\mu_F$ in taming the ultraviolet and collinear singularities are schematically illustrated in Fig. 2.6. As $Q^2$ is increased we are increasingly sensitive to effects that happen over a short time scale. Through the uncertainty principle, $\Delta E \sim \hbar/\Delta t$, the fluctuations depicted in Fig. 2.1 can "borrow" an increasing amount of energy from the vacuum, which leads, as we have seen, to the ultraviolet infinities that are absorbed into the redefinition of $\alpha_s$. The renormalization scale is simply the point at which we separate the short time scale physics from the perturbative calculation. At the other end of the spectrum, as $Q^2$ decreases the impulse approximation becomes less valid since there is an increased probability that a parton will radiate during the time the collision occurs. The factorization scale is the point at which we draw the proton boundary, all radiation ocurring outside is incorporated into the

[4]This discussion draws from lecture notes presented by D. E. Soper at the *CTEQ Summer School*, Lake Como, WI, 1997.

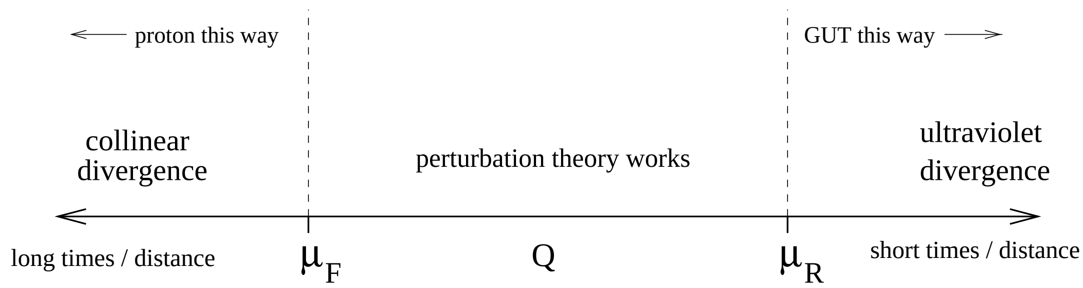


Figure 2.6: Schematic definition of the renormalization and factorization scales.

perturbative calculation, while what goes on inside is paramterized by the parton distribution functions. Since there is no prescription for determining exactly where we choose the cutoff points, in practice, the two scales are set equal for simplicity ($\mu_R = \mu_F \equiv \mu$).

The PDFs are usually extracted from lepton-hadron experiments, or from the Drell-Yan process in hadron-hadron collisions. In both cases, the QCD perturbative calculation is more accessible, and therefore more accurate, than for processes with all-hadronic final states. In addition, leptons do not hadronize, so the factorization formula contains only the partonic cross section convoluted with the PDFs, and an accurate calculation of the former facilitates extraction of the latter from experimental cross section measurements. Since any experiment covers a limited range of the $x$–$Q^2$ space, set by the center-of-mass energy, results from many different experiments are combined into "global QCD fits" that attempt to extract the distributions for all parton species in a given hadron simultaneously. There are currently two main groups who carry out such global analysis: MRS[5] and CTEQ[6]. I will be using the results from both collaborations.

[5]A. D. Martin, R. G. Roberts, and W. J. Stirling.

[6]CTEQ = "The Coordinated Theoretical-Experimental Project on QCD".

### 2.2.1 Rapidity Correlations Revisited

In order to understand the effect of the PDFs on the $b\bar{b}$ rapidity correlation, Fig. 2.3, I first note that for elastic ($2 \to 2$) scattering there exists an exact relation between the momenta of the colliding particles and the rapidities of the outgoing products,

$$x_{1,2} = \frac{M_T}{\sqrt{s}} \left[ e^{\pm y_b} + e^{\pm y_{\bar{b}}} \right], \tag{2.8}$$

where $M_T$ and $s$ were previously defined. Thus, for fixed $M_T$, or equivalently $Q$, and one particle produced central ($y \approx 0$), there is a one-to-one correspondence between the rapidity of the second particle and the momentum fraction of the initial state parton travelling in the same direction. Production of large mass objects requires large $x$ for both partons, and therefore, $y \approx 0$ for the center-of-mass of the produced particles, which is why experiments working at the energy frontier build central detectors. However, for particles with $m << \sqrt{s}$ there is sufficient phase space remaining to give a boost to the partonic center-of-mass system, which is the source of the forward/backward peak predicted in $b\bar{b}$ production at $\sqrt{s} = 1.8\,\mathrm{TeV}$ (Fig. 1.1).

Fig. 2.7 shows the parton densities $xf(x, Q^2)$ for up, down, and strange quarks, and gluons from the MRSA$'$ [51] global analysis, which I will use as the default parton distribution set. Here I have taken $Q^2 = 25\,\mathrm{GeV}^2$, which is the minimum $p_T$ for the $b$ quarks in my cross section definition (Table 1.1). The up and down quark curves are the sum of valence quarks, which contribute predominantly at $x \approx \frac{1}{3}$, and sea quarks, which increase as $x$ decreases due to the increased probability of a gluon splitting into a $q\bar{q}$ pair. In the plot, the gluon distribution is reduced by a factor of 10, and is therefore the dominant parton for $x < 0.2$. For central $b\bar{b}$ production with $p_T \sim 10\,\mathrm{GeV}/c$, the momentum fractions are $\sim 0.01$ and the gluon fusion process

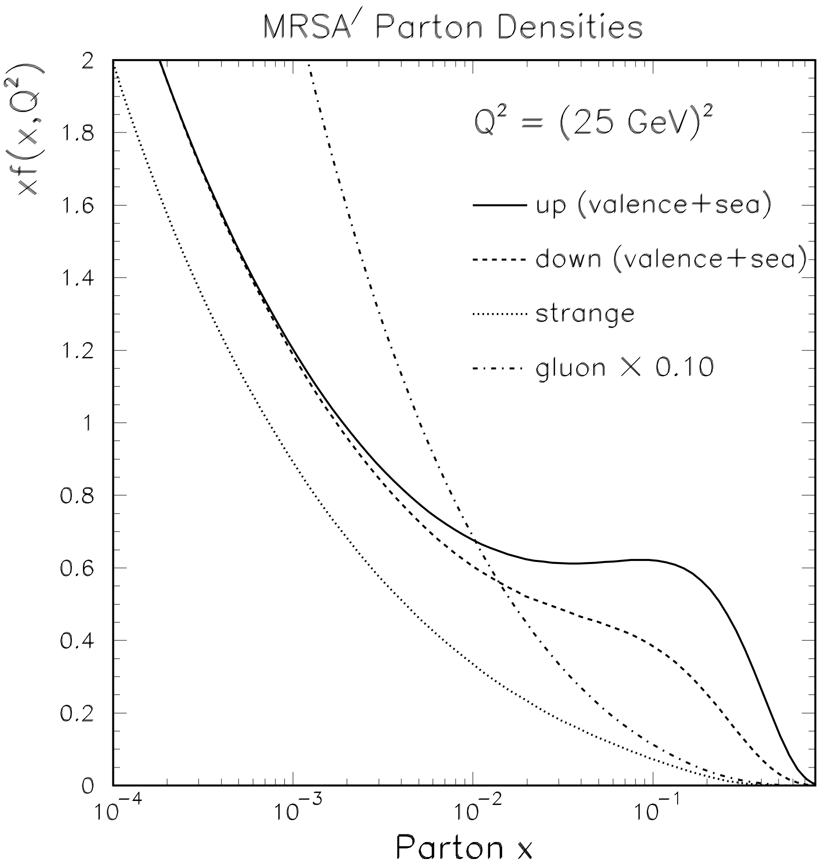


Figure 2.7: Parton distribution functions for the MRSA′ set.

dominates the cross section, despite the fact that the $q\bar{q}$ annihilation process has a larger amplitude for small $\Delta y$. Since the gluon distribution is falling rapidly as $x$ increases, we might expect the annihilation process to become significant at large rapidity. However, this is not the case, as can be seen in Fig. 2.8, which shows the Born level cross section calculation as a function of the rapidity of the $b$ quark, given that the $\bar{b}$ is central and $p_T > 25\,\mathrm{GeV}/c$ for both quarks. The gluon fusion process is 90% of the total, even at large rapidity. At higher orders there are more processes with gluons in the initial state than quarks, so the dominance of the gluon fusion process increases at $\mathcal{O}(\alpha_s^3)$.

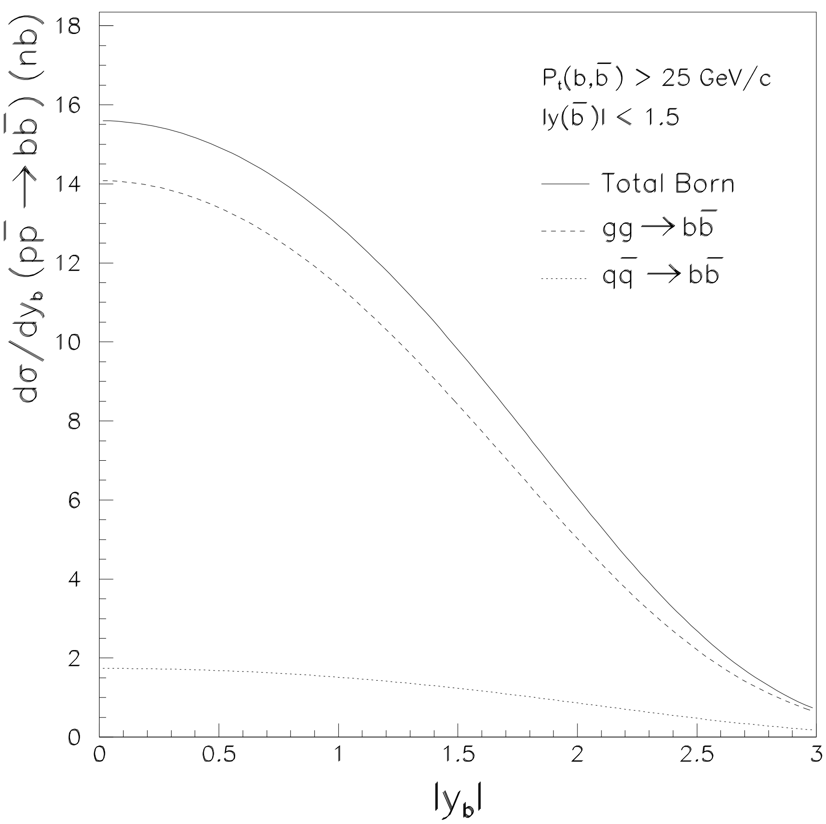


Figure 2.8: The born level differential cross section $d\sigma/dy_b$ for $b\bar{b}$ production corresponding to the cuts used in this analysis.

## 2.3 Heavy Quark Fragmentation

The $b$ quarks produced in the hard scattering can radiate some fraction of their momentum in the form of "hard" gluons and must eventually hadronize into the physical particle whose decay products are observed in the detector. The parton scattering cross section has been calculated to $\mathcal{O}(\alpha_s^3)$, so any diagrams involving more than three final state partons are formally contained in the fragmentation function. Since, by definition, the radiation of hard gluons can be calculated in perturbation theory, this process constitutes the perturbative part of the fragmentation function. In contrast, the actual hadronization process involves soft gluon exchange ($Q \sim 1/R_{\mathrm{hadron}} \sim 300\,\mathrm{MeV}$) and constitutes the non-perturbative part of the fragmentation function. In this analysis I am measuring *b quark* cross sections, so the acceptance calculation must account for the slowing down of the quark through radiation and hadronization, since the resulting decay products of the $b$ hadron will be less likely to satisfy the kinematic cuts. The procedure is to parameterize the radiation phase as a cascade process using Monte Carlo techniques. This can be done to leading order or next-to-leading order accuracy. The hadronization process is then parameterized as a function of $z$, the probability of a quark with momentum $p$ becoming a hadron with momentum $zp$. The necessity of choosing a particular fragmentation scheme, both perturbative and non-perturbative, introduces a model dependence into the cross section measurement, although the effect is reduced by measuring the ratio of forward to central $b\bar{b}$ production.

For light quarks, the acceptance correction procedure I have just described does not converge. That is, the cross section to produce, for example, an up quark with $p_T > 10\,\mathrm{GeV}/c$ is undefined because a light (read massless) quark can radiate very soft collinear gluons that give rise to "infrared" singularities in the perturbative calculation. In contrast, heavy quarks do not suffer infrared divergences since the mass provides a natural cutoff. Using simple kinematic arguments [52, 53] it is possible to construct a phenomenological model of the heavy quark hadronization process, the most popular being the Peterson parameterization [54]:

$$F(z) = \frac{N}{z\left[1 - (1/z) - \epsilon/(1-z)\right]^2}, \tag{2.9}$$

where $N$ is a normalization factor and

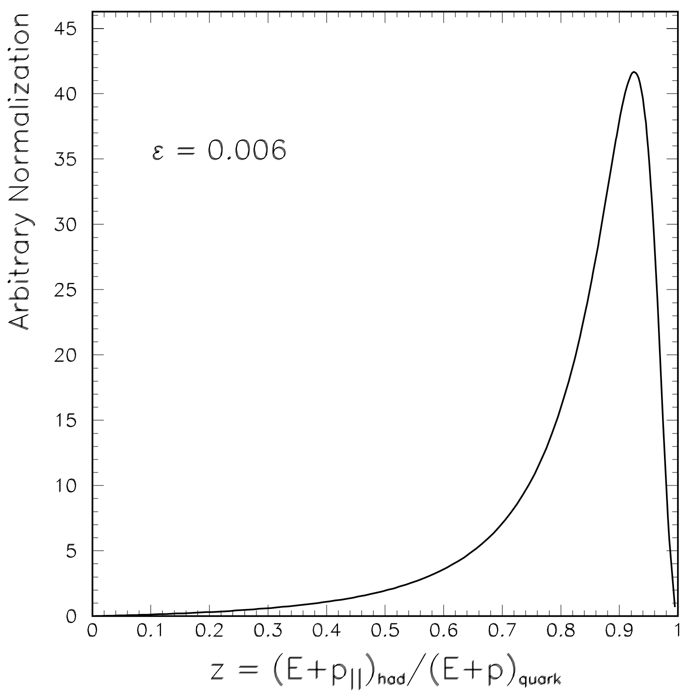


Figure 2.9: The Peterson fragmentation function for $\epsilon = 0.006$.

$$z = \frac{(E + p_{||})_{\mathrm{hadron}}}{(E + p)_{\mathrm{quark}}}, \tag{2.10}$$

with $p_{||}$ being the hadron momentum along the quark direction. The function has one parameter, $\epsilon$, which can be extracted from $B$ decays in $e^+e^-$ collisions. I use the traditional value $\epsilon = 0.006$[55, 56], for which I plot the Peterson form in Fig. 2.9. I return to the question of non-perturbative fragmentation functions in Sec. 7.2.1.

# Chapter 3

# Experimental Apparatus

The experiment described in this thesis was performed at the Fermi National Accelerator Laboratory (Fermilab), using the Collider Detector at Fermilab (CDF) to collect data from the highest energy proton-antiproton ($p\bar{p}$) collider in the world, the Tevatron. I begin this chapter by describing the various steps involved in accelerating and colliding protons and antiprotons at high energy, and the collider conditions which existed during the data taking period relevant to this thesis. I then give an overview of the CDF, followed by more detailed descriptions of the major detector subsystems. Finally, I close with a description of the data acquisition and trigger system, including the specific triggers used in this analysis.

## 3.1 Fermilab and the Tevatron

The Fermilab accelerator complex comprises five individual accelerators working in tandem to produce $p\bar{p}$ collisions at a center-of-mass energy of 1800 GeV, Figure 3.1. Each accelerator is designed to be efficient over a limited energy range; accepting protons (or antiprotons) from a lower energy accelerator and passing them on at a higher energy to the next accelerator in the chain. In this section I describe the separate steps involved in accelerating protons and anti-protons to 900 GeV, and the operating conditions of the Tevatron during the data taking period relevant for this thesis.

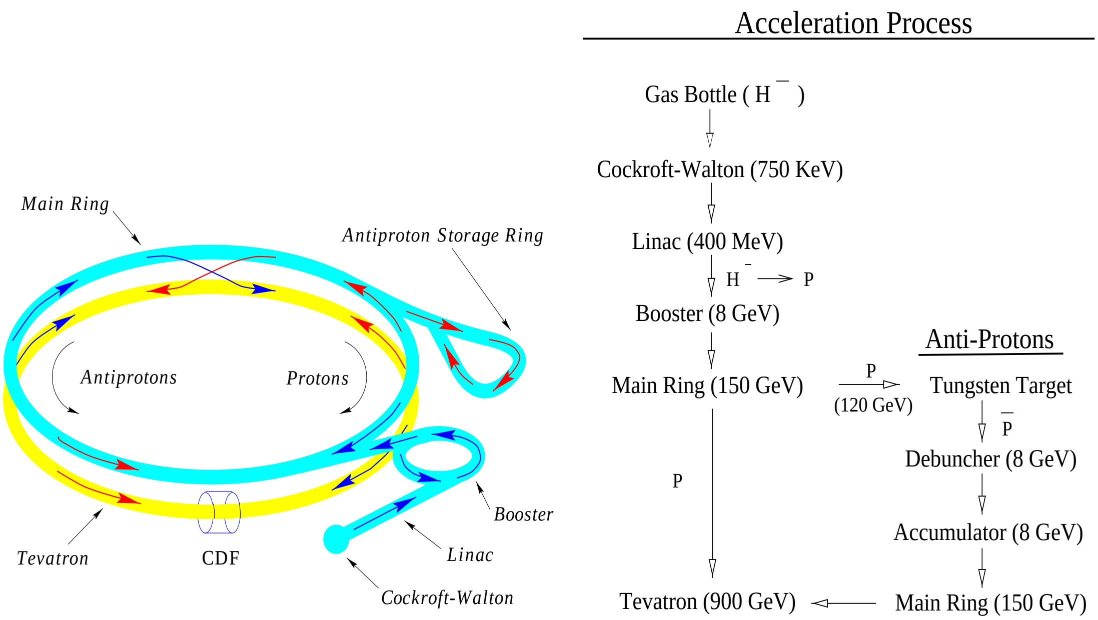


Figure 3.1: Schematic view of the Fermilab accelator complex, and a flow chart summarizing the acceleration process.

### 3.1.1 Proton Acceleration

The proton acceleration process begins with an ion source that produces 18 KeV $H^-$ ions from a bottle of ordinary hydrogen gas. The ions are injected into a Cockcroft-Walton electrostatic accelerator where they travel through a potential drop of 750 KV. The maximum voltage, and therefore energy, achievable with such an accelerator is limited by arcing and corona discharge. The Cockcroft-Walton produces a pulsed beam of 750 KeV $H^-$ ions every 67 milliseconds (15 Hz).

The 750 KeV ion beam is transported 10 m and injected into the next phase of the acceleration process, a two-stage linear accelerator (Linac) that ultimately increases the ion energy to 401.5 MeV. The first stage is an Alvarez linac [57] consisting of 5 radio frequency (RF) cavities resonating at 201.249 MHz. Within each cavity are a series of metal drift tubes alternating in polarity and separated by small gaps. While inside the drift tubes the ions are shielded from the RF field and travel at constant velocity. In the gap region the ions are accelerated toward the next drift tube, gaining a constant amount of energy proportional to the voltage of the RF field. To keep the ions in phase with the accelerating field as their energy increases, drift tube length increases along the beam line such that the travel time between successive gaps remains equal to the period of the RF field. When this length approaches half the RF wavelength, the drift tubes begin to act like antennas, radiating away the RF energy needed to accelerate the ions. For $H^-$ ions, this corresponds to a practical energy limit of 200 MeV. The Linac first stage reaches an energy of 116 MeV.

The Linac second stage is a side-coupled accelerator [58] consisting of seven RF cavities resonating at 804.996 MHz. Side-coupled linacs avoid the need to increase drift tube length by producing a travelling wave (rather than the static wave in an Alvarez design) that moves along with the ions so that the acceleration field is always in phase with the beam. The second stage raises the energy of the ion beam to 401.5 MeV. Just before entering the next acceleration phase, the Booster, the ions pass through a carbon foil that strips off the electrons, leaving only protons. The Linac has the same 67 ms cycle time as the Cockcroft-Walton.

Linear accelerators are inherently limited by the fact that the beam passes each accelerating cavity only once. To reach higher energies it becomes more practical to bend the beam around in a circle so that it passes many times through each RF cavity. Proton synchrotons are designed to do just that. The Booster is a 75.5 meter radius proton synchrotron with 17 RF cavities capable of accelerating protons to 8 GeV every 67 ms. Conventional dipole magnets are used to keep the protons in their circular path for the $\sim 20,000$ revolutions needed to reach the maximum energy. Using an RF frequency of 52.813 MHz, the Booster ring provides 84 regions of stable acceleration, referred to as "buckets". The batch of protons in each bucket are collectively referred to as a "bunch". Protons are injected into the next stage of acceleration, the Main Ring, 15 bunches at a time.

The Main Ring is a scaled-up version of the Booster, with a 1 km radius and 18 RF cavities resonating at 53 MHz. It requires 774 dipole magnets, and 240 quadrupole magnets, to steer the protons around their $2\pi$ km orbit while keeping the beam focused. For collider operation, the Main Ring accelerates the train of 15 proton bunches from 8 to 150 GeV before coalescing them into a single bunch occupying the central bucket of the train. The coalesced bunch is then injected into the final stage of acceleration, the Tevatron, to await the arrival of five more proton bunches, and six similar bunches of antiprotons. The Main Ring cycle time is 2.4 sec. Before describing the Tevatron, I will first describe the very different path travelled by the antiprotons on their way to joining the protons in the Tevatron.

### 3.1.2 Antiproton Production and Acceleration

The Fermilab antiproton ($\bar{p}$) source exploits the large $\bar{p}$ production cross section in proton-nucleus collisions for incident energy near the Main Ring's design energy [59]. Production of antiprotons thus begins with Main Ring protons accelerated using the process described above. A proton energy of 120 GeV, rather than the nominal 150 GeV Main Ring energy, was determined to be optimal for producing the highest flux of $\bar{p}$'s at the desired storage energy of 8 GeV. The resulting Main Ring cycle time at 120 GeV is 2 sec.

Before transferring the protons to the target station, the Main Ring RF cavities are manipulated to rotate each bunch 90° in phase space; exchanging, in accordance with Liouville's theorem, a large time spread and small momentum spread for a small time spread and large momentum spread. This exchange assists in maximizing the phase space density of the $\bar{p}$'s at production, which eventually facilitates the cooling of the $\bar{p}$ beam in the storage ring. Because of the resulting short bunch length, the number of protons per bunch is limited to $\sim 10^{12}$ in order to limit the heat flux generated in the target assembly.

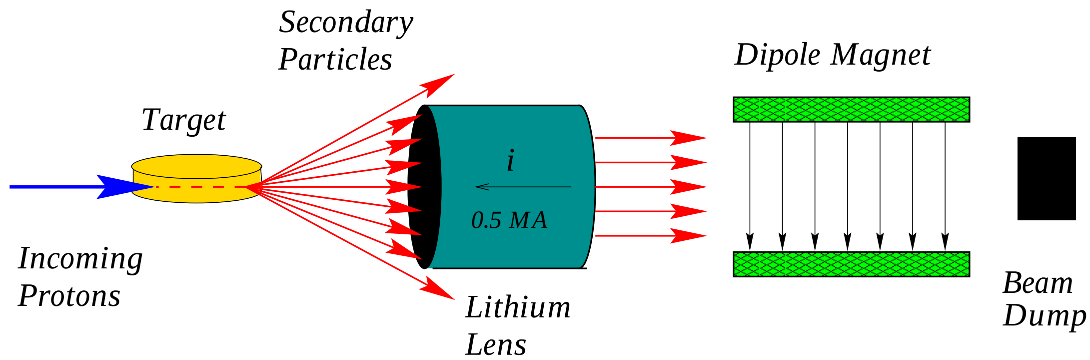


Figure 3.2: Diagram of the antiproton production and collection system.

Figure 3.2 shows a diagram of the target station. The 120 GeV protons from the Main Ring pass through a cylindrical target assembly consisting of alternating disks of Ni (target) and Cu (cooling), such that the beam subtends a chord through the disks. In addition to translating horizontally to tune the proton path length, and therefore the $\bar{p}$ flux, the target assembly rotates to more evenly distribute the heat and radiation damage produced by the beam. For every batch of $10^{12}$ protons, approximately $10^7$ $\bar{p}$'s are eventually collected. The antiprotons emerge from the target over a wide solid angle and with a large momentum spread. A 15 cm long cylindrical lithium lens with a 2 cm diameter is used to focus the $\bar{p}$'s into a parallel beam. The focusing is accomplished by an azimuthal magnetic field with a radial gradient of 750 T/m produced by passing a 0.5 MA current along the axis of the cylinder. The use of Li as the conducting material minimizes beam loss from multiple scattering. The resulting parallel beam of $\bar{p}$'s passes through a 1.5 T dipole magnet that selectively deflects negatively charged 8 GeV particles toward the Antiproton Storage Ring.

Since the walls of any storage container necessarily consist of protons, the storage of antiprotons is inherently a complex problem. The Antiproton Storage Ring solves this problem by keeping the $\bar{p}$'s inside the vacuum tube of a triangular 8 GeV ring with a mean radius of 90 meters. To increase the maximum possible $\bar{p}$

flux in the Storage Ring, the phase space density of the beam is increased using a stochastic cooling technique first proposed by van der Meer [60]. To be effective, this cooling technique requires the injected beam to have a small emittance (area in phase space) and momentum spread. As I already mentioned, the $\bar{p}$'s arriving from the target station do not satisfy these criteria. It was therefore necessary to have two rings; the purpose of the first ring, the Debuncher, is to reverse the phase space rotation performed by the Main Ring in order to reduce the momentum spread of the beam. In addition, the beam is "debunched" by adiabatically reducing the RF frequency, thus allowing particles to cross bucket boundaries. The phase rotation and debunching process takes only 10 ms, so the remainder of the 2 sec Main Ring cycle is spent reducing the transverse emittance of the beam by a factor of 3.

Just before another batch of $\bar{p}$'s is injected into the Debuncher, the current batch, now with reduced emittance and momentum spread, is injected into the second ring, the Accumulator. As its name implies, the purpose of the Accumulator is to store the produced $\bar{p}$'s until enough have been collected to be injected into the Tevatron, via the Main Ring, for high luminosity $p\bar{p}$ collisions. The accumulation process is referred to as "stacking", which consists of moving the injected $\bar{p}$'s in towards the stack core orbit ($\approx 60$ MeV less than the injection orbit), and further reducing the momentum spread and transverse emittance of the core by stochastic cooling.

The term "cooling" refers to the analogy between the betatron oscillations of the individual particles in the beam and the motion of particles in a classical ideal gas, for which the temperature $T$ is given by the well-known relation

$$\frac{3}{2}kT = \frac{1}{2}m\langle v^2\rangle. \tag{3.1}$$

Since the transverse emittance of the beam is related to the average transverse momentum of the $\bar{p}$'s, reducing the emittance can therefore be regarded as cooling the beam (see Ref. [61] for further discussion). The cooling is accomplished through a feedback mechanism that senses the rms deviation of the beam from the central orbit with electrostatic plates, and transmits this information to another set of plates downstream that correct the slope of the beam back towards the central orbit.

When a sufficient number of $\bar{p}$'s ($\sim 10^{11}$) has been accumulated, the 53 MHz RF is turned on to collect approximately half of the stack into 11 bunches for injection into the Main Ring. Once transferred to the Main Ring the 11 $\bar{p}$ bunches are accelerated to 150 GeV and then coalesced into one bunch in a manner similar to the protons. Although the number of $\bar{p}$'s in the final bunch is less than for a corresponding proton bunch, the coalescing efficiency decreases rapidly with more than 11 bunches. The lower resulting luminosity is therefore compensated by the shorter time needed to restore the $\bar{p}$ stack to its original size. The coalesced bunch is then injected into the Tevatron, followed by five more similar bunches.d

### 3.1.3 Tevatron and $p\bar{p}$ Collisions

The Tevatron was the first proton synchrotron to use superconducting dipole bending magnets in its lattice. The maximum energy of a proton synchrotron using conventional dipole bending magnets is ultimately limited by power loss due to resistive heating of the coils. The use of superconducting materials for the magnet coils solves this problem since resistive heating does not occur. The resulting savings in energy costs more than make up for the cost of cooling the magnets to liquid helium temperature (4 K). The Tevatron occupies the same tunnel as the Main Ring and shares many of the same parameters. It has the same 1 km radius, the same number of dipole magnets, a similar number of quadrupole focusing magnets (216), and the same 53 MHz RF structure as the Main Ring.

Once the six proton and six antiproton bunches are in the Tevatron, the energy is ramped from 150 to 900 GeV in only a few seconds. Since particle and antiparticle have opposite charge, the proton and antiproton bunches are accelerated in the same beam pipe in opposite directions. While being accelerated the two beams are kept spatially isolated by electrostatic separators. When the beams reach 900 GeV, special high-power quadrupole magnets (low-$\beta$ quads) installed in the CDF and the DØ experimental halls are energized to force the two beams to collide at the center (interaction point, or IP) of each detector. The final phase of the acceleration process involves "scraping" the beam to remove stray particles in the beam halo that could collide with residual gas in the beam pipe and produce background radiation in the experimental halls. When scraping was complete the Tevatron was producing stable $p\bar{p}$ collisions and the experiments could begin data acquisition. The entire process, from particle acceleration to the time when the beam was dumped (intentially or unintentially), was referred to as a store. Depending on the intitial luminosity, a store could last anywhere from a few hours, to over 12.

During Run 1B, a typical proton bunch contained 150 billion particles, while a typical antiproton bunch contained 50 billion particles. With an RF frequency of 53 MHz, the longitudinal extent of each of the 1113 buckets was approximately 5.6 meters. The focusing of the low-$\beta$ quads was such that each bunch was longitudinally distributed according to a gaussian of width 30 cm and a transverse rms size $\sim 25\,\mu$m (Figs. 8 and 9 from Ref. [62]). The bunches were equally spaced around the lattice, so the time between collisions in the CDF experimental hall was $3.5\,\mu$s.

The luminosity of a bunched-beam $p\bar{p}$ collider is often estimated with the following simplified equation,

$$\mathcal{L} = \frac{N_p N_{\bar{p}} N_B f}{4\pi\sigma_{xy}^2}, \tag{3.2}$$

where $N_{p,\bar{p}}$ are the number of particles in each bunch, $N_B$ is the number of bunches, $f$ is the orbital frequency, and $\sigma_{xy}$ is the rms size of the beam in the transverse plane (assumed to be bi-gaussian). With the numbers given above and an orbital frequency of 47.7 kHz, the estimated typical luminosity during Run 1B was $2.7 \times 10^{31}\,\mathrm{cm}^{-2}\mathrm{s}^{-1}$; which demonstrates the limitations of Eq. 3.2, since the highest luminosity recorded by CDF during Run 1B was only $2.4 \times 10^{31}\,\mathrm{cm}^{-2}\mathrm{s}^{-1}$. The exact formula for the luminosity takes into account the different intensities of each bunch, as well as the dependence on their longitudinal and transverse profiles [63, 64]. Since the lattice parameters that determine the shape of each bunch must be measured outside the interaction region of the two detectors, the accuracy of an absolute luminosity calculation is ultimately limited by uncertainty in the extrapolation of the beam conditions to the region where particles actually collide. In practice, CDF monitored the luminosity in real time by measuring the rate of inelastic $p\bar{p}$ collisions. A detailed description of this measurement will be given in Chapter 4. During Run 1B, the typical luminosity at the beginning of a data run was between 1 and $2 \times 10^{31}\,\mathrm{cm}^{-2}\mathrm{s}^{-1}$.

## 3.2 Detector

The CDF is a general purpose modular detector designed to analyze the debris produced in high energy $p\bar{p}$ collisions. In the context of this thesis, the purpose of the detector is to efficiently identify the decay products of $b$ hadrons and provide techniques to separate signal from background. In this section I first give an overview of the general features of the detector, and then describe the individual components relevant to this thesis. Since detailed descriptions of the CDF exist in the literature [65, and references therein], the discussion will be phenomenolgical rather than technical.

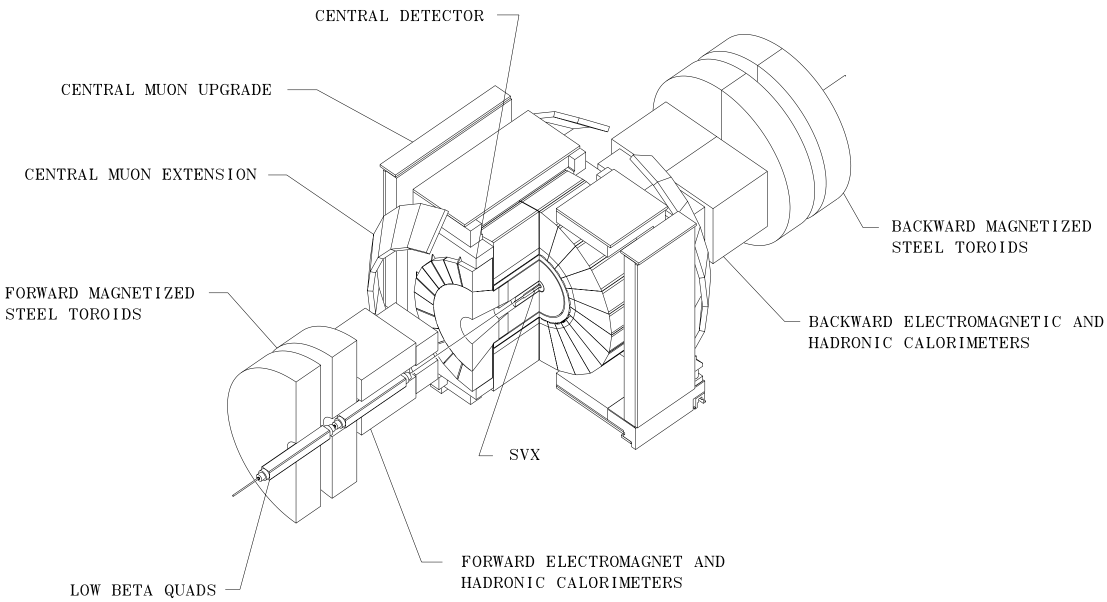


Figure 3.3: Isometric view showing three quarters of the CDF in Run IB.

CDF consists of a central detector comprising tracking, calorimeter, and muon subsystems, and two forward/backward detectors comprising calorimeters and muon spectrometers. An isometric view of the detector is shown in Fig 3.3. The Tevatron beam pipe passes through the center of the detector, while the low-$\beta$ quads can be seen embedded in the forward sepectrometer at the lower left corner of the diagram. Charged particle trajectories are reconstructed in three dimensions using the CDF central tracking system, consisting of three complementary detectors immersed in a 1.4 T solenoidal magnetic field. The field is generated by a 1.5 m radius solenoid consisting of 1164 turns of Nb-Ti/Cu superconducter, and facilitates determination of a charged particle's transverse momentum from its measured curvature. Located just outside the solenoid, the central calorimeter system consists of electromagnetic (EM) and hadronic (HAD) calorimeters designed to measure the total energy of charged and neutral particles. As mentioned, the forward detectors also house calorimeters. In this thesis, the non-muonic $b$ decay products are detected as localized energy deposition in the calorimeters. Finally, muon detectors are located beyond the calorimeters in both the central and forward detectors. Because the muon mass is approximately 200 times the electron mass, muons radiate much less than electrons. In addition, muons do not feel the strong force, and therefore, do not interact strongly with nuclei as hadrons do. These properties are exploited by placing the muon detectors outside the many interaction lengths presented by the calorimeters, which stop most hadrons but allow the muons to penetrate.

Fig. 3.4 shows a more detailed view of one quadrant of the detector and the orientation of the CDF coordinate system. A right-handed cylindrical coordinate system is motivated by the symmetry of the detector, which in turn is derived from the rapidity and azimuthal scaling of secondary particle production in high energy hadron collisions[1]. The origin of the coordinate system is located at the geometric center of the detector. The $\hat{z}$ direction is defined along the proton beam direction (East), $\hat{x}$ points radially out (North) from the center of the Tevatron, and $\hat{y}$ is vertical. Azimuth ($\phi$) and polar ($\theta$) angles are measured from the $x$ and $z$ axes respectively, while the cylindrical radius variable $r$ measures perpendicular distance from the beam line. Transverse quantities ($p_T$, $E_T$, etc) refer to projections in the $r-\phi$ plane. Finally, pseudorapidity, $\eta \equiv -\ln(\tan(\theta/2))$, is often more convenient than rapidity to express angle with respect to the beam. I distinguish between detector pseudorapidity $\eta$, calculated using the primary vertex $z$ position, and detector pseudorapidity $\eta_D$, which uses $z = 0$. In the limit $m/p_T \to 0$, rapidity and pseudorapidity coincide. In the remainder of this section I describe in more detail the tracking, calorimeter, and muon systems of the CDF.

[1] See Chapter 4 of Ref. [66] for a discussion of particle production in hadron collisions.

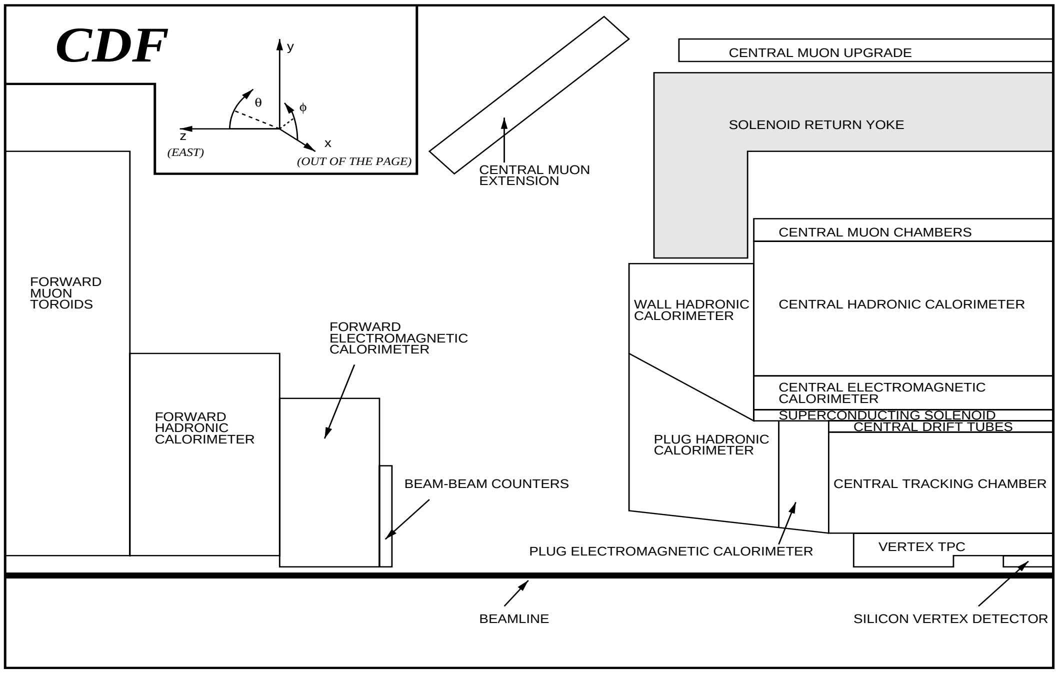


Figure 3.4: A schematic side-view of one quadrant of the CDF.

### 3.2.1 Tracking System and Track Reconstruction

Precision track reconstruction is critical to the success of any $B$ physics measurement, but conflicting requirements are placed on the tracking system. Identification of displaced vertices from $b$ decay requires excellent spatial resolution and detection capability as close as possible to the interaction region. Good momentum resolution requires a large volume detector capable of accurately measuring the radius of curvature of high-$p_T$ charged particles in the magnetic field. Finally, determination of jet directions from energy clusters in the calorimeter requires accurate knowledge of the primary vertex $z$ position from tracking information in the plane containing the beam line. To satisfy these conflicting requirements, CDF employs three complementary detectors, each optimized to perform one of the tasks described above.

**Silicon Vertex Detector**

Closest to the beamline, a silicon vertex detector (SVX) [67] provides precision spatial resolution in the $r-\phi$ plane. The device installed for Run 1B [68] consists of four concentric layers of silicon microstrip detectors grouped into two modules (barrels) extending 25.5 cm in each direction along the beam line. A 2.15 cm gap separates the two barrels at $z=0$. The detector layers are located at radii of 2.86, 4.26, 5.69, and 7.87 cm, resulting in a measured impact parameter resolution of $(13+40/p_T)\,\mu$m for isolated tracks, where $p_T$ is the transverse momentum in GeV/$c$. The constant term in the resolution function arises from the inherent spatial resolution of the detector, while the $p_T$-dependent term is the familiar contribution from multiple scattering. Due to the 51 cm active length of the detector and the 30 cm length of the Tevatron bunches, the SVX samples $\approx 60\%$ of the $p\bar{p}$ collisions.

The basic detector element in the SVX is called a ladder and there are twelve ladders per layer, each subtending approximately 30° in azimuth. A ladder is comprised of three silicon wafers bonded end-to-end, with each wafer containing rows of microstrips aligned along the $z$ direction. The fundamental physics process involved in silicon detectors is the same as that in the common transistor: the p-n junction. A reverse-biased p-n junction contains a depletion region absent of free charge carriers, producing an electric field with a geometry similar to that of a parallel plate capacitor. When a particle traverses the depletion region, collisions with the semiconductor lattice excite valence electrons into the conduction band, creating electron-hole pairs that are swept towards the electrodes by the electric field. The motion of the electrons and holes in the field regions induces a current in the external circuit that can be integrated to give a pulse proportional to the charge liberated by the ionizing particle. Each microstrip is one such silicon detector, with widths of $60\,\mu$m in the inner three layers, and $55\,\mu$m in the outer layer. Although the location of each "hit" within a strip is not known, the position of a particle in the transverse plane can be determined with an accuracy better than $55\,\mu$m. This is accomplished by calculating the charge-weighted centroid of several adjacent hit strips, referred to as a cluster. The cluster centroids are then used to fit SVX tracks.

Fig. 3.5 displays SVX information from Event 6238 in data Run 56669, which was recorded on February 24, 1994. This event is one of the 382 that survive all of the cuts applied to the forward cross section sample (Chapter 5), and I will refer to it throughout the remainder of this section. The display shows an $r$–$\phi$ slice through the detector, indicating ladder position, location of the beam pipe (circle near the center), cluster hits (spikes protruding from ladders), reconstructed SVX tracks (radial line segments), and azimuthal position of energy clusters in the central calorimeter. The jet at $45°$ contains two SVX tracks that form a secondary vertex "tag" that is displaced from the primary. A blow-up of the beam-pipe region is displayed in Fig. 3.6, where the origin of the CDF coordinate system is indicated by the small cross. Many low momentum[2] tracks emanate from the primary vertex, while two high-$p_T$ SVX tracks are seen to form a secondary vertex displaced from the primary. The distance between the primary and secondary vertices in this event is $\approx 0.30\,$cm.

### Vertex Time Projection Chamber

Just outside the SVX, a set of 28 vertex time projection chambers (VTX) measure charged particle trajectories in the $r$–$z$ plane out to a radius of 22 cm, and over the pseudorapidity range $|\eta_D| < 3.25$. Tracking in the $r$–$z$ plane requires a unique geometry. Each VTX module is segmented into octants and consists of two drift regions, filled with a 50/50 mixture of argon-ethane gas, separated by a cathode

[2] Momentum is indicated by the length of each track.

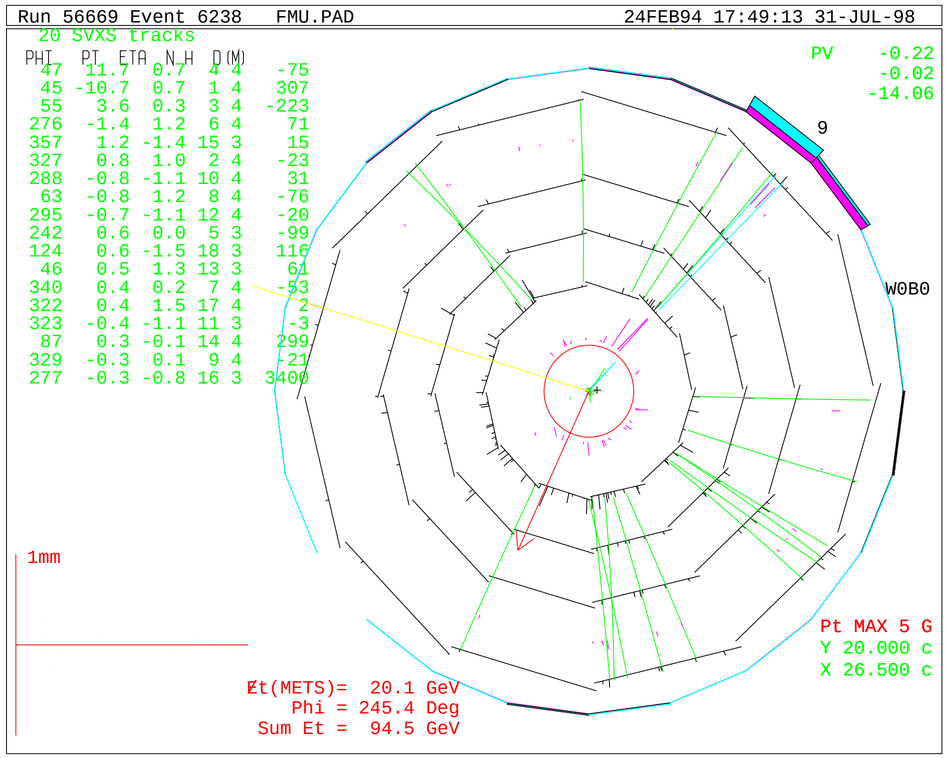


Figure 3.5: Event display showing reconstructed tracks in the SVX.

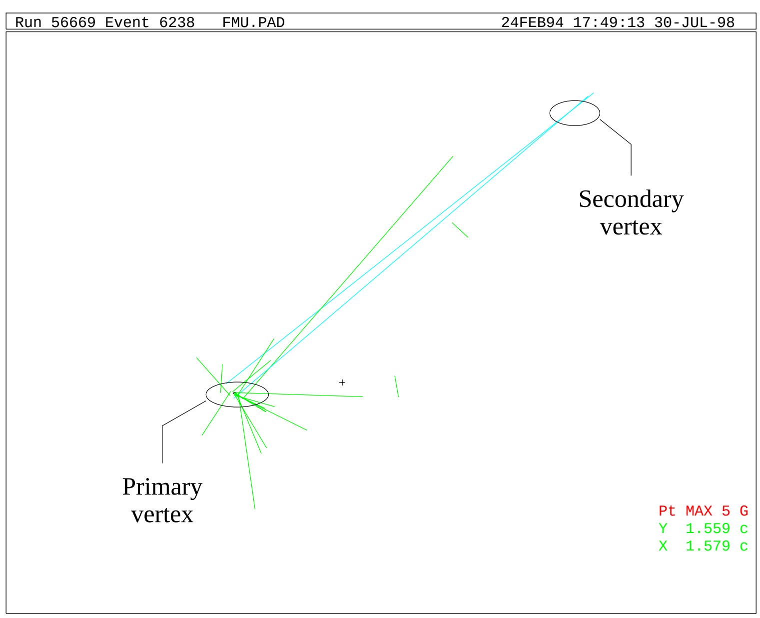


Figure 3.6: Blow-up of the beam-pipe region of Fig. 3.5.

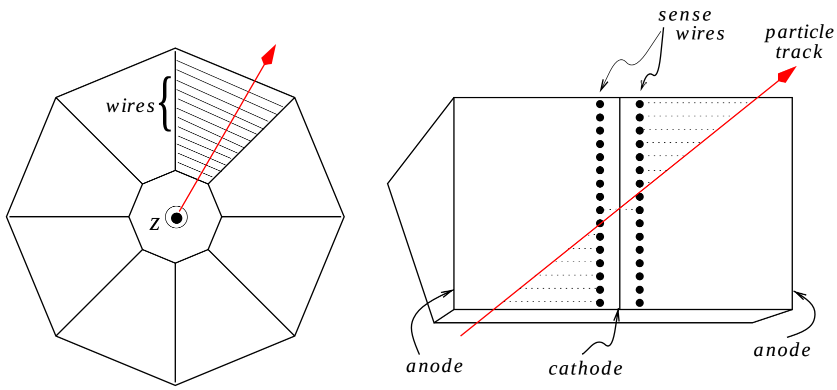


Figure 3.7: Schematic view of the VTX.

plane, Fig. 3.7. At the anode end, sense wires strung along chords in azimuth measure radius from the beam line. Gas molecules are ionized by the passage of charged particles through the detector, and the liberated charges drift at constant velocity until initiating an avalanche at the sense wires. The different drift times on adjacent wires are used to reconstruct the particle trajectory in the $r$–$z$ plane, as illustrated in Fig. 3.7. The VTX is capable of identifying the event vertex position in $z$ with a resolution of $\sim 1\,\mathrm{mm}$, which also facilitates separation of multiple $p\bar{p}$ interactions in the same crossing.

Fig. 3.8 displays the VTX information for the same event depicted in Fig. 3.5. The diagram shows a longitudinal slice, with the upper and lower detectors representing two opposing octants for the $\phi$ slice containing the $b$-tagged jet. The relative positions of the two SVX barrels are indicated by the rectangular boxes at the center of the diagram. Drift hits are seen to project back to several vertices (crosses) of varying quality[3]. The larger cross indicates the location of the primary vertex. The collection of tracks in the upper octant at $\eta \approx 1$ belong to the tagged jet. As we shall see, the collection of tracks in the lower octant at $\eta \approx 2$ belong to the jet containing the forward muon (Sec. 3.2.3).

[3]Parameters used to determine vertex quality include number of tracks and hit usage per track.

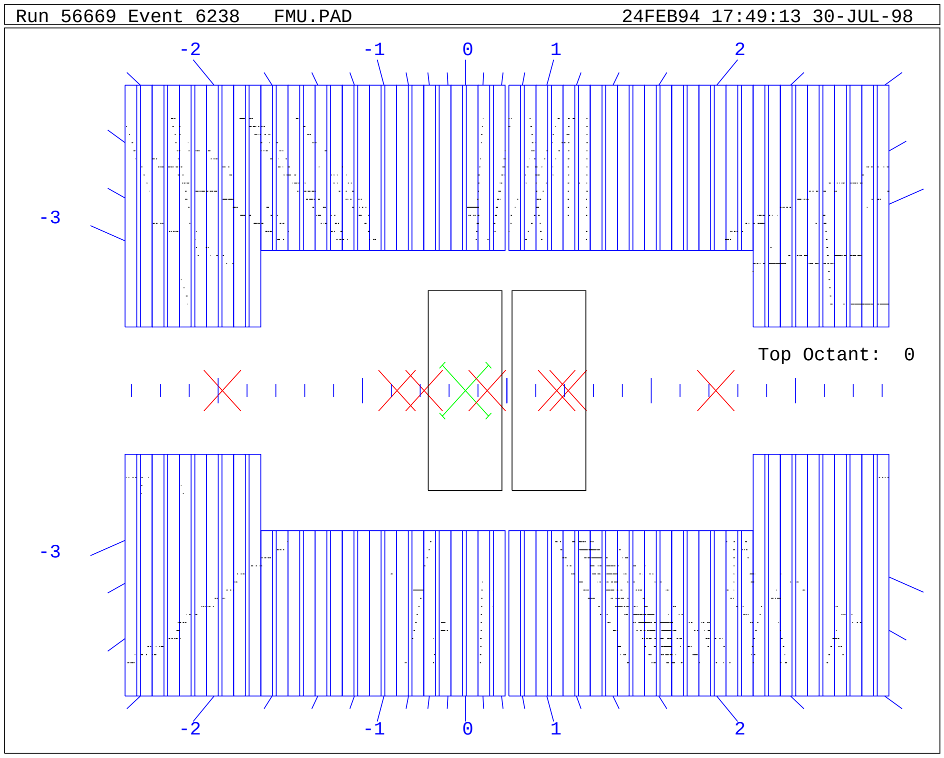


Figure 3.8: Event display showing the VTX.

### Central Tracking Chamber

The outermost tracking detector, the Central Tracking Chamber (CTC) [69], provides full three-dimensional track reconstruction out to a radius of 132 cm, enabling high resolution momentum measurements over the pseudorapidity range $|\eta_D| < 1.1$. The CTC is a 3.2 m long cylindrical open cell drift chamber consisting of 84 layers of 40 $\mu$m gold-plated tungsten sense wires grouped into nine superlayers filled with 50/50 argon-ethane gas. Fig. 3.9 shows a diagram of one CTC endplate indicating the geometry of the sense wire layout. The wires are grouped into five axial superlayers aligned along $z$, alternating with four stereo superlayers canted $\pm 3°$ with respect to the beam axis. Axial and stereo superlayers consist of 12 and 6 sense wire layers and provide tracking information in the $r$–$\phi$ and $r$–$z$ views respectively. The cylindrical shell of each superlayer is divided azimuthally into "cells" bordered

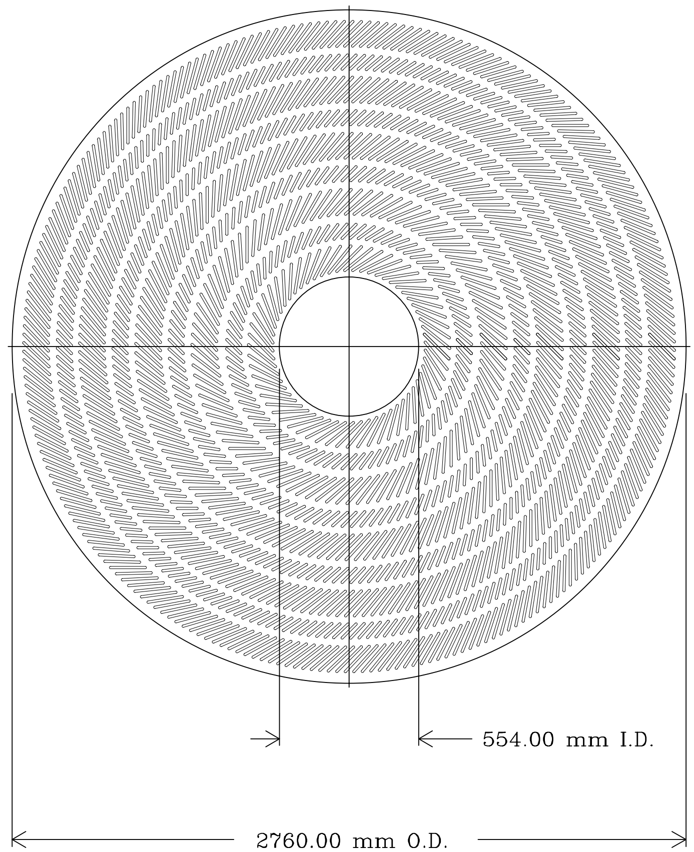


Figure 3.9: Diagram of the CTC endplate illustrating the wire-plane geometry.

by high voltage field shaping wires. Due to the presence of crossed electric and magnetic fields in the drift region, liberated charges will drift at an angle (Lorentz angle) with respect to the electric field, leading to a non-linear time-to-distance relationship at the edges of a cell. To compensate for the Lorentz angle, the cells are rotated approximately 45° with respect to the radial direction, which results in the characteristic spiral silhouette of the CTC wire slots shown in Fig. 3.9. The single hit spatial resolution of the CTC is $200\,\mu m$. A brief overview of CDF track reconstruction follows.

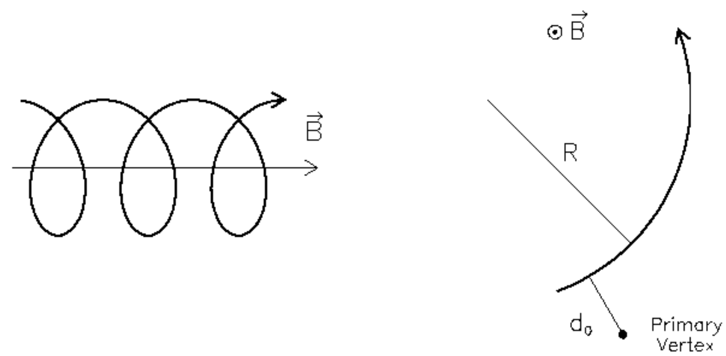


Figure 3.10: Motion of a charged particle in a uniform magnetic field.

**Track Reconstruction**

The motion of a charged particle in a uniform magnetic field is described by a circular helix with its axis aligned along the field direction, Fig. 3.10. In CDF, $\vec{B} = B\hat{z}$, so charged particles trace out circles in the $r$–$\phi$ plane while translating along $z$ with constant velocity. The helix is defined by five parameters: $z_0$, $\phi_0$, $\theta_0$, and impact parameter $d_0$ at closest approach to the primary vertex, and the radius of curvature $R$ in the transverse plane. The definition of impact parameter is illustrated in Fig. 3.10. It is defined as the perpendicular distance between the track and primary vertex at the point of closest approach in the transverse plane. For positive charged tracks, the CDF sign convention defines $d_0$ positive when the primary vertex is outside the circle, negative when it is inside. The convention is reversed for negative tracks. For a particle with charge $ze$ in a magnetic field $B$, the transverse momentum is given by

$$p_T = 0.3zRB, \tag{3.3}$$

where $B$ is in tesla, $R$ is in meters, and $p_T$ is in GeV$/c$. Thus, a measurement of $R$ determines the transverse momentum of the particle.

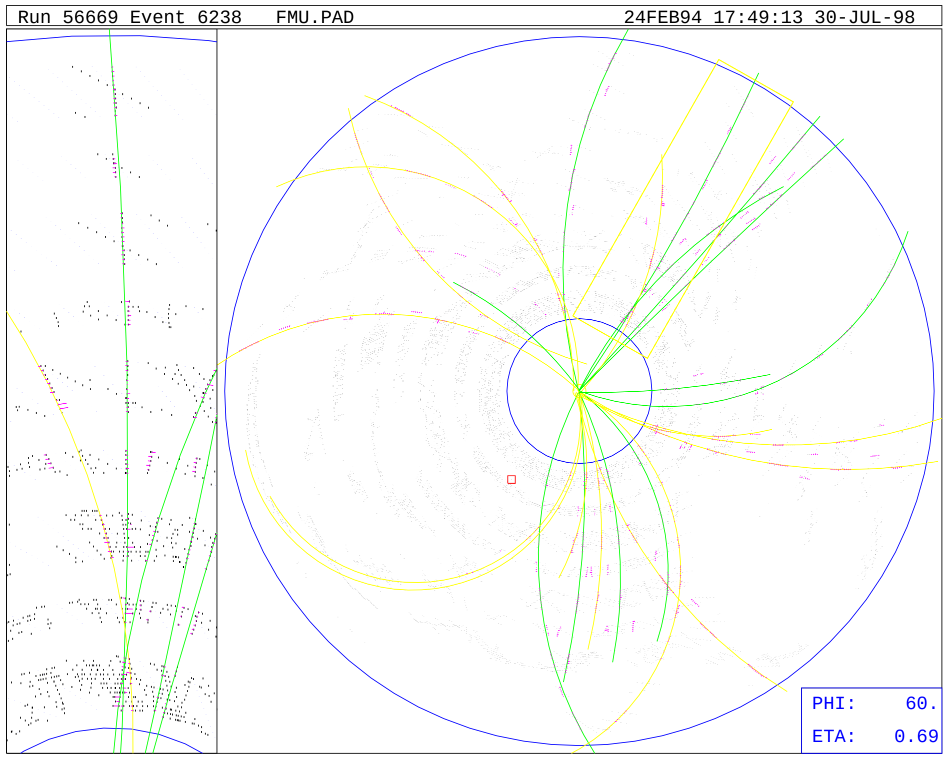


Figure 3.11: Event display showing reconstructed tracks in the CTC. The window to the left is a blow-up view of the region bordered by the rectangle.

CDF track reconstruction begins in the CTC[4]. Fig. 3.11 shows the CTC information for our sample event, where the curvature of low momentum tracks can be seen. Individual wire hits are indicated by dots, making the inner superlayers clearly visible due to the high occupancy of low momentum secondaries created in the $p\bar{p}$ collision. The two high momentum tagged tracks appear as relatively straight lines at 45°. The smaller window to the left shows an enlarged view of the region bordered by the rectangle in the main window. For each sense wire hit, both possible positions on either side of the wire are indicated. Because of the tilted cell design, this ambiguity is always resolvable since the "other" track possiblity does not point back to the interaction point.

[4]The VTX is capable of stand-alone tracking in the $r$–$z$ plane.

The track resconstruction algorithm begins by creating segments using hits within each axial superlayer cell. These segments are then combined to create a track candidate. Once an $r$–$\phi$ track candidate is found, stereo segments are added to give the $z$ information. SVX pattern recognition uses reconstructed CTC tracks extrapolated into the four layers of the SVX [70]. Matched clusters are assigned to the track, the combined CTC-SVX hits are refit, and the result is designated an SVX track. VTX track segments can be combined with CTC or SVX tracks in a similar manner. The momentum resolution of the CDF tracking system is $0.002p_T \oplus 0.0066$ for CTC tracks, where $p_T$ is in GeV/$c$. The resolution improves to $0.0009p_T \oplus 0.0066$ for tracks reconstructed in both the CTC and SVX.

### 3.2.2 Calorimeter System and Jet Identification

Calorimeters are multiparticle detection devices designed to measure total energy flow (magnitude and direction) by fully containing charged and neutral particles entering the detector. In this thesis, the CDF calorimeter system is used to measure the energy and position of jets resulting from the production and decay of $b$ hadrons. As there is no three-dimensional tracking in the forward region of the detector, calorimetry is the only method available for determining the jet axis when calculating $p_T^{\rm rel}$ for forward muons. Rather than simply providing information for kinematic cuts, the calorimeters play a central role in determining the signal fraction in the cross section samples. The calorimeter system is therefore an essential part of the physics analysis.

There are two main types of calorimeters, depending on whether the goal is to measure the energy of an electromagnetic shower initiated by an electron or photon, or a hadronic shower initiated by a meson or baryon. Electromagnetic showers are based on the principle that when a high energy ($> 10^2$ MeV) electron enters a medium it will lose energy predominantly by radiation, a process referred to as bremsstrahlung. Similarly, photons with $E > 10\,\mathrm{MeV}$ will preferentially lose energy by producing electron-positron pairs, which subsequently radiate to produce more photons. The scale for longitudinal development of such a shower is set by the electromagnetic radiation length $X_0$, which is proportional to the atomic mass $A$ and inversely proportional to the square of the nuclear charge $Z$ of the absorbing medium. EM calorimeters are therefore constructed from high-$Z$ materials, usually lead, to contain the shower in as small a volume as possible. In contrast, hadronic showers develop when an incident hadron undergoes an inelastic nuclear collision with production of secondary hadrons, which then collide with other nuclei producing tertiary hadrons, and so on. Ultimately, the bulk of dissipated energy appears as ionization loss from secondary protons and electromagnetic cascades initiated by neutral pions [71]. Unlike electromagnetic showers, a significant fraction of the initial energy of an incident particle is lost in a hadron shower due to nuclear breakup and excitation. The longitudinal scale of a hadronic shower is set by the nuclear absorption length $\lambda$, which is proportional to $A$ and inversely proportional to the nuclear absorption cross section $\sigma_{\mathrm{abs}}$ for the given medium. HAD calorimeters are larger than EM calorimeters since $\lambda > X_0$ for the same material.

CDF employs sampling calorimeters, so-named because they measure energy flow by alternating absorbing material with an active medium that samples the number of particles at a given depth in the shower. For both EM and HAD showers, the number of particles at any given depth in the shower is proportional to the incident particle energy $E_0$. Because fluctuations in the number of particles are governed by poisson statistics, the energy resolution for a sampling calorimeter is proportional to $1/\sqrt{E_0}$; with HAD calorimeters having worse resolution than EM calorimeters due to the lossed energy from nuclear breakup and excitation. As mentioned above, the absorbing material for EM calorimeters is usually lead, while HAD calorimeters use iron. Many options exist for the sampling component

**Summary of Calorimeter Properties**

| Detector | $\eta_D$-coverage | Energy resolution | Thickness |
|---|---|---|---|
| Central EM | $\|\eta_D\| < 1.1$ | $13.7\%/\sqrt{E_T} \oplus 2\%$ | $18\,X_0$ |
| Central HAD | $\|\eta_D\| < 0.9$ | $50\%/\sqrt{E_T} \oplus 3\%$ | $4.5\lambda_0$ |
| Endwall HAD | $0.7 < \|\eta_D\| < 1.3$ | $75\%/\sqrt{E} \oplus 4\%$ | $4.5\lambda_0$ |
| Plug EM | $1.1 < \|\eta_D\| < 2.4$ | $22\%/\sqrt{E} \oplus 2\%$ | $18 - 21\,X_0$ |
| Plug HAD | $1.3 < \|\eta_D\| < 2.4$ | $106\%/\sqrt{E} \oplus 6\%$ | $5.7\lambda_0$ |
| Forward EM | $2.2 < \|\eta_D\| < 4.2$ | $26\%/\sqrt{E} \oplus 2\%$ | $25\,X_0$ |
| Forward HAD | $2.4 < \|\eta_D\| < 4.2$ | $137\%/\sqrt{E} \oplus 3\%$ | $7.7\lambda_0$ |

Table 3.1: Summary of the CDF calorimeter properties. Thickness is give in radiation lengths ($X_0$) for EM calorimeters, and absorption lengths ($\lambda_0$) for HAD calorimeters.

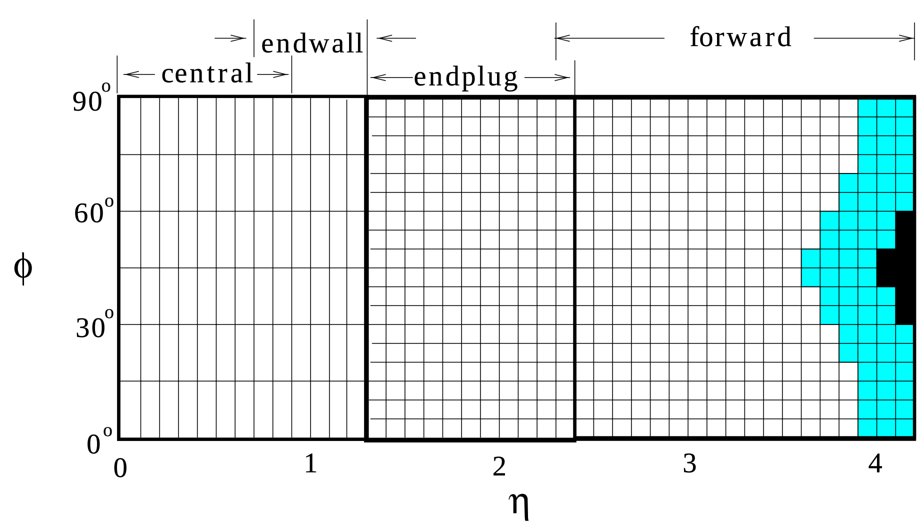


Figure 3.12: The CDF hadron calorimeter tower segmentation map.

of a sampling calorimeter; scintillator, gas, and liquid argon are some of the most popular choices in high energy physics. Whatever the active medium, its task is to produce an electronic signal proportional to the number of particles, and therefore energy loss, at a given longitudinal depth in the calorimeter. The sum of signals from each layer is then proportional to the total energy of the particle, or particles, entering the detector. Much hard work goes into calibrating a calorimeter to determine the constant of proportionality for a given detector geometry and material.

Referring to Fig. 3.4, the CDF calorimeter system [72, 73, 74, 75, 76] is divided into central ($|\eta_D| < 1.1$), plug ($1.1 < |\eta_D| < 2.4$), and forward ($2.4 < |\eta_D| < 4.2$) regions instrumented with electromagnetic (lead absorber) and hadronic (iron absorber) sampling calorimeters. Table 3.1 summarizes the main properties of each calorimeter. The central calorimeters use scintillator as the active medium and have energy resolutions that range from $13.7\%/\sqrt{E_T} \oplus 2\%$ for the central electromagnetic, to $75\%/\sqrt{E} \oplus 4\%$ for the endwall hadronic. The plug and forward calorimeters use gas (50/50 argon-ethane) as the active medium and have energy resolutions that range from $22\%/\sqrt{E} \oplus 2\%$ for the plug electromagnetic, to $137\%/\sqrt{E} \oplus 3\%$ for the forward hadronic. All of the calorimeters are segmented in $\eta$ and $\phi$ to provide a tower geometry that projects back to the nominal interaction point, Fig. 3.12. Each tower comprises both EM and HAD compartments and, unless specifically noted otherwise, tower energy refers to the sum of the two. The central calorimeters have a tower size of $\Delta\eta_D \times \Delta\phi = 0.1 \times 15°$, while the plug and forward calorimeters have a tower size of $\Delta\eta_D \times \Delta\phi = 0.1 \times 5°$. Projective tower segmentation assists in triggering and simplifies identification of jets with the use of a cone clustering algorithm (discussed below).

Fig. 3.13 displays the calorimeter information for our sample event, arranged in the form of a lego plot based on the $\eta$–$\phi$ segmentation shown in Fig. 3.12. For each hit tower, the total (transverse) energy deposited is proportional to the

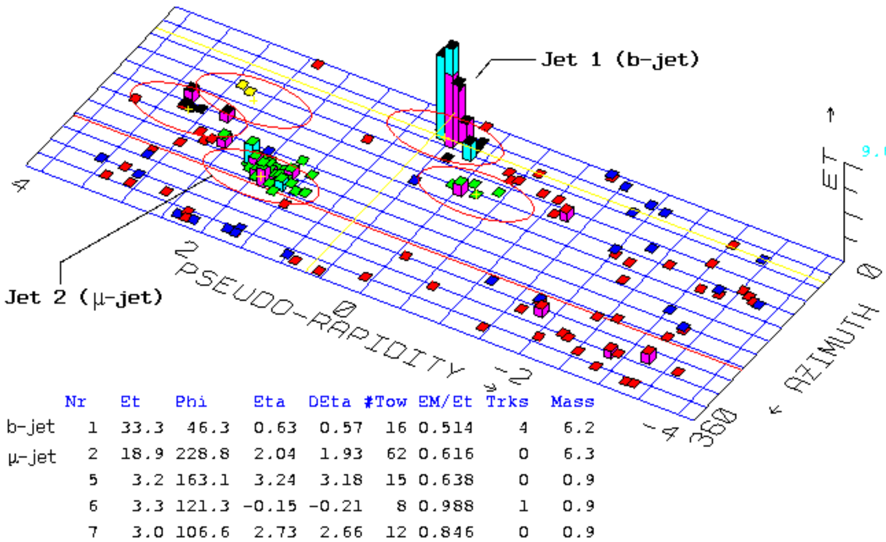


Figure 3.13: Event display showing the CDF calorimeter.

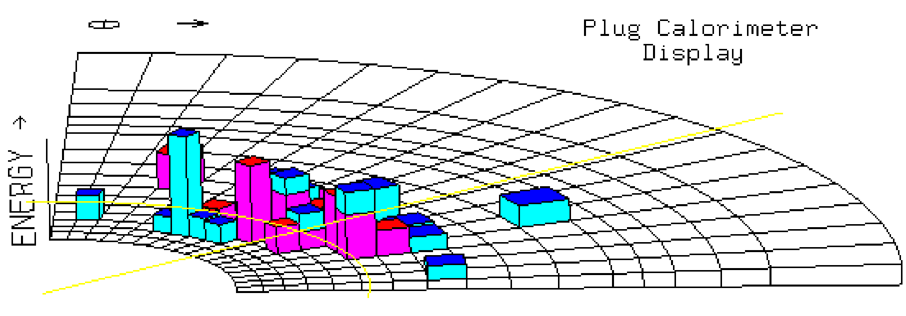


Figure 3.14: Event display showing energy deposition in the plug calorimeter.

height of the block. EM (dark) and HAD (light) energy is shown separately, and the transverse energy scale is indicated. Energy deposition due to low $p_T$ particles from the proton and antiproton remnants can be seen at large positive and negative rapidity. The $b$-tagged jet (Jet 1, or $b$-jet) consists of the prominent energy cluster in the central calorimeter at $\eta = 0.63$ and $\phi = 46°$. The jet associated with the forward muon (Jet 2, or $\mu$-jet) is identified as the energy cluster in the plug calorimeter at $\eta = 2.0$ and $\phi = 228°$, approximately 180° from the $b$-jet. Fig. 3.14 shows a close-up view of the tower-by-tower $\mu$-jet energy deposition in the plug, illustrating the projective geometry of the tower segmentation.

### Jet Identification

Jets are identified as clusters of energy deposition in the calorimeters using a fixed-cone clustering algorithm [32]. The parameters used in clustering are transverse energy, $E_T = E \sin\theta$, and the metric in $\eta$–$\phi$ space, $R = \sqrt{\Delta\eta^2 + \Delta\phi^2}$. Plug and forward towers are combined in $\phi$ sets of three to produce an azimuthal segmentation corresponding to the central calorimeters. The algorithm begins by creating a list of seed towers with $E_T > 1.0\,\mathrm{GeV}$. Preclusters are formed by combining contiguous seed towers of decreasing $E_T$ and within a $7 \times 7$ tower window corresponding to a cone size of $R_0 = 0.7$. Preclusters are grown into clusters by incorporating towers with $E_T > 0.1\,\mathrm{GeV}$ and within a cone of radius $R_0$ around the precluster centroid. Cluster formation uses the true tower segmentation in the plug and forward calorimeters, and the attached towers need not be adjacent to a tower already assigned to the cluster. The centroid position of each cluster is then calculated and the algorithm repeats until two successive passes result in no change to any of the clusters. With this algorithm it is possible to have a tower assigned to more than one jet. This situation is resolved by either merging clusters with shared energy greater than 75% of the smaller cluster, or reassigning all shared towers to the nearest cluster. The cluster centroids are then recalculated using the new tower lists.

The resulting clusters are interpreted as jets and the following variables are defined:

$$\begin{aligned} E &= \sum_{i=1}^{N} E_i, & (3.4) \\ P_x &= \sum_{i=1}^{N} E_i \sin\theta_i \cos\phi_i, & (3.5) \\ P_y &= \sum_{i=1}^{N} E_i \sin\theta_i \sin\phi_i, & (3.6) \\ P_z &= \sum_{i=1}^{N} E_i \cos\theta_i, & (3.7) \end{aligned}$$

where the sum is over towers, $\theta_i$ and $\phi_i$ are computed at the center of each tower, $E$ is the total energy of the jet, and the momentum components determine the jet axis. The jet momentum $P$, transverse momentum $P_T$, and $E_T$ are then calculated as[5]

$$\begin{aligned} P_T &= \sqrt{P_x^2 + P_y^2}, & (3.8) \\ P &= \sqrt{P_T^2 + P_z^2}, & (3.9) \\ E_T &= E\frac{P_T}{P}. & (3.10) \end{aligned}$$

Finally, measured jet energies are corrected for detector effects (including $\eta$-dependent corrections) and underlying event energy using the standard CDF corrections described in Sec. 5.2.

[5]Note that it is usually the case that $E^2 - P^2 > 0$. That is, jets can have a nonzero mass.

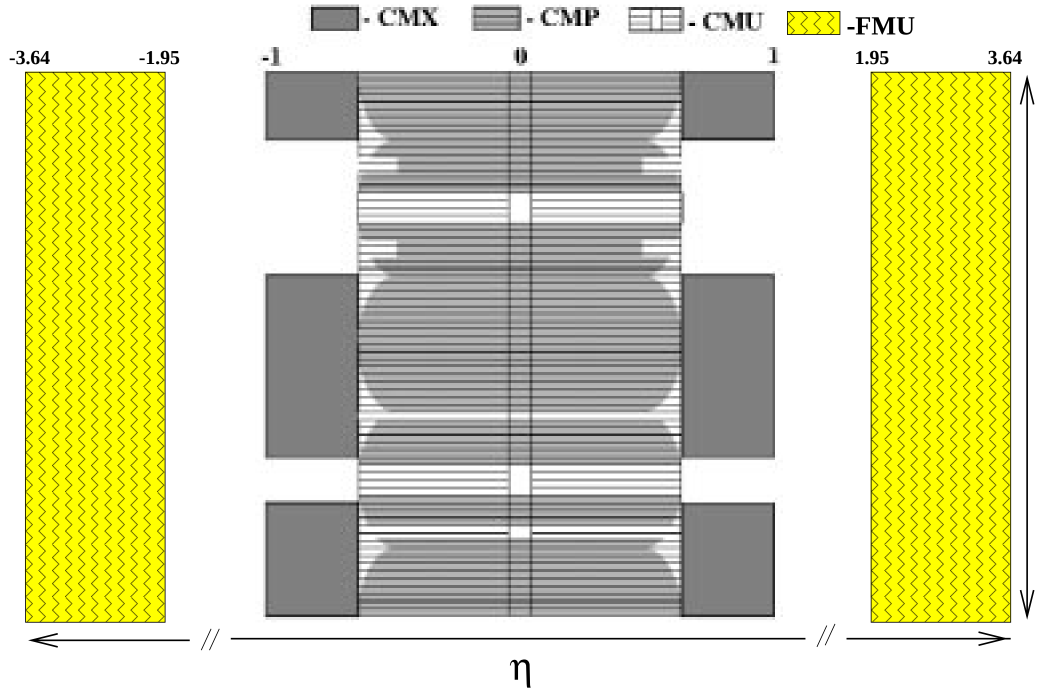


Figure 3.15: A map showing the $\eta$-$\phi$ coverage of the CDF muon system.

### 3.2.3 Muon System

As mentioned in the introduction to this section, muons are highly penetrating particles compared with electrons, photons, and hadrons at comparable energies. This property motivates the location of the muon system outside the many interaction lengths of the hadron calorimeters (cf. Table 3.1). The CDF muon system consists of the central muon (CMU), central muon upgrade (CMP), central muon extension (CMX), and forward muon (FMU) detectors. A map of the muon system $\eta$–$\phi$ coverage is shown in Fig. 3.15. All of the muon detectors are used in this analysis except the CMX, which, given its close proximity to the CMU and CMP systems, and the broad rapidity distribution in $b\bar{b}$ events, does not add significant additional information on the rapidity correlation between the $b$ and $\bar{b}$.

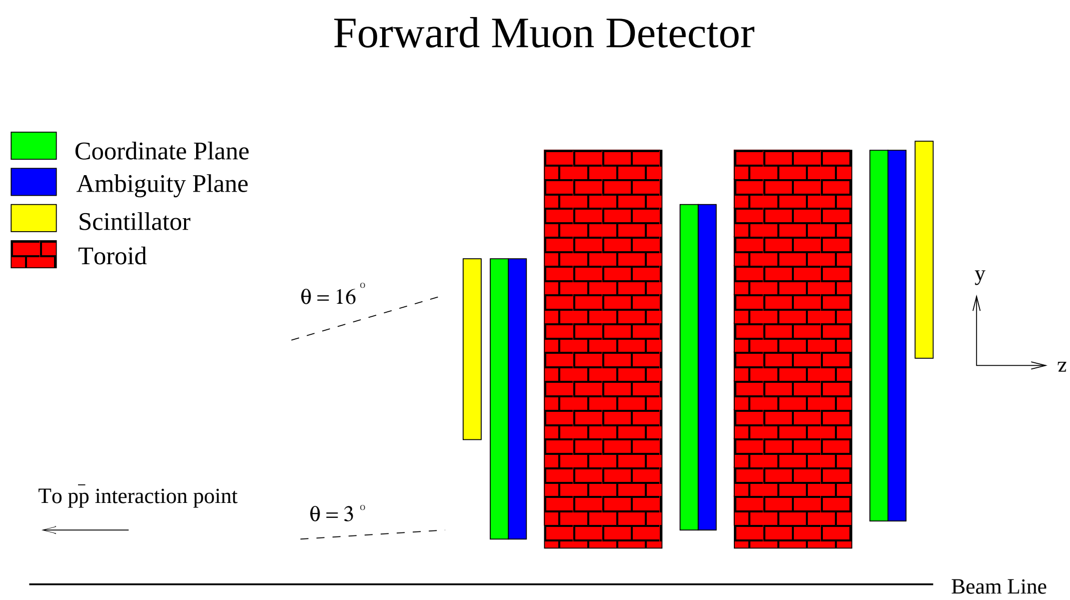


Figure 3.16: Diagram showing the relative location of the FMU detector elements.

**Forward Muon Detector**

Covering the small angle regions between $1.95 < |\eta_D| < 3.64$, the FMU [77] is a magnetic spectrometer consisting of three detector planes of drift chambers surrounding two 1 m thick iron toroids. The first detector plane is located $\approx 10$ m from the interaction point. Fig. 3.16 presents a side-view diagram showing the relative placement of the FMU detector elements. Each detector plane is divided into 24 chambers staggered in $z$ to allow for overlap at the edges. This overlap leads to the 100% $\phi$ coverage indicated in Fig. 3.15. Each chamber consists of two planes of drift cells referred to as "coordinate" and "ambiguity" depending on whether they are closer or further from the interaction point respectively. Coordinate cells are numbered 0–55, while ambiguity cells are numbered 56–95 and are staggered with respect to the coordinate cells to resolve the left-right ambiguity inherent in a drift chamber. Cell size increased with increasing $r$ and $z$ to provide a projective tower geometry for triggering (Sec. 3.3.1). Each drift cell is filled with 50/50 argon-ethane gas and contains a 63 $\mu$m stainless steel sense wire strung along a chord in azimuth. As in the VTX and CTC, charged particles traversing a cell ionize the gas and the resulting electron drift time determines the distance of the particle trajectory from the wire. The single hit spatial resolution is $550\,\mu$m, which includes the detector resolution and survey errors.

The FMU sense wires share the same geometry as the VTX, measuring the $r$ position of a particle trajectory at 6 different postions in $z$. The $\phi$ position of a track is determined by a copper cathode separating the coordinate and ambiguity cells in each detector plane. The cathode plane is segmented into 15 "pads" each covering $5°$ in azimuth and $3°$ in polar angle. Motion of the liberated electrons in the drift field induce a signal on the pad adjacent to the hit cell. Thus, the $\eta$ information from the sense wires could be correlated with the $\eta$ and $\phi$ information from the pads to determine a three-dimensional particle trajectory. In addition, scintillators, segmented $5°$ in $\phi$, cover the front and rear detector planes, providing confirming hits in $\phi$ for use in the trigger. In all then, a muon traversing the FMU detector consists of 6 drift chamber hits, 3 cathode pad hits, and 2 scintillator hits; although detector inefficiency could lead to missing hits, while secondary particle production from delta rays and random background typically provided additional drift chamber hits.

The FMU toroids are energized with four 28-turn copper coils each carrying a current of $600A$, providing an azimuthal magnetic field varying from 1.96 T at the inner radius (50 cm) to 1.58 T at the outer radius (380 cm) [78]. FMU tracks were reconstructed from drift chamber hits using an iterative fitting procedure which took into account multiple scattering and energy loss in the calorimeters and toroids [79]. The fitting code could perform a fit with or without a $z$ vertex constraint, where the parameters in the fit are the radial position at $z = 0$, the tangent of the initial polar angle, and the curvature of the trajectory in the magnetic field regions. The track momentum is determined from the fitted curvature,

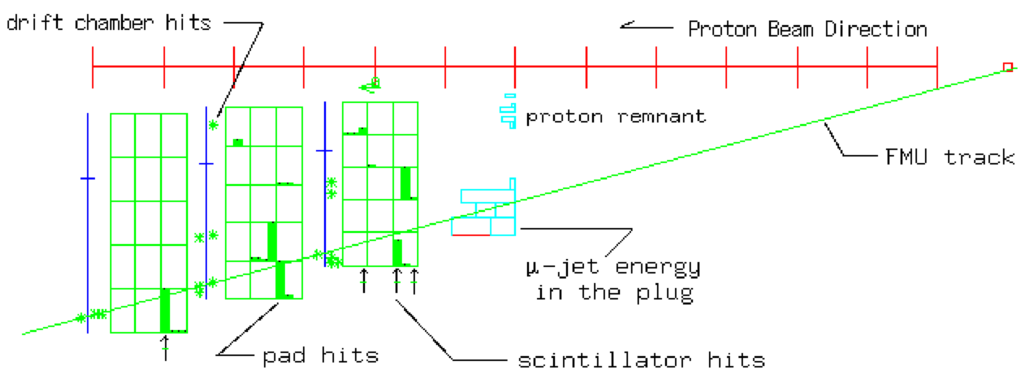


Figure 3.17: FMU Event display showing drift chamber, pad, and scintillator hits, as well as the reconstructed muon track (see text for details).

and the resulting resolution is $\delta p_T/p_T \approx 15\%$, dominated by multiple scattering. For low momentum muons, the resolution is momentum independent because both the magnetic field and multiple scattering angular deflections are inversely proportional to momentum (Ref. [66], Chapter 2).

Fig. 3.17 shows a side-view display of the FMU information for our sample event. The beam line is indicated by the top scale, which marks off 1 m increments, and the small square at the right shows the IP. The detector planes are represented by the vertical lines at approximately 10, 11.5, and 13 meters from the IP. The reconstructed track is seen to coincide with several wire hits (asterisks), as well as pad (vertical bars) and scintillator (arrows) hits. As mentioned above, a muon would often produce more than the nominal 6 wire hits, and four additional hits are associated with the track in this event. The vertical histogram just in front of the first detector plane indicates the relative location of energy deposition in the plug calorimeter corresponding to the $\mu$-jet cluster shown in Fig. 3.14. The muon is clearly embedded in the jet, which is one of the signatures of $b$ decay used to separate signal from background. The smaller energy deposited at higher rapidity is most likely due to low $p_T$ particles from the proton remnant.

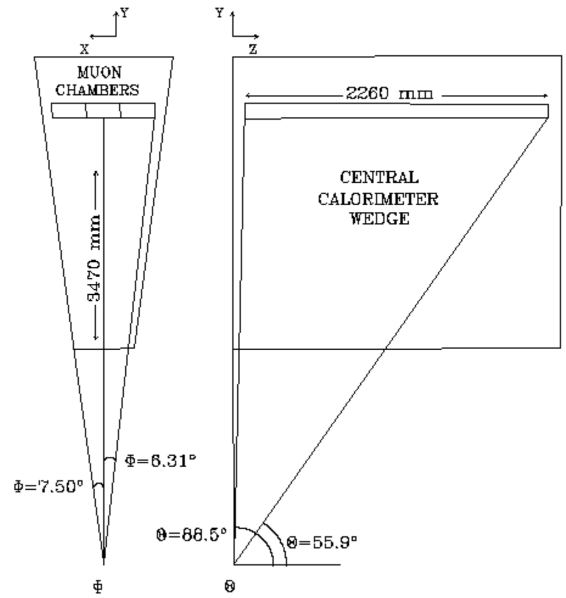


Figure 3.18: A diagram showing the relative location of the central muon system inside the central calorimeter wedge.

**Central Muon Detectors**

The CMU [80] consists of 72 modules embedded in the 24 central calorimeter wedges at a radius of 3470 mm, as shown in Fig. 3.18. Each wedge contains 3 modules, with each module subtending 4.2° in azimuth. Due to the gaps between sets of three modules, the CMU azimuthal coverage is 84% in the pseudorapidity region $|\eta_D| < 0.6$. In addition, there is a 3° polar angle gap at $z = 0$ which further reduces the geometric coverage of the detector.

Fig. 3.19 shows one of the CMU modules, which consists of four layers containing four rectangular drift cells each. The drift cells contain a single 50 $\mu$m stainless steel wire strung longitudinally down the length of each tube. Drift cells in the second and fourth layers from the IP have their wires aligned radially with the beam axis, while layers 1 and 3 are aligned along a radial that is offset by 2 mm at the center of the module. This offset not only allows for resolution of the left-right

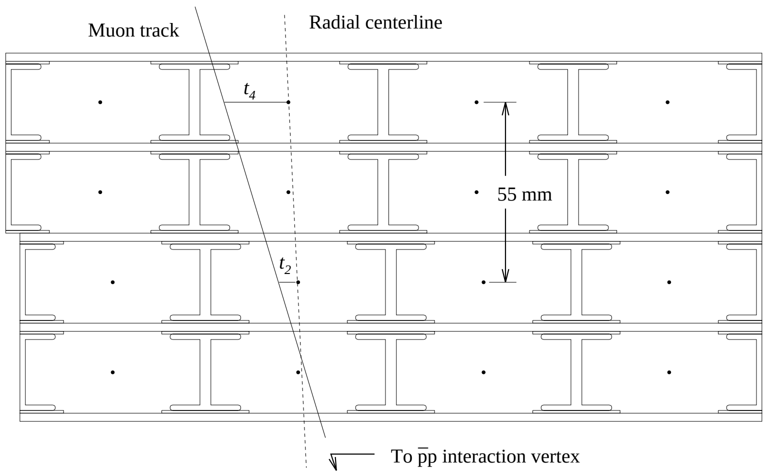


Figure 3.19: Schematic diagram of a CMU module (see text for details).

ambiguity, but also allows a coarse momentum measurement for use in triggering. The momentum measurement relies on the fact that low momentum particles will emerge from the magnetic field at an angle with respect to the radial direction. The offset between layers (1,3) and (2,4) results in a drift time difference that is inversely proportional to the transverse momentum of the particle.

A particle will traverse approximately 5.4 absorption lengths before reaching the CMU chambers. Thus, approximately 1 out of every 221 high momentum hadrons will penetrate the calorimeters without interacting, proceeding on to leave hits in the CMU chamber. This hadronic "punch-through" represents a significant background in the CMU[6]. To address this problem, in 1992, 60 cm of steel absorber were placed beyond the the CMU system, and an additional four layers of axially aligned drift chambers were installed behind the steel. Due to the geometry of the central detector, the central muon upgrade (CMP) [81], has a box shape which limits the combined coverage of the CMU-CMP system to 53% of the solid angle for $|\eta_d| < 0.6$. Particles that penetrate to the CMP traverse 7.8 interaction lengths

[6]Including the 2 m of toroid iron, particles must traverse at least 18 interaction lengths to produce 6 hits in the FMU. The punch-through background is therefore negligible.

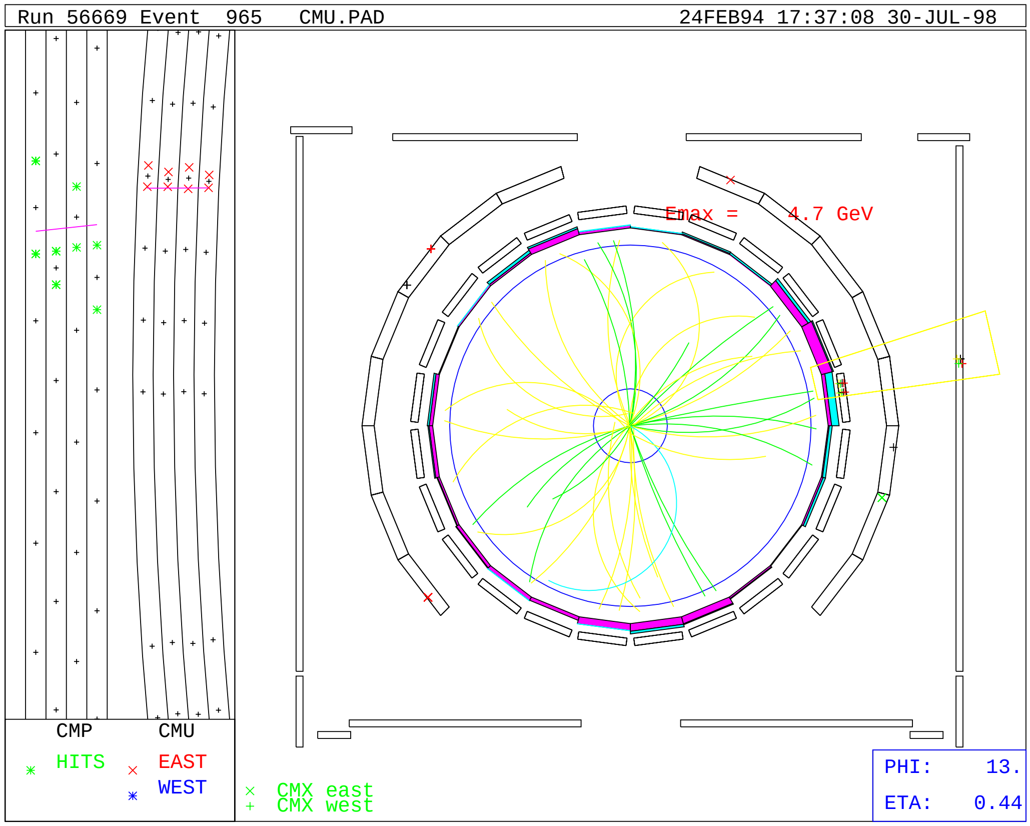


Figure 3.20: Event display showing all central detector components.

at $\eta = 0$, significantly reducing the punch-through background.

Fig. 3.20 displays central muon information for Event 965 in Run 56669. The inner circle of the main plot shows the CTC volume, with reconstructed tracks indicated by line segments. Energy deposition in each of the 24 central calorimeter wedges is indicated just outside the CTC. The CMU modules are pictured just beyond the calorimeter, the semi-circular arcs represent the CMX system, and the box-like geometry of the CMP is seen as the set of chambers furthest from the IP.

Muon hits are indicated by small plus signs. At $\phi = 13°$, a relatively high $p_T$ CTC track is pointing at a set of CMU and CMP hits. The smaller window on the left shows a close-up view of the CMU and CMP systems (not to scale) for the region bordered by the rectangle in the main view. Sense wire locations in both detectors are shown as small plus signs, while the CMU and CMP hits are shown as crosses and asteriks respectively. Both possible positions for each hit are shown in this view. Well-defined muon segments are clearly visible (straight lines) in both detectors, which line up in azimuth within multiple scattering errors. For this thesis, central muon candidates are defined as a CTC track matching both a CMU and CMP segment in $\phi$ and $z$. Charge division in the CMU is used to measure the $z$ position of the muon segment. The matching requirements applied in the trigger are discussed in Sec. 3.3, while the offline requirements are listed in Sec. 5.4. Identified central muon candidates are referred to as CMUP muons.

### 3.2.4 Luminosity Monitor

Luminosity calculations using measurements of the Tevatron lattice functions have historically been inaccurate (Chapter 4). CDF monitored the instantaneous luminosity online using a set of dedicated scintillators on either side of the interaction point. The beam-beam counters (BBC), as they were called, consisted of four planes of four crossed counters providing hit or miss information on the passage of particles, Fig. 3.21. The entire system covered the pseudorapidity range $3.24 < |\eta_D| < 5.90$ and was located just in front of the forward electromagnetic calorimeters.

In addition to providing a measure of the instantaneous luminosity, the BBC was also used as a “minimum bias” trigger, meaning that no physics requirements other than the presence of an inelastic $p\bar{p}$ collision were imposed. Minimum bias data samples were used in many diagnostic studies of detector performance and beam profile parameters. For this analysis, I use minimum bias data to determine the longitudinal profile of the beam during Run 1B.

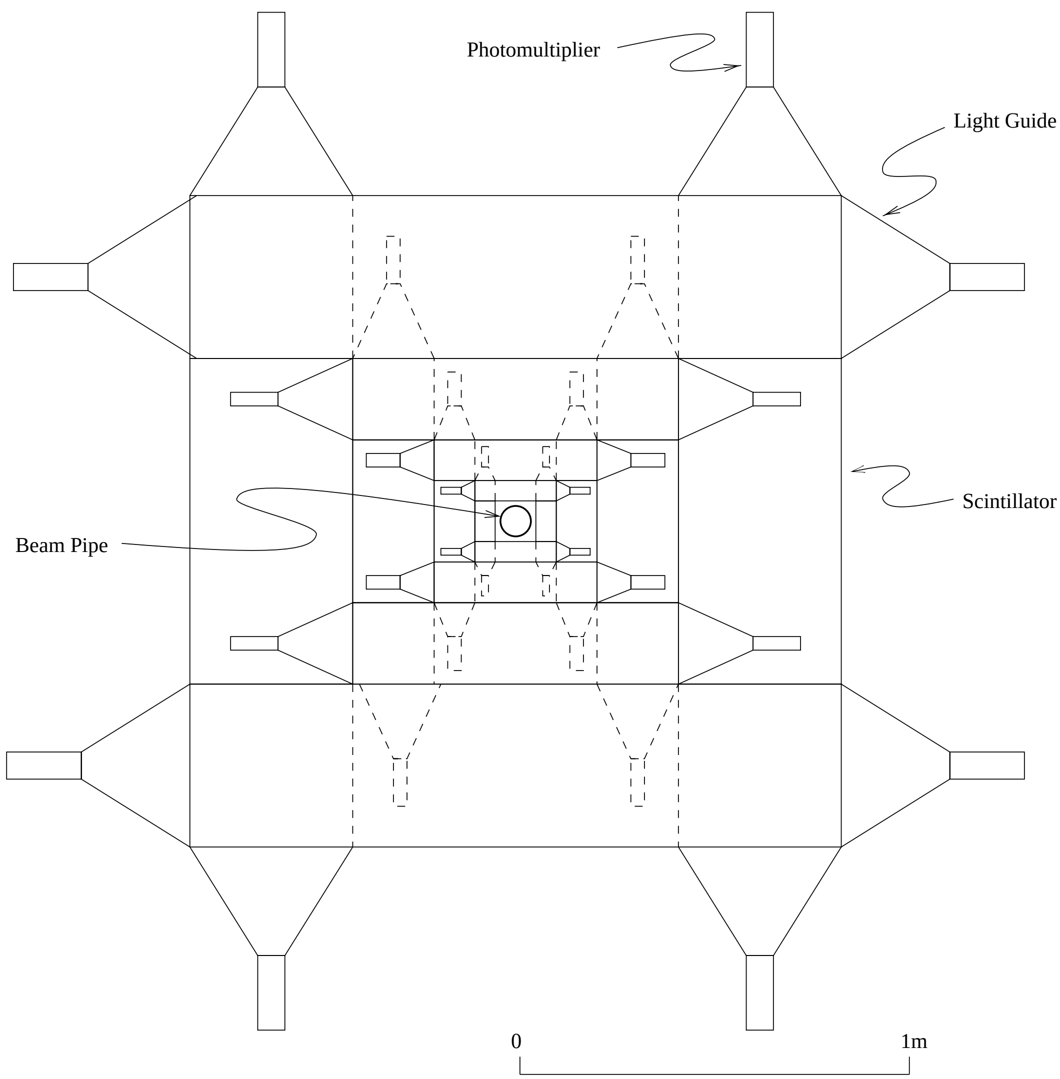


Figure 3.21: A schematic view showing one set of beam-beam counters.

## 3.3 Data Acquisition

During Run 1B, beam crossings occured in the CDF collision hall every $3.5\,\mu$s. With an average number of $p\bar{p}$ interactions per crossing $> 1$, the total collision rate seen by the CDF was $> 286$ kHz. The different detector elements comprised over 100,000 individual electronic signals that had to be amplified, modified, and assembled into a coherent snapshot of each event. A given event produced approximately 165 kB of digitized detector data, which amounts to a data flow of 47 GB/s. However, the preferred permanent mass storage device, 8 mm tape, could only be written to at $5-10$ Hz. It was the job of the CDF data acquisition (DAQ) system to filter and record the interesting events while minimizing detector deadtime[7]. The task of filtering uninteresting low energy inelastic collisions while accepting interesting high energy parton-parton collisions was performed by the trigger system, which accessed fast detector data in parallel with the main data pathway.

A block diagram of the CDF DAQ system is shown in Fig. 3.22. The lowest level (front end) of this system was the detector itself. Analog signals were typically pre-amplified at the detector and sent along twisted pair or coaxial cables to electronics crates inside the collision hall, where further amplification took place. The amplified signals were then sent upstairs to the Counting Room where they were digitized with either analog-to-digital (ADC) or time-to-digital (TDC) converters, depending on the detector. The digitized data then awaited the outcome of the first and second level trigger decisions on whether the current event would be readout, or the buffers cleared to make room for the next crossing.

[7] Deadtime refers to the length of time the detector is unable to accept data from subsequent $p\bar{p}$ collisions while reading out the current event.

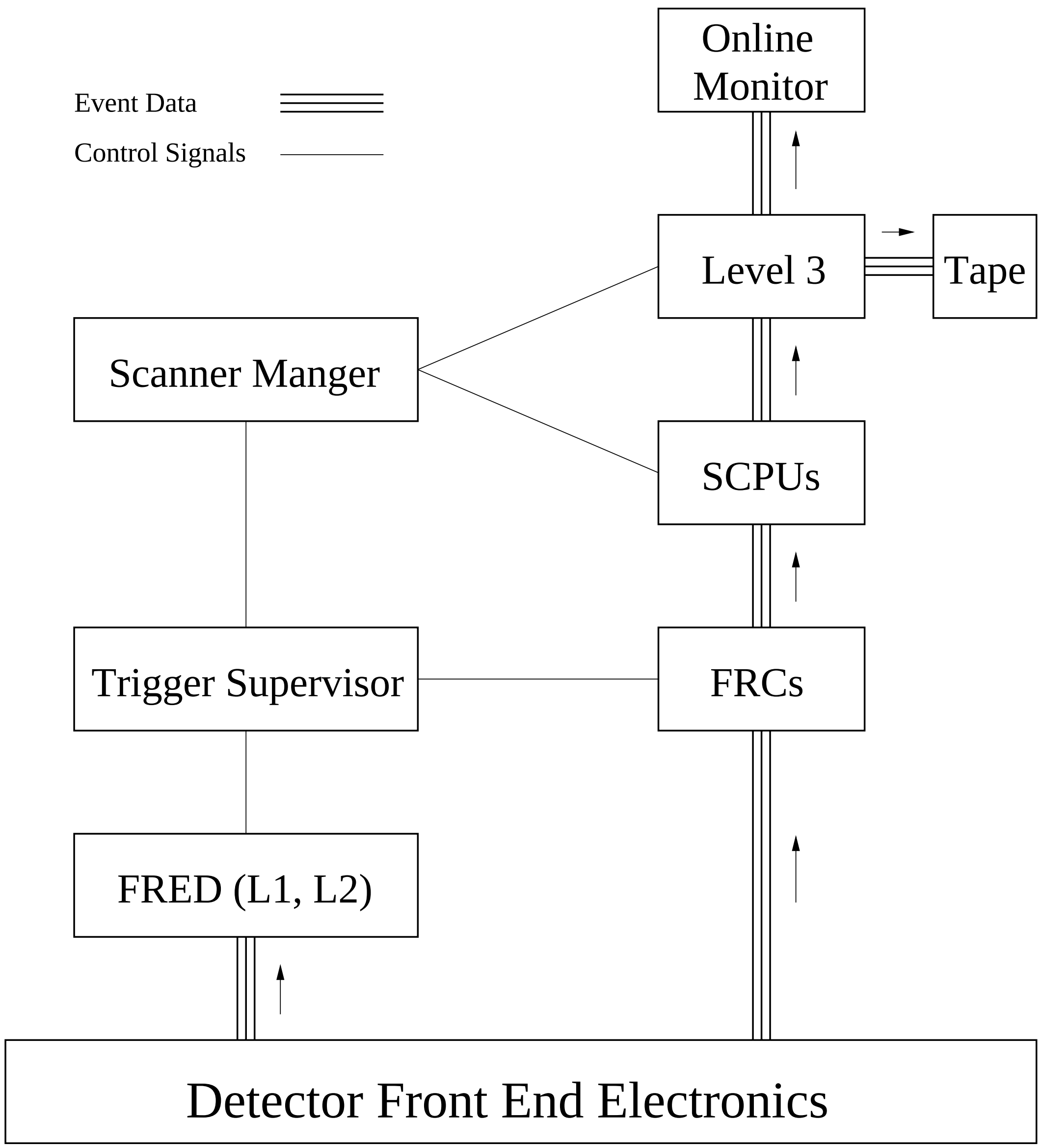


Figure 3.22: Simplified block diagram of the CDF data acquisition system.

### 3.3.1 Trigger System

The CDF trigger system [82] is divided into first and second level hardware triggers, and a third level software trigger based on a version of the offline reconstruction package optimized for speed. This analysis uses data acquired with the inclusive central muon and forward muon+jet triggers, and I will describe the various requirements imposed by each of these triggers as I describe the different levels of the system.

#### Level 1

The level 1 trigger was designed to be deadtimeless, meaning a decision had to be made within the $3.5\,\mu s$ crossing time, or all data was cleared from the buffers in time for the next crossing. This requirement limited the processing to simple logic algorithms applied using only calorimeter and muon detector data. The trigger decision was controlled by a dedicated FASTBUS module (FRED) that received 'yes' or 'no' results from each of the ten level 1 physics triggers, and passed on the logical OR of all the these results to another FASTBUS module, the trigger supervisor. The trigger supervisor was the interface between the trigger and the rest of the DAQ, and controlled whether or not the data was readout based on the signals received from FRED. The level 1 accept rate was $\sim 1\,\mathrm{kHz}$.

Table 3.2 presents a summary of the ten level 1 triggers. There were three calorimeter triggers, six muon triggers, and one combined calorimeter-muon trigger. The level 1 calorimeter triggers used fast analog signals and required at least one tower above a programmable $E_T$ threshold. The tower size at this level of the trigger was $\Delta\eta_D \times \phi = 0.2 \times 15°$, with EM and HAD towers being considered separately for each of the calorimeters. One inclusive trigger imposed high $E_T$ thresholds, $\approx 10\,\mathrm{GeV}$ for the central EM and HAD and the plug EM calorimeters,

**Summary of Level 1 Triggers**

| Name | Description | Required? |
|---|---|---|
| L1_CALORIMETER | Single tower above threshold | No |
| L1_4_PRESCALE_40 | Single tower above threshold, prescaled | No |
| L1_DIELECTRON_4 | Dielectron trigger $p_T > 4\,\mathrm{GeV}$ | No |
| FMU_L1_7_5 | Single FMU, rate limited at $0.6\,\mathrm{Hz}$, $p_T > 7.5\,\mathrm{GeV}/c$ | Yes |
| TWO_FMU_L1_4_5 | FMU dimuons, rate limited $0.6\,\mathrm{Hz}$, $p_T > 4.5\,\mathrm{GeV}/c$ | No |
| CMU_CMP_6PT0_NO_HTDC | CMU$\otimes$CMP $p_T > 6\,\mathrm{GeV}/c$, Hadron-TDC for CMNP | Yes |
| CMX_10PT0_HTDC | CMX with Hadron-TDC | No |
| TWO_CMU_3PT3 | CMU$\otimes$CMU, $p_T > 3.3\,\mathrm{GeV}/c$ | No |
| TWO_CMU_CMX_3PT3 | Dimuon trigger, $p_T > 3.3\,\mathrm{GeV}/c$ | No |
| CEM_CMU_OR_CMX | $e$-$\mu$ trigger, $p_T^e > 4\,\mathrm{GeV}/c$, $p_T^\mu > 3.3\,\mathrm{GeV}/c$ | No |

Table 3.2: Summary of level 1 triggers. The two triggers used in this thesis are indicated.

and $\approx$ 50 GeV for the remaining detectors, while a second "prescaled"[8] trigger used a lower threshold (4 GeV) in the central region. Finally, a "dielectron" trigger required two EM towers above 4 GeV as the initial signal of an event with two high $p_T$ electrons. The calorimeter triggers were not used in this analysis.

The level 1 CMU trigger looked at sets of two hits in each trigger tower. A trigger tower comprised the four drift cells aligned along the radial direction and subtending an angle of 4.2° (cf. Fig. 3.19). As already mentioned, a coarse $p_T$ measurement was achieved by exploiting the fact that low momentum tracks emerge from the magnetic field at an angle with respect to the radial direction, and therefore, produce different arrival times on the radially aligned wires. Two $p_T$ thresholds were implemented in Run 1B, 3.3 and 6.0 GeV/$c$. The trigger used for this analysis, CMU_CMP_6PT0_HTDC, required at least one CMU segment satisfying the high $p_T$ threshold and a matching CMP segment within a $\phi$ window predetermined by multiple scattering. If there was no CMP segment match in a region where one was expected, a minimum ionizing signal in the corresponding central HAD calorimeter wedge was required. Since I explicitly require the CMP stub this additional requirement has no effect on the analysis.

The FMU level 1 triggers employed pattern recognition units to search for a set of 6 drift chamber hits, 3 pad hits, and 2 scintillator hits consistent with the expected signature of a high $p_T$ muon originating from the interaction point. While one set (NUPU)[9] searched for track candidates consisting of 6 wire hits satisfying one of the predetermined trigger patterns (roads) in $\eta$, a second set (PPU)[10] identified combinations of 3 pad hits matching each other within 5° in $\phi$

[8] Prescaled triggers had their rates reduced by accepting only 1 out of $p$ triggers, where $p$ was the prescale factor. The above mentioned calorimeter trigger had a prescale factor of 40.

[9] NUPU stands for new-half-octant-pattern-unit, which was descended from the half-octant-pattern-units (HOPU) used in Tevatron Run 0 (1988-1989).

[10] PPU stands for pad-pattern-unit.

and $3^\circ$ in $\theta$, and matching a front-rear scintillator pair within $5^\circ$ in $\phi$.

The preset trigger roads exploited the projective geometry of the FMU drift cells to identify hit patterns corresponding to rough $p_T$ thresholds. The technique is illustrated in Fig. 3.23. Most particles with $p_T > 7.5\,\mathrm{GeV}/c$ will follow a relatively straight line through the detector, producing hits on corresponding cells in successive detector planes (solid line). Patterns that satisfy the so-called "100% road" were allowed to deviate from a straight line by at most one cell. The set of ten 100% roads corresponding to a particle entering the front detector plane through coordinate wire 44 are listed in the figure. Lower momentum particles were deflected more in the magnetic field and scattered more in the toroids. To account for this, an additional set of 300% roads allowed for more deviation from a straight line trajectory. An example of a particle satisfying one of the 300% roads corresponding to cell 44 is shown as a dashed line in Fig. 3.23.

The inclusive FMU trigger used in this analysis, FMU_L1_7_5, required the presence of a track candidate satisfying a 100% road, along with a pad-scintillator match in the same octant. This trigger was approximately 50% efficient for muons with $p_T \approx 7.5\,\mathrm{GeV}/c$. The dimuon trigger required two track candidates satisfying a 300% road in coincidence with pad-scintillator matches in each candidate octant. The dimuon trigger was 50% efficient at $p_T \approx 4.5\,\mathrm{GeV}/c$. Due to the high luminosity delivered by the Tevatron during Run 1B, the FMU triggers were rate-limited to 0.6 Hz, meaning that FRED inhibited the FMU trigger bits for 1.67 s after a level 1 accept. The loss of valid FMU level 1 triggers is treated as a trigger inefficiency, the calculation of which I will describe in Chapter 4.

### Level 2

If FRED returned a level 1 accept, the trigger supervisor signaled the data acquisition system to inhibit further data taking for approximately $20\,\mu\mathrm{s}$ while the level

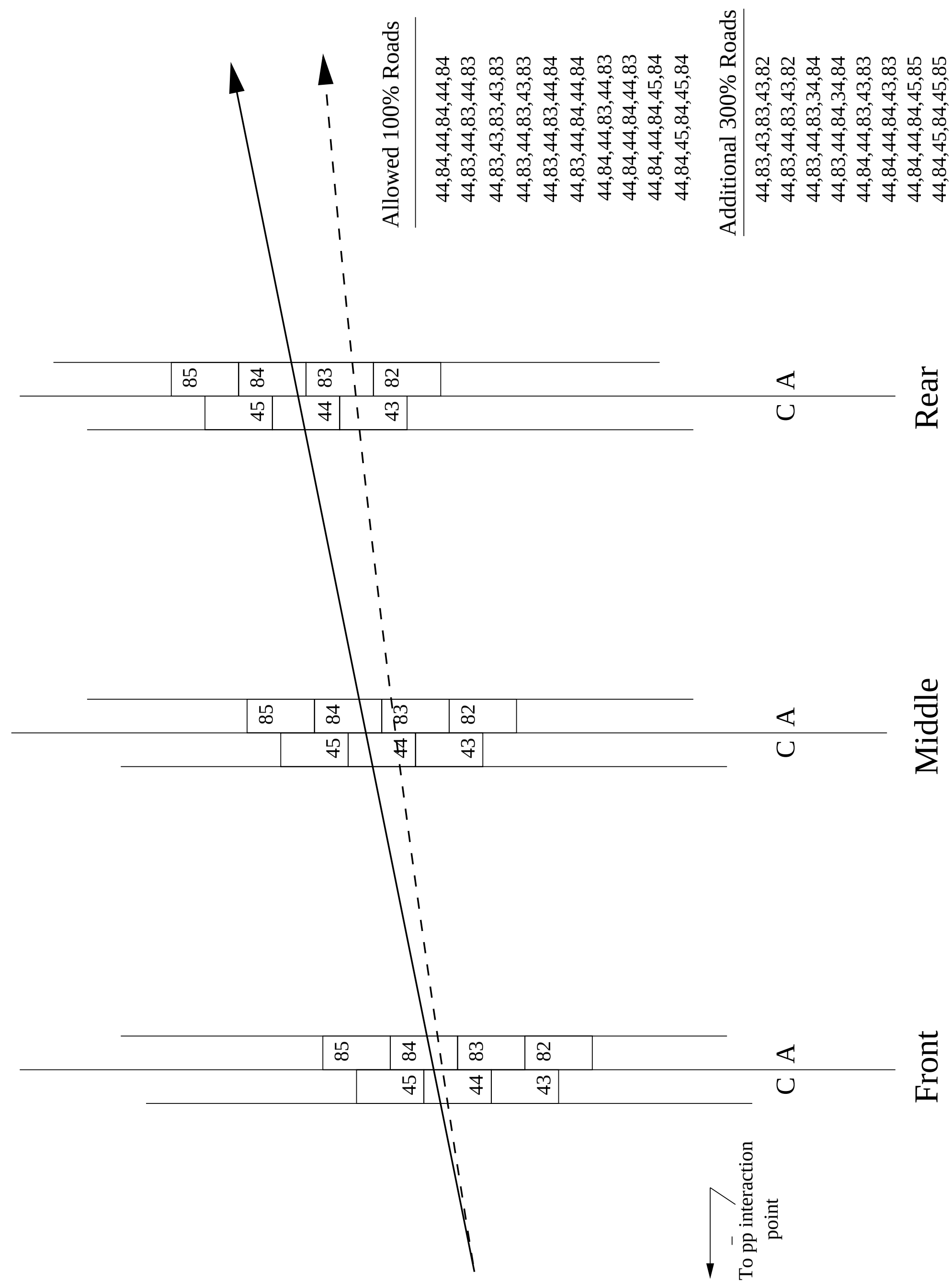


Figure 3.23: Diagram illustrating the definition of the FMU level 1 100% and 300% trigger patterns (Adapted from K. Byrum, Ph.D. Thesis, University of Wisconsin, Madison, 1992).

2 trigger made its decision. With more time to process information, the level 2 trigger could afford to perform higher level data manipulation, including simple jet clustering, two-dimensional track reconstruction, and muon-track matching. Over 40 level 2 triggers were active at any one time during Run 1B. Wherever possible, "physics objects" (electrons, photons, muons, and jets) were constructed and checked against varying kinematic requirements.

The level 2 calorimeter clustering algorithm was based on the preclustering algorithm mentioned above (Sec. 3.2.2). Clusters were grown around seed towers by incorporating contiguous "shoulder" towers above a given threshold that were not already part of a separate cluster. Again, none of the calorimeter triggers are used in this analysis.

Simple tracking in the transverse plane was performed by the CDF central fast tracker (CFT) [83]. The CFT was a dedicated hardware track processor which used fast timing information from the CTC to identify eight preprogrammed hit patterns corresponding to $p_T$ bins from 2.2 to 27 GeV/$c$. Due to the 45° slant of the CTC sense wire planes, a high $p_T$ track was guaranteed to pass close to at least one sense wire per superlayer. These "prompt" hits provided the fast timing inputs to the CFT. Beginning with a prompt hit in the outer superlayer, the CFT searched the inner axial superlayers for other prompt hits along the predetermined roads. Both possible signs of curvature were checked, and a CFT track satisfying a given $p_T$ bin also fired all lower momentum bins. The momentum resolution of the CFT was approximately 3.5%.

The level 2 central muon triggers used in this analysis, CMUP_CFT_7_5_5DEG and CMUP_CFT_12_5DEG, required a match between a CMUP segment and a CFT track within 5° in $\phi$ at the outer CTC superlayer. The segment-track match was required to pass either the 7.5 (bin 4) or 12 GeV/$c$ (bin 5) trigger thresholds. Both triggers were used because the lower $p_T$ trigger path was dynamically prescaled during Run 1B (see Chapter 4).

No additional requirements were placed on the FMU candidates identified at level 1. The level 2 FMU trigger was therefore auto-accept. Including all triggers, the typical level 2 accept rate was $15 - 20\,\mathrm{Hz}$.

### Data Readout

If FRED determined that one of the level 2 triggers had passed, the trigger supervisor sent a signal to the FASTBUS readout controllers (FRCs) to begin reading the stored detector data in their crates. When all of the FRCs were finished reading data the trigger supervisor cleared the detector front end and sent a message to the scanner manager that the FRC buffers were full. The scanner manager was a VME[11] based module containing a Synergy Corporation CPU running the VxWorks operating system. The scanner manager controlled the flow of data between the front end FASTBUS network and the level 3 processor farm via the scanner CPUs (SCPU). Each SCPU was a VME module, similar to the scanner manager, programmed to readout a specific set of FRCs over a 16-bit scanner bus. When all SCPUs had finished reading out their respective FRCs, the scanner manager instructed them to send their event fragments to an available level 3 buffer. At this point, the entire event was contained in one of the level 3 receiver buffers, where it awaited reformatting and passage to one of the level 3 processor nodes. It took $\sim 1\,\mathrm{ms}$ to readout the data for one event.

### Level 3

The level 3 processor farm comprised eight "boxes" containing eight processors each. Four of the boxes were Silicon Graphics, Inc. (SGI) Challenge machines supporting R4400 CPUs, while the remaining four were SGI Power Servers with

[11]VME stands for Versa Module Eurocard, and is a crate based modular electronics package similar to FASTBUS.

R3000 CPUs. Each box was logically divided into receiver, reformatter, reconstruction, and dispatcher subsystems. As already mentioned, the receiver acted as an input buffer for the event data sent from the SCPUs. The event reformatter combined the various data fragments into the CDF YBOS data format. The YBOS format was essentially a long one-dimensional array consisting of detector-specific data banks linked end-to-end. Once the event was in YBOS format it was sent to one of the eight processors running the CDF level 3 executable, a modified version of the full offline FORTRAN program optimized for speed. Several events could be processed simultaneously at level 3 and the temporal ordering of output events was not always coincident with the input.

The two level 3 CMU triggers used in this analaysis, MUOC_CMU_CMP_6 and MUOB_CMU_CMP_8, accessed full three-dimensional CTC tracking information and required a CMUP segment matching a CTC track with $p_T > 6$ or $8\,\mathrm{GeV}/c$ respectively. The track-stub matching was implemented by extrapolating CTC tracks out to the radius of the CMU and CMP detectors. If the extrapolated position of the track matched the stub positions within a tolerance determined by multiple scattering, the stubs were assigned to that track. The higher momentum trigger required a match within $\sqrt{14}\sigma$ in $z$ for the CMU, and $\sqrt{11}\sigma$ in $\phi$ for both the CMU and CMUP, while the lower momentum applied a straight distance cut of 10 cm on the CMU stub only. Approximately 7 million events were collected with the central muon trigger during the data taking period considered for this analysis.

The FMU level 3 triggers performed track reconstruction using all hits in the detector, not just the hits responsible for the level 1 trigger. In addition, tracks using only 5 out of 6 possible hits were also reconstructed. Because the $z$ position of the event vertex was not known at level 3, the track fit was performed without the vertex constraint. The trigger used in this analysis, MUOB_FMU_4_JET_20, required at least one 6-hit track with $p_T > 4\,\mathrm{GeV}/c$. Although the detector was instrumented down to $|\eta_D| \approx 3.6$, large backgrounds near the Tevatron beam pipe restricted the active trigger coverage to the outer radius region $1.9 < |\eta_D| < 2.7$. Further background suppression of sources not associated with the $p\bar{p}$ collision was accomplished by requiring the sum of hits on coordinate wires 14-55 and ambiguity wires 63-95 in the trigger octant to be less than 31. Finally, real muon backgrounds from the decay of vector bosons and light mesons were suppressed relative to heavy flavor decays by requiring at least one jet in the event with uncorrected $E_T > 20\,\mathrm{GeV}$. No specific jet triggers were required, only that there be a cluster anywhere in the calorimeter system above the given threshold.

Events that passed one of the level 3 triggers were sent to one of three data loggers (A, B, and C), which temporarily stored the data files on disk. The events for a given data taking run were organized into files corresponding to approximately $7\,\mathrm{nb}^{-1}$ of integrated luminosity. Events passing high priority, low cross section triggers (e.g. $Z$'s and $W$'s) were sent to stream A, while the majority of remaining events were set to stream B. Stream C comprised low priority specialty triggers not intended to be used as the basis for a complete dataset. The low momentum CMUP trigger used in this analysis, mostly consisting of events with $6 < p_T^{\mu} < 8\,\mathrm{GeV}/c$, was a stream C trigger. Online monitoring programs called consumer servers continually accessed a portion of the current data on disk for use in diagnostics by the on-duty CDF shift crew. When a data logger had recorded a sufficient number of events to fill one 8 mm tape, the disk-resident data was written out to permanent storage. These "raw" data tapes were the starting point for all subsequent data analysis performed at CDF.

# Chapter 4

# Luminosity

In the context of a scattering experiment, the term "luminosity" refers to the incident flux of colliding particles, and the particle flux is related to the total number of collisions taking place per unit time. Therefore, to measure a cross section one needs to know both the reaction rate for the process under investigation, and the beam luminosity.

It has already been mentioned that calculations of the absolute Tevatron luminosity have not been accurate (Sec. 3.1.3). Furthermore, the CDF luminosity calculation, while more accurate than the accelerator estimate, is only known with an accuracy of 8% [84]. One of the primary motivations for performing a ratio measurement was to eliminate this irreducible error. This was accomplished by filtering the forward and central muon trigger samples with the same data file list. The two samples therefore have equal luminosity by definition, and the cross section ratio is insensitive to the luminosity normalization. However, due to the rate limit applied to the FMU level 1 trigger, and the prescale factor applied to the CMUP level 2 trigger, knowledge of the luminosity remains essential to the prescale efficiency calculations.

I begin this chapter by outlining the two general methods used to calculate luminosity at a colliding beam machine, followed by a description of the specific method used by CDF during Run 1B. I then conclude with a detailed description of my calculation of the prescaled luminosity for the forward and central muon triggers used in this analysis.

## 4.1 Two Methods for Calculating Luminosity

### 4.1.1 Absolute

In principle, for any controlled experiment it should be possible to calculate the luminosity from the parameters of the experimental setup. Such an estimate is referred to as an absolute luminosity calculation, and usually relies on a formula similar to Eq. 3.2. In practice, however, the situation is more complicated. A more accurate estimate of the luminosity is given by [63]

$$\mathcal{L} = \frac{f}{4\pi\sqrt{\beta_x\beta_y}} \sum_i^{N_B} \sum_j^{N_B} \frac{N_i \bar{N}_j F(\sigma_{\lambda i}, \sigma_{\lambda j}, \beta_x^*, \beta_y^*)}{\sqrt{\frac{1}{4}(\epsilon_{xi} + \bar{\epsilon_{xj}})(\epsilon_{yi} + \bar{\epsilon_{yj}})}} \tag{4.1}$$

where the sum is over particle ($i$) and antiparticle ($j$) bunches, $N_{i,j}$ are the bunch intensities, $f$ is the orbital frequency, $\epsilon$ and $\beta$ describe the area and shape of the beams in phase space respectively [85], and $F$ is a function describing the longitudinal profile of each bunch, with $\sigma$ being the bunch length. The function $F$ is usually taken to be either gaussian or triangular.

Calculation of the luminosity using Eq. 4.1 requires measurements of bunch intensity and the transverse and longitudinal profiles. At the Tevatron, bunch intensity and longitudinal extent were both measured with a resistive wall current monitor, which detected the time varying magnetic field produced by the passage of the beam [86]. The transverse profile was measured with two methods. The "flying wire" method passed a 30 $\mu$m diameter carbon wire through the beam at a speed of 5 m/s. Collisions between the beam and wire produced secondary pions that were detected downstream by plastic scintillators. The second method exploited the synchrotron radiation produced when the beam particles passed through one of the Tevatron dipole bending magnets. A ccd camera detected the synchrotron photons, producing a two-dimensional image of the beam in the transverse plane.

The estimated uncertainty on the beam parameter measurements was $5-10\%$, so the expected total uncertainty on the luminosity was $\approx 10\%$. Luminosity measurements during Tevatron Run 0 (1988-9) were consistent with this estimate [63]. However, similar measurements conducted during Run 1B produced results differing from the CDF and DØ experiments by 50% [86]. The method is currently being scrutinized to determine the source of the error.

### 4.1.2 Relative

An alternative to the absolute luminosity calculation is to measure physics cross sections relative to some other process for which the cross section is known. Thus, if one counts $N$ signal events and $N_0$ events corresponding to a reference process with known cross section $\sigma_0$, the unknown cross section is given by,

$$\sigma = \sigma_0 \frac{N}{N_0}. \tag{4.2}$$

For the luminosity measurement not to dominate the total uncertainty on $\sigma$, the systematic uncertainty on $\sigma_0$ must be small, and $\sigma_0$ must be larger than $\sigma$ so that the statistical uncertainty on $N_0$ will be less than for the signal process.

The relative luminosity method works very well at $e^+e^-$ colliders, where the reference process is small angle elastic (Bhabha) scattering. For example, at the Large Electron Positron (LEP) collider at CERN, the Bhabha scattering process has been calculated to a precision of 0.11% [87]. Furthermore, the experimental signature of an electron-positron pair with equal and opposite momenta, corresponding to the beam energy, is relatively easy to detect. As a result, luminosity measurements at the four LEP experiments are accurate to $\sim 0.1\%$ [88].

## 4.2 CDF Luminosity Measurement

At a hadron collider, such as the Tevatron, the total collision cross section cannot be calculated using perturbation theory because hadrons are composite objects. Hadron colliders therefore lack a precisely calculable reference process with which to measure the machine luminosity. However, the $p\bar{p}$ cross section can be measured experimentally using a luminosity-independent method (defined below), and the rate of inelastic collisions can be measured using a luminosity monitor. For CDF during Run 1B, the luminosity was calculated from the measured rates in the BBC. In order to peform the conversion from event rate to luminosity, the $p\bar{p}$ cross section visible to the BBC had to be determined.

### 4.2.1 BBC Cross Section

The BBC cross section, $\sigma_{\mathrm{BBC}}$, was defined as that part of the total $p\bar{p}$ cross section visible to the scintillation counters [89],

$$\sigma_{\mathrm{BBC}} \equiv \sigma_{\mathrm{tot}} \frac{N_{\mathrm{BBC}}^{\mathrm{vis}}}{N_{\mathrm{tot}}}, \tag{4.3}$$

where $N_{\mathrm{BBC}}^{\mathrm{vis}}$ and $N_{\mathrm{tot}}$ are the total number of BBC east-west coincidences[1] and $p\bar{p}$ interactions respectively, and $\sigma_{\mathrm{tot}}$ is the total $p\bar{p}$ cross section. In order to determine $\sigma_{\mathrm{BBC}}$, the total $p\bar{p}$ cross section and the fraction of $p\bar{p}$ events detected by the BBC must be known.

The total $p\bar{p}$ cross section is related to the forward nuclear elastic scattering amplitude through the optical theorem [90, 91]

$$\sigma_{\mathrm{tot}}^2 = \frac{1}{\mathcal{L}} \frac{16\pi}{1+\rho^2} \left.\frac{\mathrm{d}N_{\mathrm{el}}}{\mathrm{d}t}\right|_{t=0}, \tag{4.4}$$

[1] A BBC east-west coincidence was defined as one or more hit scintillators in the east and west detectors within a given time window centered on the beam-beam crossing time.

where $\mathcal{L}$ is the integrated luminosity, $\rho$ is the ratio of the real and imaginary parts of the forward elastic scattering amplitude, and the Mandelstam invariant $t$ is the square of the four-momentum transfered in the collision. In terms of elastic ($N_{\mathrm{el}}$) and inelastic ($N_{\mathrm{inel}}$) event rates, the total cross section can also be written as

$$\sigma_{\mathrm{tot}} = \frac{N_{\mathrm{el}} + N_{\mathrm{inel}}}{\mathcal{L}}. \tag{4.5}$$

Therefore, by dividing Eqs. 4.4 and 4.5, the total $p\bar{p}$ cross section can be written in a luminosity-independent form,

$$\sigma_{\mathrm{tot}} = \frac{16\pi(\hbar c)^2}{1+\rho^2} \left.\frac{\mathrm{d}N_{\mathrm{el}}}{\mathrm{d}t}\right|_{t=0} \frac{1}{N_{\mathrm{el}} + N_{\mathrm{inel}}}. \tag{4.6}$$

Using data from Tevatron Run 1A (1992-3), CDF measured the small-angle elastic [92], single diffractive (inelastic) [93], and total [94] $p\bar{p}$ cross sections. Evaluating Eq. 4.6 required measurements of $\rho$, $N_{\mathrm{inel}}$, $N_{\mathrm{el}}$, and the slope of the elastic scattering amplitude at $t = 0$. The latter two measurements were facilitated by the experimental fact that the nuclear elastic scattering cross section at small $t$ can be approximated as an exponential [90],

$$\frac{\mathrm{d}\sigma}{\mathrm{d}t} = \left.\frac{\mathrm{d}\sigma}{\mathrm{d}t}\right|_{t=0} e^{bt}. \tag{4.7}$$

Thus, a measurement of $\mathrm{d}\sigma/\mathrm{d}t$ as a function of $t$ provides both the slope and intercept needed in Eq. 4.6. The total number of inelastic collisions was obtained by measuring event rates in the BBC and a set of forward/backward telescopes consisting of several planes of drift chambers installed for the special runs devoted to the cross section measurement. Because the combined BBC/telescope system did not record 100% of the inelastic collisions, a Monte Carlo program was used to determine the (small) fraction of missed events. Finally, the parameter $\rho$ is usually measured by observing the behavior of the elastic cross section in the region of maximal interference between the nuclear and Coulomb fields. Due to the small angle ($\sim 0.02\,\mathrm{mrad}$) at which this occurs for $\sqrt{s} = 1.8\,\mathrm{TeV}$, a dedicated experiment was required to perform the measurement [95].

Combining the individual measurements, CDF obtained $\sigma_{\mathrm{tot}} = 80.03 \pm 2.24\,\mathrm{mb}$ for the total $p\bar{p}$ cross section [94]. From the fraction of inelastic events triggered by the BBC (rather than the telescopes), the ratio of visible to total $p\bar{p}$ collisions could be determined. The final result for the BBC cross section was $\sigma_{\mathrm{BBC}} = 51.15 \pm 1.60\,\mathrm{mb}$ [96].

### 4.2.2 CDF Luminosity

Once the BBC cross section was determined, the instantaneous luminosity could be obtained from a measurement of the rate detected by the counters,

$$\mathcal{L}_{\mathrm{BBC}} = \frac{R_{\mathrm{BBC}}}{\sigma_{\mathrm{BBC}}}. \tag{4.8}$$

For an instantaneous luminosity low enough such that the average number of interactions per beam crossing was much less than 1, Eq. 4.8 gave an accurate estimate of the luminosity. However, since the luminosity trigger required only one hit each on the east and west sides, the BBC integrated multiple $p\bar{p}$ interactions in the same beam crossing. When the luminosity increased to the point where the mean number of interactions per crossing was $\sim 1$, the probability of getting two or more interactions in the same crossing was high. Under those conditions, Eq. 4.8 underestimated the luminosity.

Correcting the instantaneous BBC rate for multiple interactions was straight forward [97]. The number of interactions per crossing follows Poisson statistics,

$$P(n) = \frac{\langle n\rangle^n e^{-\langle n\rangle}}{n!}, \tag{4.9}$$

where $P(n)$ is the probability of having $n$ interactions in one beam crossing. The mean number of interactions per crossing, $\langle n\rangle$, is given by

$$\langle n\rangle = \frac{\sigma_{\rm BBC}\mathcal{L}_{\bf true}}{f}, \tag{4.10}$$

where $f$ is the frequency of beam crossings (286 kHz), and $\mathcal{L}_{\bf true}$ is the "true" luminosity. Since $\sigma_{\rm BBC}$ was the BBC cross section for one, and only one, interaction, and $R_{\rm BBC}$ integrated over multiple interactions, $\mathcal{L}_{\rm BBC}$ was not equal to $\mathcal{L}_{\bf true}$ at high luminosity. What was actually measured by the BBC was the probability of obtaining one or more interactions in a single beam crossing,

$$\sum_{n=1}^{\infty} P(n) = 1 - P(0) = \frac{R^{\rm BBC}}{f}. \tag{4.11}$$

Combining Eqs. 4.9, 4.10, and 4.11 gave the proper relation for the luminosity measured by CDF [84],

$$\mathcal{L}_{\rm CDF} = -\frac{\ln(1 - \frac{\sigma_{\rm BBC}\mathcal{L}^{\rm BBC}}{f})}{\frac{\sigma_{\rm BBC}}{f}}, \tag{4.12}$$

where I have made the notational substitution $\mathcal{L}_{\bf true} \to \mathcal{L}_{\rm CDF}$. The integrated luminosity was obtained by replacing rates with numbers of events counted over a given period of time.

The relation between $\mathcal{L}_{\rm BBC}$ and $\mathcal{L}_{\rm CDF}$ is illustrated in Fig. 4.1. The BBC rate began to saturate at $\sim 5 \times 10^{30}\mathrm{cm}^{-2}\mathrm{s}^{-1}$. When the Tevatron luminosity reached

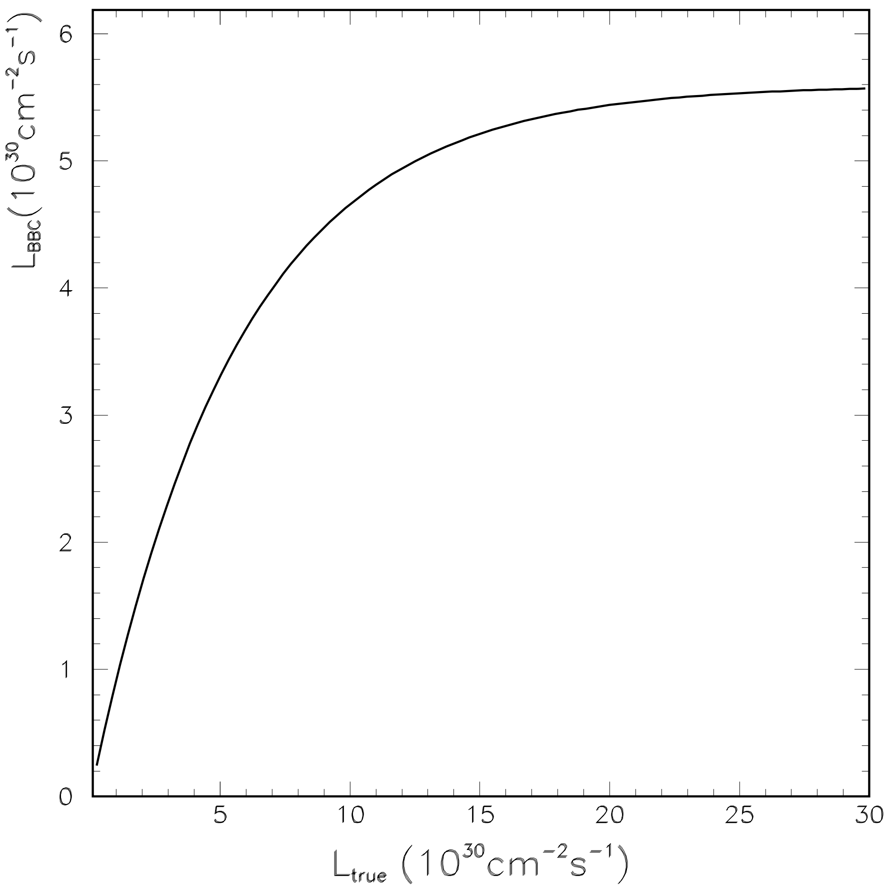


Figure 4.1: Relation between measured ($\mathcal{L}_{\mathrm{BBC}}$) and true luminosity.

that level the BBCs were effectively only counting crossings where no interactions occured. Due to a variety of sources, including beam-gas collisions, cosmic rays, and overlapping single diffractive events, accidental east-west coincidences could occur in the BBC. Because of the high luminosity effect on the BBCs, the accidentals actually became more significant as the luminosity increased. It was therefore necessary to correct Eq. 4.12 for this effect.

The accidentals correction was calculated by considering independently the fraction of beam crossings producing hits in the east BBC ($e$), west BBC ($w$), and both east and west BBCs ($d$). Using probablistic arguments it is easy to show that the true probability, $c$, of obtaining an east-west coincidence is [97]

$$c = \frac{d - ew}{1 + d - e - w}. \tag{4.13}$$

For the reasons given above, this correction to the observed rate was luminosity-dependent during Run 1B. The dependence was found to be linear, and the resulting accidentals correction was determined to be [98]

$$\text{Accidentals Correction}\,(\%) = (0.2704 \pm 0.0063), \tag{4.14}$$

which was applied as a correction to Eq. 4.12 using the average instantaneous luminosity in each data file.

## 4.3 Luminosity for the Prescaled Muon Triggers

While CDF was taking data, dedicated scalers in FRED kept track of the singles rates in the east and west BBCs, as well as the east-west coincidence rate. For each event accepted by the trigger system the current values of the BBC scalers were copied to a data bank in the event record. The integrated luminosity for a given data file was then calculated with Eq. 4.12 using the difference in scaler values for the first and last events in the file. For the majority of datasets, the procedure for obtaining the integrated luminosity was to feed the dataset file list to a program called LUM_CONTROL, which summed up the individual luminosities for each file, applied the accidentals correction, and reported the result.

Due to the high luminosity delivered by the Tevatron during Run 1B, some of the higher cross section triggers had to be prescaled to keep the total level 3 accept rate manageable. Prescaled triggers had their rates reduced by only accepting 1 out of every $p$ triggers, where $p$ was referred to as the prescale factor. Some triggers required *dynamic* prescaling, meaning that $p$ decreased over the course of a data run. For all level 1 and level 2 triggers, a scaler in FRED was assigned to keep track of the number of trigger accepts before and after the prescale factors were applied. In addition to the integrated luminosity per file, LUM_CONTROL had access to these scaler values for the last event in each run, and was therefore able to correct the luminosity for prescaled triggers using the run-averaged prescale factor.

For non-prescaled and statically prescaled triggers, the run-weighted method returned the correct luminosity. However, the run-weighted method underestimated the luminosity for dynamically prescaled triggers by a few percent, depending on the trigger [99]. For these triggers the effect of the prescaling had to be taken into account on a file-by-file basis. Appendix A gives a detailed description of the difference between the file-weighted and run-weighted methods. In the remainder of this section I describe my calculation of the luminosity corresponding to the rate-limited FMU trigger and dynamically prescaled CMUP trigger used in this analysis.

### 4.3.1 Obtaining the Prescale Efficiencies

To calculate prescaled luminosity using the file-weighted method, the number of triggers before and after prescaling for each file was needed. This information was stored in the level 2 trigger scaler bank for the prescaled CMUP_CFT_7_5_5DEG trigger, and in the level 1 trigger scaler bank for the rate-limited FMU_L1_7_5 trigger. The scalers ran continuously throughout a run, so the number of triggers before and after prescaling was the difference in scaler values between the first and last event in a file. However, the event order was usually permuted at level 3 due to multiple events being reconstructed in parallel on the eight separate processor boxes, so every event in a file had to be checked before it was known which were the first and last. Since it was desirable to keep the data permanently on disk, and space was an issue, it was decided to copy the banks from only the first 20 events in a file. This ensured that the first event (or close to it) was copied. The number of triggers per file was then calculated from the difference in scaler values for the first event in consecutive files.

Prescale information was eventually obtained for 15297 out of 15693 files in the master luminosity database. The missing files were either on missing or damaged tapes, empty, or contained bad prescale data. Figure 4.2 shows the average prescale efficiency per file for the CMUP and FMU triggers. Major peaks in the CMUP efficiency correspond to prescale values of 1, 2, 3, 4, 8, and 32, while interpeak data comes from files where the prescale value changed midway through and the efficiency was a weighted average of the two. The FMU prescale efficiency plot reflects the continuously varying nature of the prescale corresponding to a rate-limited trigger, and also graphically demonstrates that the FMU level 1 trigger almost never enjoyed a prescale value of 1.

### 4.3.2 Luminosity Calculation

Given the prescale efficiency for each file, $\epsilon_j$, the luminosity was calculated with the following equation,

$$\mathcal{L} = \sum_j \epsilon_j \mathcal{L}_j^{\mathrm{CDF}} C_j, \qquad (4.15)$$

where $C_j$ is the accidentals correction given by Eq.4.14, and $\mathcal{L}_j^{\mathrm{CDF}}$ is the integrated luminosity for file $j$. The integrated and average instantaneous luminosities (to calculate $C_j$) were obtained from the same master luminosity database file accessed by LUM_CONTROL. Approximately 15% of the files were missing an instantaneous luminosity entry, which means the accidentals correction could not be calculated.

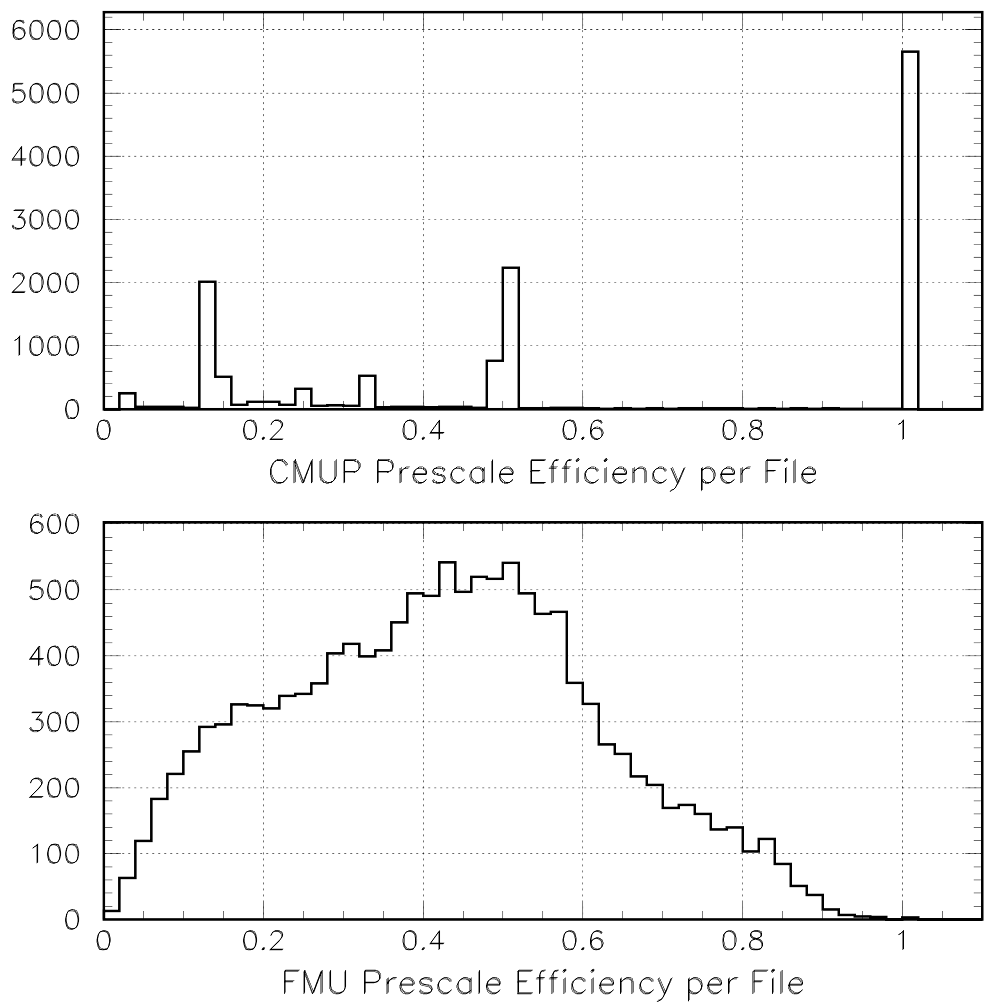


Figure 4.2: Prescale efficiencies for the CMUP (top) and FMU (bottom) triggers.

**Luminosity Summary**

| | |
|---|---|
| Number of files in input list: | 14337 |
| Files with $\mathcal{L}_{\mathrm{CDF}} > 2.0\,\mathrm{nb}^{-1}$: | 13668 |
| Files with prescale info: | 13390 |
| Files in good run list: | 12184 |
| CDF luminosity: | $77.1\,\mathrm{pb}^{-1}$ |
| FMU luminosity: | $30.5\,\mathrm{pb}^{-1}$ |
| CMUP luminosity: | $43.1\,\mathrm{pb}^{-1}$ |

Table 4.1: Summary of the luminosity calculation.

Given that this correction is only 6% at the highest luminosity seen by CDF in Run 1B, using a correction factor of 1.0 for these files would introduce at most a 1% error ($.15 \times .06$) on the total luminosity. However, a more accurate calculation was obtained by filling in missing entries with the following algorithm. For isolated files in a run, the average instantaneous luminosity from the two adjacent files was used. If two or more consecutive files in a run were missing an entry, the average instantaneous luminosity found in the LUMMON[2] output file for that run was used. If the corresponding LUMMON file was not available, a correction factor of 1.0 was used. Only 29 files fell into this last category, introducing a negligible error.

Table 4.1 summarizes the luminosity calculation. The common file list for the three triggers used in this analysis was constructed in the following way. First, the individual file lists used to create the datasets were cross-checked to create a filtered list containing only those files that appeared in each of the three lists.

[2]LUMMON was an online diagnostic program that recorded luminosity and trigger information throughout a data run. LUMMON output was saved to disk as a text file and was easily accessible.

There were 14337 files in the filtered list. Requiring that each file have integrated luminosity $> 2.0\,\mathrm{nb}^{-1}$ left 13668 remaining. Next, files for which no prescale information was available were removed, leaving 13390 files in the list. Finally, files in data runs that were considered "bad for all analyses" for any of a variety of reasons, including bad trigger or calibration data, corrupted data banks, or inoperable detector elements, were removed from the list. The final list contained 12184 files, for which the CDF luminosity was determined to be $77.1\,\mathrm{pb}^{-1}$. The prescaled luminosity for the FMU and CMUP triggers was $30.5\,\mathrm{pb}^{-1}$ and $43.1\,\mathrm{pb}^{-1}$ respectively. The resulting total prescale efficiencies are 39.6% and 55.9% for the forward and central muon datasets.

The CMUP trigger efficiency varied over the course of the run due to detector modifications and changing operating conditions. The prescale efficiency is therefore included in the trigger simulation, which takes into account the changes in trigger efficiency over the course of Run 1B.

# Chapter 5

# Data Reduction

The primary task in this analysis is to positively identify both the $b$ and $\bar{b}$ in the forward and central muon samples. The trigger datasets described in the previous two chapters provide only a high $p_T$ muon in the case of the CMUP trigger, or a high $p_T$ muon plus an uncorrelated jet in the case of the FMU trigger. In both samples, explicit kinematic requirements have only been placed on the $b$-quark decaying to the muon. Furthermore, simply requiring an additional jet does not constitute identification of the second $b$, or provide a means with which to separate signal from background. Further cuts are therefore required to increase the $b$ purity of the trigger samples, and additional techniques are needed to determine the fraction of events in the final sample that are due to $b\bar{b}$ production.

The selection criteria applied in this analysis are designed to detect both the $b$ and $\bar{b}$ by identifying the semileptonic decay of one quark to a muon+jet, and the inclusive decay of the second quark using a secondary vertex tagging algorithm. The muon and $\mu$-jet are collectively referred to as the $\mu$-tag, while the tagged $b$-jet is referred to as the SVX-tag. Events are classified as forward or central depending on whether the muon is FMU or CMUP respectively. I begin this chapter by describing how the primary vertex is reconstructed in three dimensions and the procedure to correct jet energies for detector effects and underlying event background. I then describe the secondary vertexing algorithm used to identify jets likely to contain a heavy quark decay, and close by listing the offline cuts used to define the final datasets.

## 5.1 Primary Vertex Reconstruction

Offline reconstruction of the primary vertex location began with identified track segments in the VTX. Segments were combined to form vertex positions in $z$, and the resulting vertices were ranked according to number of segments, total number of hits, and forward/backward asymmetry. The asymmetry variable compared the number of VTX segments in the forward ($N_f$) and backward ($N_b$) cones defined by $|\theta| < 70°$, requiring good vertices to have $|N_f - N_b|/N < 0.70$, where $N$ was the total number of segments attached to the vertex. Class 12 was the highest quality vertex and required 6 or more VTX segments and $> 180$ total hits. Because the VTX did not provide momentum measurements, the primary vertex was identified as the "best" vertex according to the above criteria, regardless of the $p_T$ distribution of tracks attached to the vertex. An initial estimate of the vertex location in the transverse plane was obtained from the $z$ position and the average Tevatron beam line slope in the $r$–$z$ plane (using SVX tracks) for the data run in which the event was recorded.

Beginning with the seed primary vertex position, an iterative fitting procedure was performed combining the average beam line position with reconstructed SVX tracks [100, 101]. Using the beam line position in the fit reduced the effect of large impact parameter tracks in events containing heavy quark decays. For each iteration, the track with the largest residual with respect to the fitted vertex was discarded if that residual was above a preset value. The algorithm continued until no more tracks were discarded, or until the number of remaining tracks was less than one, since any track combined with the beam line resulted in a more accurate determination of the transverse vertex position. For fitted vertices with only one attached SVX track, the improvement in transverse position resolution was $\approx 40\%$, while the longitudinal position resolution improved by $\approx 17\%$ [101]. Vertices with more than one track had corresponding improvements in resolution.

At high luminosity, more than one $p\bar{p}$ interaction could occur in the same beam crossing (Sec. 4.2.2). As mentioned above, multiple vertices in the same event were sorted according to number of segments and total hits used in the VTX fit. However, this ordering was not always optimal. During Run 1B the proton and antiproton beams did not meet head-on; the slope of the beam line being approximately $6\mu$m/cm in $x$ and $-3\mu$m/cm in $y$ [102]. This slope, combined with the longitudinal extent of each bunch (30 cm), could lead to tracks from one vertex appearing to be displaced with respect to another vertex in the same event. To minimize this effect, before performing the track fit described above, SVX tracks were assigned to the nearest vertex within $|z| < 5$ cm. The vertex with the largest $\sum |\vec{p_T}|$ was then chosen as the primary [103]. In a subset of CMUP trigger events, Fig. 5.1 shows the difference in $z$ between the original primary vertex determined from the VTX fit, and the result of the combined fit starting from the highest $p_T$ vertex. The narrow peak is due to events where the two coincided, while the broad background is due to events where the two are distinct. For this analysis I use the highest $p_T$ VTX vertex as the seed to the fitting algorithm, and I require the resulting primary vertex to satisfy $|z| < 30$ cm. This cut restricts the analysis to those events within the full acceptance of the SVX.

The distribution shown in Fig. 5.1 also has consequences for energy clustering and jet identification, since the initial offline event reconstruction used the VTX primary vertex to cluster events. Because CDF uses tower $E_T$, rather than $E$, to cluster jets, applying the clustering algorithm with respect to the wrong vertex effects not only the $E_T$ of each jet, but can also result in a different set of towers being assigned to each cluster. The resulting shift in the jet axis can affect the calculation of $p_T^{\rm rel}$ used to determine the $b$ fraction on the $\mu$-tag side. Calorimeter energy was therefore reclustered using the result of the combined primary vertex fit.

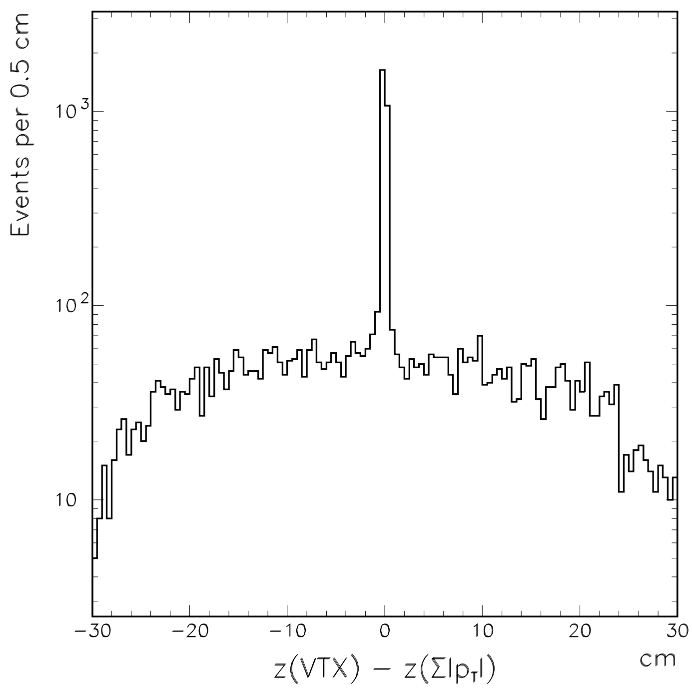


Figure 5.1: Difference in $z$ between the VTX primary vertex and the result of the combined fit using the highest $p_T$ vertex as a seed.

## 5.2 Jet Energy Corrections

The jet energy scale at CDF has been extensively studied and a detailed description of the standard corrections was presented in Ref. [104]. The corrections fall into four general categories: relative, absolute, underlying event, and out-of-cone. All of the corrections were combined into one FORTRAN program, which, for each jet, returned the correction factor $E_T^{\rm cor}/E_T$, where $E_T^{\rm cor}$ is the corrected transverse energy of the jet. In this analysis I apply all but the out-of-cone correction, which was designed to correct for the low momentum particles that are swept out of the jet cone by the magnetic field. Such a correction is more relevant in the top quark mass determination, where soft gluon radiation outside the jet cone contributes the dominant systematic uncertainty on the jet energy scale [105].

Since the central calorimeters had superior energy resolution (Table 3.1), the first procedure in correcting jet energies was to make all jets equivalent to central jets. This relative correction factor [106] was a function of both $E_T$ and $\eta_D$, and was determined with a dijet balancing technique. A sample of dijet events with two, and only two, jets having uncorrected $E_T > 15\,\mathrm{GeV}$ and one jet in the region $0.2 < |\eta_D| < 0.7$ were selected. The central jet was referred to as the "trigger" jet, while the second jet was the "probe" jet. The correction factor, $\beta_R \equiv E_T^{\mathrm{trig}}/E_T^{\mathrm{probe}}$, was parameterized with a spline-fit in $\eta_D$, and linearly in $E_T$. Fig. 5.2 shows the resulting relative correction for a sample of inclusive jets with uncorrected $E_T$ in the range $50 < E_T < 100\,\mathrm{GeV}$. The effects of cracks at calorimeter boundaries are clearly visible at $|\eta_D| = 0$, 1.1, and 2.4, where the correction factor can be as high as 30%.

The relative jet energy correction equalized the $\eta$ response of the CDF calorimeter system relative to the central detector. The goal of the absolute energy correction was to correct for nonlinearities in the central calorimeter response. The correction factor was derived from a Monte Carlo program using ISAJET with a tuned Field-Feynman fragmentation scheme [32], and a full detector simulation. The simulation included the single pion response measured both in test beams and *in situ*. Dijet events were generated and the simulated jets were clustered using the same clustering algorithm applied to data. The correction factor was then defined as the ratio of uncorrected jet $p_T$ to the sum of $p_T$ for all particles whose initial momentum vector was inside the jet cone. The mean response was parameterized as a function of $E_T$, with a typical correction of +15%.

After the absolute energy correction was applied, all jet energies were corrected for the presence of underlying event energy, which arose from the low momentum-transfer collisions between spectator partons in the proton and antiproton. These resulting particles produced an ambient background energy deposition throughout

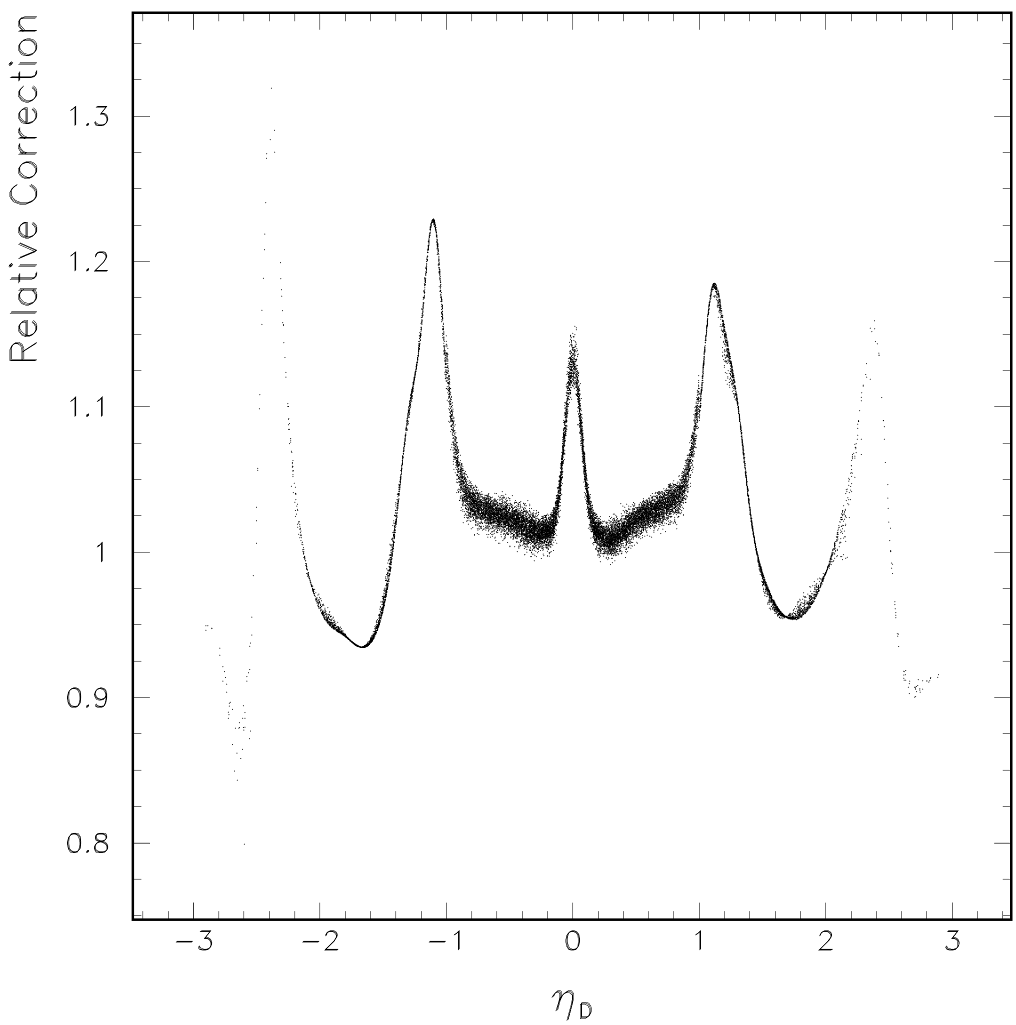


Figure 5.2: The relative jet energy correction with respect to pseudorapidity.

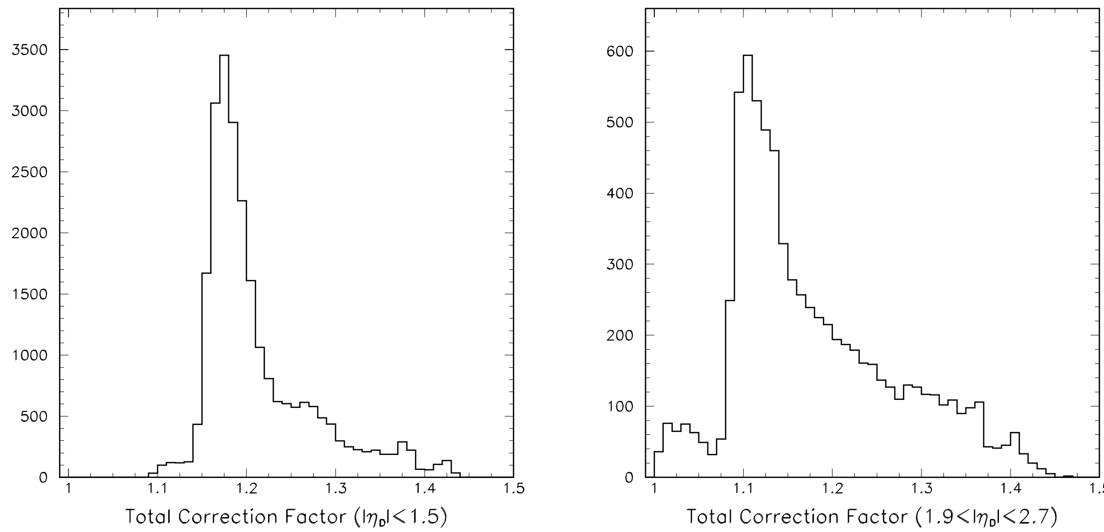


Figure 5.3: The total energy correction for central (left) and forward (right) jets in the FMU trigger sample.

the calorimeter system. The effect of the underlying event was a function of luminosity and the size of the cone used to cluster jets. I used an average correction based on the mean instantaneous luminosity during Run 1B ($9.0 \times 10^{30}\,\mathrm{cm}^{-2}\mathrm{s}^{-1}$), which was 3.29 GeV for a cone size of 0.7.

The total correction factor for jets with uncorrected $E_T > 15\,\mathrm{GeV}$ in the FMU sample is shown in Fig. 5.3. I show the correction for central ($|\eta_D| < 1.5$) and forward ($1.9 < |\eta_D| < 2.7$) jets separately, where the definitions correspond to the cuts described below (Sec. 5.4). The average correction was 20% and 15% for central and forward jets respectively, where the higher correction for central jets was due to the two detector cracks present in that region, compared with only one crack in the forward region (cf. Fig. 5.2). Unless it is specifically stated otherwise, all future references to jet $E_T$ in this thesis will refer to corrected $E_T$.

**SECVTX Track Quality Cuts**

| Cut | Loose | Tight |
|---|---|---|
| $p_T$ | $0.5\,\mathrm{GeV}/c$ | $1.0\,\mathrm{GeV}/c$ |
| $d_0/\sigma_{d_0}$ | 2.5 | 3.0 |
| $N_{\mathrm{good}}^{\mathrm{cluster}}$(3-hit track) | $\geq 1$ | $\geq 2$ |
| $N_{\mathrm{good}}^{\mathrm{cluster}}$(4-hit track) | $\geq 1$ | $\geq 1$ |

Table 5.1: Summary of loose and tight SECVTX track quality cuts.

## 5.3 Secondary Vertex Algorithm

I use a modified version of the secondary vertexing (SECVTX) algorithm originally developed for the CDF top quark analysis [107]. As the name implies, the objective of the SECVTX [108] algorithm is to identify sets of tracks within jets that meet at a point in the transverse plane that is displaced from the primary vertex. The algorithm begins by creating two lists of displaced SVX tracks passing either loose or tight quality cuts. Table 5.1 summarizes these cuts. A "good" SVX cluster is defined as a cluster which is not shared with another track and comprises three or less hit microstrips, which is the expected width of charge deposition from a single track. Different cuts are placed on the number of good clusters required depending on the total number of SVX clusters on the track. Finally, track pairs with invariant mass within $1\sigma$ of the known $K_S$ or $\Lambda$ masses [44] are discarded, and the remaining tracks are assigned to the nearest jet within a cone of radius $R = 0.7$.

Identification of secondary vertices proceeds in two steps. For each jet, associated tracks are ranked according to $p_T$, impact parameter significance ($d_0/\sigma_{d_0}$), and number of good clusters. The first pass (Pass 1) begins with tracks passing the loose cuts defined in Table 5.1. The two highest quality tracks are then re-tracked while constraining them to originate from a common vertex. An attempt is then made to attach the remaining tracks to this seed vertex. If an additional track having an impact parameter significance $< 3$ with respect to the seed vertex is not found, a new track pair is used to form a seed vertex. The algorithm continues until one or more tracks are succesfully attached to a seed vertex, or until all track pairs have been tested. If a secondary vertex candidate is found a full three-dimensional fit is performed simultaneously constraining all attached tracks to originate from a common vertex. If no candidate is found a second pass is performed. The second pass (Pass 2) uses tracks satisfying the tight quality cuts listed in Table 5.1, requiring at least one track to have $p_T > 2\,\mathrm{GeV}/c$. These tracks are fit to a common three-dimensional vertex and if the track contributing the largest $\chi^2$ has $\chi^2 > 50$, that track is discarded and the remaining tracks are refit. This process is repeated until no more tracks are discarded, or there are less than two tracks in the list.

If neither Pass 1 or Pass 2 produces a secondary vertex candidate, the current jet has failed the algorithm and processing moves on to the next jet in the event. If a secondary vertex is found, the jet has been "tagged" and the two-dimensional decay length $L_{xy}$ is defined as

$$L_{xy} = (\vec{S} - \vec{P}) \cdot \hat{j}, \tag{5.1}$$

where $\vec{P}$ and $\vec{S}$ are the position vectors of the primary and secondary vertices in the transverse plane, and $\hat{j}$ is a unit vector pointing along the jet axis. The situation is illustrated in Fig. 5.4 (see also Fig. 3.6). The decay length has a definite sign depending on whether the secondary vertex appears to originate from in front of or behind the primary. If the secondary vertex is on the same (opposite) side of

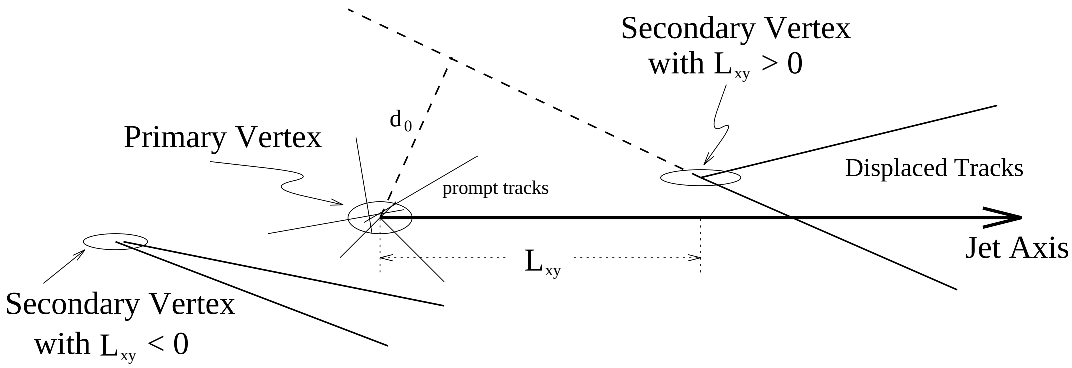


Figure 5.4: An illustration of positive and negative secondary vertices.

the primary as the jet then $L_{xy}$ is positive (negative). Examples of both types of vertex are shown in Fig. 3.6. I accept both positive and negative $L_{xy}$ tags since the latter is useful in determining the "fake" SECVTX tag background, defined as any tagged jet not arising from the decay of a heavy quark ($b$ or $c$). As a final quality cut, the decay length significance $L_{xy}/\sigma$ is required to be $\geq 2.0$, where $\sigma$ includes the uncertainty from both the primary and secondary vertex fits.

## 5.4 Event Selection Criteria

In this section I describe the selection criteria used to increase the $b$ purity of the forward and central muon trigger samples. Wherever possible, kinematic and geometric cuts are set equal in both samples in order to minimize the effect of systematic uncertainties that depend on event topology.

### 5.4.1 Muon-Tag Requirements

The trigger $b$ is identified through its decay to a muon correlated with a jet, constituting what I refer to as the $\mu$-tag. Since events could contain more than one muon, all candidate FMU and CMUP muons are explicitly required to pass their respective triggers. For the forward sample I check that the six drift chamber hits pass one of the 100% NUPU roads (Sec. 3.3.1) and a pad-scintillator match is present in the same octant. For the central sample I check that all of the trigger bits are correctly set in the level 1 and level 2 trigger data banks and rerun the CFT-CMU track matching to ensure that the muon stub could have passed the trigger. I then apply tighter track matching cuts; requiring the CMU and CMP stubs to match within $3\sigma$ in $x$, and the CMU stub to match within $\sqrt{12}\sigma$ in $z$, where $\sigma$ includes the effects of multiple scattering and engery loss. These requirements remove approximately 20% of FMU muons, 15% of stream B CMUP muons, and 50% of stream C muons, where the difference between the two central muon samples was due to the much looser matching requirements applied in the stream C trigger (see Sec. 3.3.1).

The FMU track fit at level 3 was performed without a vertex constraint. In order to increase the momentum resolution I refit all candidate forward muons constraining the $z$ position of the track at closest approach to the beam line to be equal to the event primary vertex. I then require $p_T^\mu > 6\,\mathrm{GeV}/c$ for muons in both the forward and central samples. In addition, the forward muon pseudorapidity is required to be in the range $2.0 < |\eta| < 2.6$ in order to match the coverage of the CMU-CMP system $|\eta| < 0.6$, and the CTC track associated with the CMUP muon must point back to the primary within 5 cm ($5\sigma$) in $z$.

Poorly reconstructed forward muons are rejected by requiring the confidence of the track fit, Prob($\chi^2$), to be greater than 1%. If the FMU hit position resolution is properly understood, the fit quality variable should be distributed according to a $\chi^2$ distribution with 3 degrees of freedom. The corresponding Prob($\chi^2$) distribution should then be flat between 0 and 1. Fig. 5.5 shows the forward muon Prob($\chi^2$) distribution for a subset of muons satisfying all other cuts. It is indeed flat. The large peak at small values of Prob($\chi^2$) is due to both fake muons (*ie*, random hit combinations) and badly measured real muon tracks. The cut on Prob($\chi^2$) > 1% removes the majority fake muons while retaining $\approx 90\%$ of the real muons.

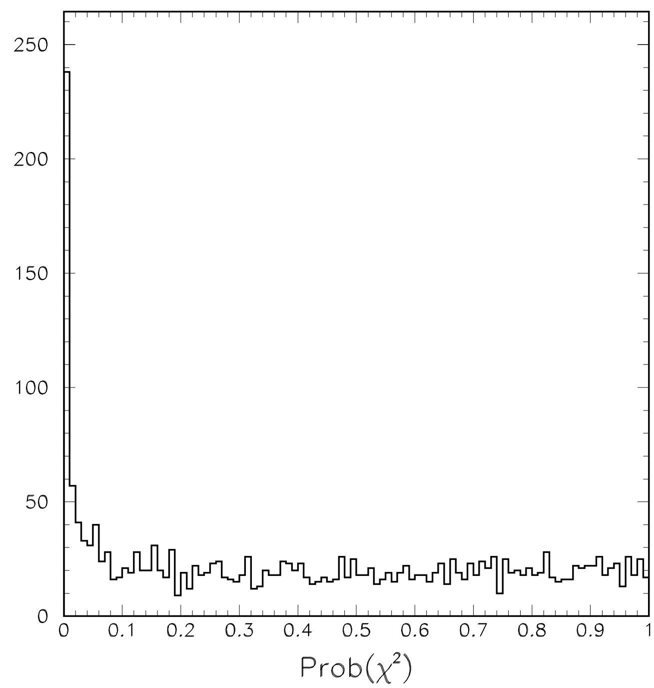


Figure 5.5: The distribution of FMU track-fit confidence level.

Once the muon has been identified, I define the $\mu$-jet to be the jet with the minimum separation in $\eta$–$\phi$ space from the muon. This jet is required to be within $\Delta R < 0.7$ of the muon and have $E_T > 15\,\text{GeV}$. If the closest jet does not satisfy either of these two cuts the event is dropped, even if there is a second jet within $\Delta R < 0.7$. This algorithm guarantees that for events with two jets near the muon, only the closest jet is considered as a candidate. Finally, the $\mu$-jet in the forward sample must be in the range $1.9 < |\eta_D| < 2.7$, while the $\mu$-jet in the central sample must have $|\eta_D| < 0.7$. Table 5.2 summarizes the cuts used to define the $\mu$-tag in both samples. Requiring a $\mu$-tag reduces both samples by a factor of 10.

**Muon-Tag Selection Criteria**

| | Forward | Central |
|---|---|---|
| Muon: | $p_T > 6\,\mathrm{GeV}/c$ | same |
| | $2.0 < \|\eta\| < 2.6$ | $\|\eta\| < 0.6$ |
| | Track Prob$(\chi^2) > 1\%$ | $\Delta z < \sqrt{12}\sigma$, $\Delta x < 3\sigma$ |
| | | $\Delta z < 5.0\,\mathrm{cm}$ |
| $\mu$-Jet: | $\Delta R < 0.7$ | same |
| | $E_t > 15\,\mathrm{GeV}$ | same |
| | $1.9 < \|\eta_D\| < 2.7$ | $\|\eta_D\| < 0.7$ |

Table 5.2: Cuts used to define the $\mu$-tag.

### 5.4.2 SVX-Tag Requirements

In both samples, the second $b$ quark is identified as a SECVTX-tagged central jet, which I refer to as the SVX-tag. For the CMUP sample the SVX-tag must be distinct from the $\mu$-jet. The SVX-tag must have $E_T > 26\,\mathrm{GeV}$ and $|\eta_D| < 1.5$ in both samples. The $E_T$ threshold is driven by the FMU level 3 jet requirement, which, after the reclustering and jet energy corrections, produces a turn-on in the central jet $E_T$ spectrum, Fig. 5.6. The cut was chosen as the point at which the distribution turns over. Since the central muon triggers did not require a jet, this cut could be lower in that sample. However, the SECVTX tagging efficiency falls off dramatically below 25 GeV [109], so in order to facilitate cancellation of the tagging efficiency in the cross section ratio I set the SVX-tag cuts equal in both data samples. The SVX-tag requirement reduces each sample by approximately a factor of 50. The number of events remaining after requiring both a $\mu$-tag and SVX-tag is 391 in the forward sample and 7737 in the central sample.

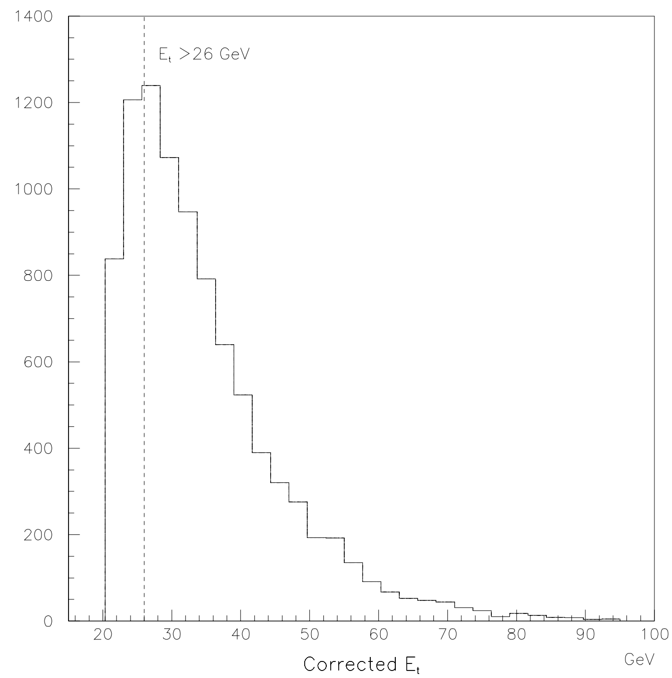


Figure 5.6: The corrected $E_T$ distribution for the central SECVTX-tagged jet in the forward sample.

### 5.4.3 Opening Angle Requirement

There is one final cut applied to both samples. Once the SVX-tag is identified, I require $\delta\phi(\text{tags}) > 60°$, where $\delta\phi$ is the azimuthal opening angle between the $b$-jet axis and the vector sum of the muon and $\mu$-jet momenta. This cut is motivated by the decreasing acceptance observed in the central data sample for small values of $\delta\phi$, where the $\mu$-jet and $b$-jet occupy overlapping regions of phase space, compared with the increase in this region due to the gluon splitting process predicted by the NLO QCD calculation of Mangano, Nason, and Ridolfi (MNR) [19], Fig. 5.7. In contrast, no such increase is predicted in the forward sample, where the $b$ and $\bar{b}$ are separated by a minimum opening angle in $\eta$-$\phi$ space and the gluon splitting process is highly suppressed. The presence of this process in the central sample will

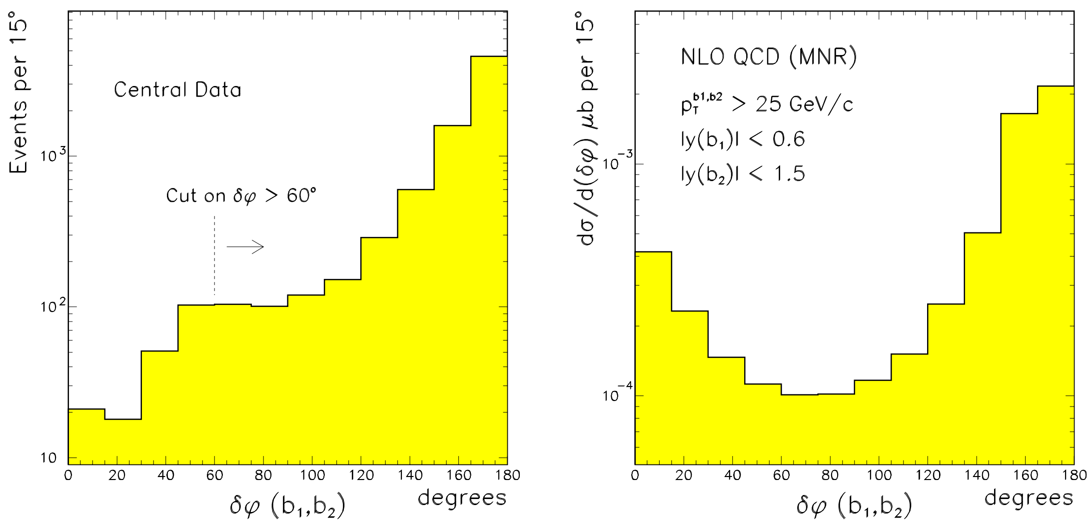


Figure 5.7: The azimuthal opening angle between the $\mu$-tag and SVX-tag in central data events (left), and the NLO QCD prediction (right) using the cross section definition in Table 1.1.

therefore introduce a model dependence in the acceptance calculation that does not cancel in the cross section ratio. By requiring $\delta\phi(\text{tags}) > 60°$ the contribution from gluon splitting in the region of falling acceptance is removed, which allows me to ignore this process in the acceptance calculation. There are 382 (7544) forward (central) events remaining after the $\delta\phi$ cut.

# Chapter 6

# Selection Criteria Efficiency

In order to determine the total number of $b\bar{b}$ events corresponding to the cross section defintion in Chapter 1, the event yields in each data sample need to be corrected by the efficiency of satisfying the selection criteria. Since I am quoting quark-level cross sections, it will be necessary to use a Monte Carlo simulation to determine the kinematic efficiency for a $b$ quark to produce, for example, a 6 GeV/$c$ muon satisfying the muon cuts. For the purpose of keeping clear which efficiencies are measured in data and which are from simulation, I have chosen to separate the total efficiency calculation into two parts by defining the "acceptance" to be the Monte Carlo evaluated efficiencies for all cuts that could not be determined in data, and the "efficiency" to be those cuts that were determined in data. The only exception to this definition is that the central muon level 1 and level 2 trigger efficiencies, although measured in real data, are included in the trigger simulation. In addition, the prescale efficiencies calculated in Chapter 4 are also included in the acceptance calculation.

The Monte Carlo simulation used to calculate the acceptance includes all of the cuts in one program and the result is quoted as a single number, which is the number of simulated events passing all cuts divided by the number of generated events satisfying the cross section cuts. The individual efficiencies determined in data are estimated separately using appropriately unbiased samples. The results are then combined with the acceptance for an estimate of the total efficiency to detect a $b\bar{b}$ event satisfying the forward or central topology.

## 6.1 Efficiency

The efficiency for each sample is the product of the individual efficiencies for cuts not included in the simulation (Sec. 6.2). For the forward data this includes the level 1 detector efficiency, the level 3 occupancy and jet requirement efficiencies, and the FMU track fit confidence level cut efficiency. The efficiencies not included in the central acceptance calculation are the stub-finding efficiency, muon-track matching efficiency, level 3 $p_T$ cut efficiency with respect to offline, and the offline tracking efficiency. In this section I describe the measurement of each of these efficiencies.

### 6.1.1 FMU Efficiency

#### Level 1

The level 1 detector efficiency includes the drift chamber, cathode pad, scintillator, and trigger hardware efficiencies. The efficiency was determined as part of the forward muon $W$-asymmetry measurement [110, 111] using a sample of $Z^0 \to \mu^+\mu^-$ decays where one muon was CMU and the other was FMU. The CMU trigger was required so that the sample would be unbiased with respect to the FMU level 1 trigger. Fig. 6.1 shows the invariant mass distribution for the CMU-FMU pairs satisfying basic quality cuts [110]. The fraction of events where both muons have the same sign is 3.5%, indicating a small background contamination from uncorrelated muons.

FMU candidates in the sample with opposite sign muons were checked to see if they should have fired the trigger, and whether or not they actually did. The efficiency was found to be 73(70)% in the West(East) side detectors respectively. The results were consistent within the statistical uncertainty so I combine them to determine an overall efficiency of $(71.4 \pm 1.6)\%$.

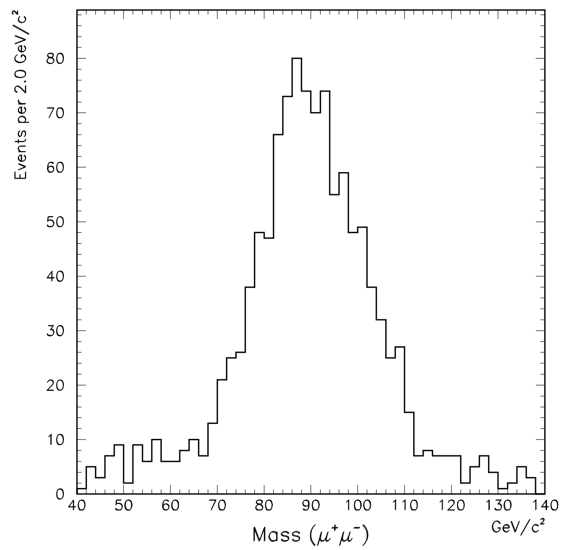


Figure 6.1: Invariant mass distribution for muons in the CMU-FMU $Z^0$ sample.

**Level 3**

The level 3 occupancy cut required $\leq 30$ hits in the octant containing the reconstructed track. I measured the efficiency of this cut with a sample of volunteers which passed the level 1 trigger but were rejected by the rate limit. The events were obtained from the inclusive central muon data streams. I found 3007 events passing the following cuts:

- Level 1 hardware trigger bit present (in FRED)
- Level 1 trigger bit absent in TAGC
- $p_T^\mu > 6\,\mathrm{GeV}/c$
- $2.0 < |\eta^\mu| < 2.6$
- Track Prob($\chi^2$) $> 1\%$
- $|z| < 30\,\mathrm{cm}$

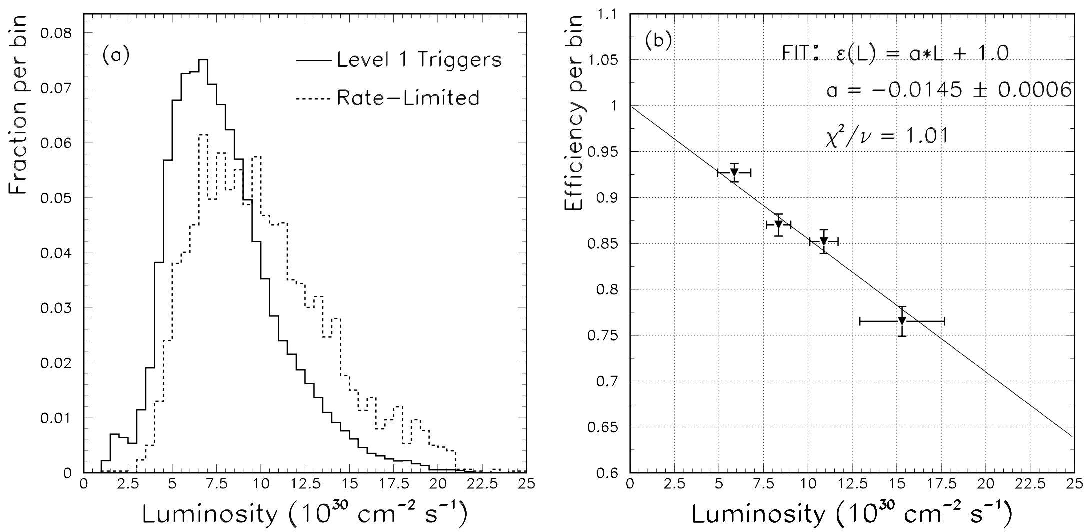


Figure 6.2: (a) Luminosity profile for level 1 FMU triggers (solid), and the sample of rate-limited events used in the efficiency calculation (dashed). (b) The FMU level 3 occupancy cut efficiency as a function of luminosity.

The first two cuts require that the trigger fired but FRED ignored it. The remaining cuts were applied to ensure a sample of quality muons. The number of events in this sample that passed the occupancy cut was 2567, giving an efficiency of $(85.4 \pm .6)\%$.

Since this is an occupancy cut I expect it to be luminosity dependent. Furthermore, the sample of events rejected by the rate limit should have a very different luminosity profile than the triggered data. In Fig. 6.2a I show the luminosity for a volunteer sample of FMU level 1 triggers (solid), and the sample of rate-limited data used to calculate the occupancy cut efficiency (dashed). Since the rate-limited data is skewed to higher luminosity, the average efficiency quoted above is a pessimistic estimate of the true efficiency for the triggered data.

To get the correct efficiency a parameterization as a function of luminosity was needed that could then be applied to the correct luminosity distribution. In

Fig. 6.2b I show the occupancy cut efficiency divided into four bins of instantaneous luminosity. Data points are plotted at the mean of each bin and the horizontal error bar corresponds to the luminosity variance in that bin. Fitting the data to a slope constrained to go through $\epsilon = 1.0$ at $\mathcal{L} = 0.0$, I find $\epsilon(\mathcal{L}) = -0.0145\,\mathcal{L} + 1.0$. Applying this parameterization bin-by-bin to the solid histogram in Fig 6.2a, I obtain an occupancy cut efficiency of $(88.5 \pm 0.4)\%$. Finally, fluctuating the slope by $\pm\sigma$ results in a change of .6%, giving a final efficiency of $(88.5 \pm 0.4 \pm 0.5)\%$.

The jet requirement would be fully efficient if not for the fact that level 3 transverse energy was calculated with $z = 0$. Depending on the actual location of the vertex, a jet with $E_t > 20\,\mathrm{GeV}$ could appear to have $E_t < 20\,\mathrm{GeV}$ and therefore fail the trigger. This effect is reduced by requiring the central jet have corrected $E_t > 26\,\mathrm{GeV}$, but it is still possible for such a jet to fail the trigger. To calculate the efficiency of the jet requirement I took events which passed the inclusive FMU trigger, MUOB_FMU_15 and contained a central jet with corrected $E_t > 26\,\mathrm{GeV}$, and asked how often the FMU_JET trigger was also satisfied. The muon cuts in the inclusive trigger were identical to those in the jet trigger except for a higher $p_T$ threshold ($15\,\mathrm{GeV}/c$). There were 2260 inclusive triggers with a central jet above threshold, 2228 of which also pass the FMU_JET trigger, resulting in an efficiency of $(98.6 \pm 0.3)\%$.

### Prob($\chi^2$) Cut

The efficiency of the Prob($\chi^2$) cut was obtained from the same CMU-FMU $Z^0$ sample used to determine the FMU level 1 trigger efficiency. The number of events in this sample is 1148 and the number passing the cut is 1051, giving an efficiency of $0.920 \pm 0.010$. This result is consistent with the efficiency determined from a detailed Monte Carlo simulation of the FMU detector, as well as the efficiency measured directly in the FMU data sample defeined in the previous chapter.

### 6.1.2 CMUP Efficiency

All of the central muon efficiencies have been measured and documented previously in the course of separate CDF analyses. Here I only give brief descriptions of each of the measurements and refer the interested reader to the internal CDF documentation.

In general, the procedure for determining central muon trigger efficiencies is to obtain a sample of $Z^0$ or $J/\psi \to \mu^+\mu^-$ events that were collected with an independent trigger. High quality cuts, including passing the single muon trigger requirement, are placed on one "leg" of the muon pair. The efficiency of the second muon passing the trigger can then be measured as a function of muon $p_T$. Studies have been performed for the level 1 low $p_T$ CMUP and level 2 CFT bin 0 ($2.2\,\mathrm{GeV}/c$) triggers [112], and the CFT bin 4 ($7.5\,\mathrm{GeV}/c$) and bin 5 ($12\,\mathrm{GeV}/c$) efficiencies were measured with respect to the bin 0 trigger [113]. The trigger efficiency is typically parameterized as a function of $p_T$, or $1/p_T$, and fit to the form:

$$\epsilon(p_T) = \epsilon_0\,\mathrm{freq}\left(\frac{p_T - p_0}{\sigma}\right), \tag{6.1}$$

where freq is the frequency function, $\epsilon_0$ is the plateau efficiency, $p_0$ is the 50% point, and $\sigma$ parameterizes the steepness of the efficiency turn-on.

The combined efficiency for the stub-finding and track-stub matching cuts was determined to be $(96.6 \pm 0.4)\%$ using $J/\psi$ events [114]. The efficiency of passing the level 3 $6\,\mathrm{GeV}/c$ $p_T$ cut relative to the offline $p_T$ cut was not 100% because a slightly different tracking algorithm was used. The efficiency was determined in a similar sample of $J/\psi$ events $(98.5 \pm 1.0)\%$ [115]. Finally, the offline tracking efficiency for high $p_T$ tracks was measured for low, medium, and high luminosity samples by embedding Monte Carlo tracks into real data events and attempting to reconstruct them [116, 117]. The CTC hit efficiency and track finding efficiencies depend on both instantaneous luminosity (hit density) and integrated luminosity (CTC aging). I take a luminosity-weighted average of the efficiencies determined in the three luminosity samples as the best estimate for my analysis. This results in an efficiency of $0.962 \pm 0.009$.

## 6.2 Acceptance

### 6.2.1 Simulation

Monte Carlo $b\bar{b}$ events are generated with the TWOJET process in ISAJET [23], using MRSA$'$ parton densities [51] and a $b$ quark mass of $4.75\,\mathrm{GeV}/c^2$. ISAJET uses the exact leading order matrix elements (Sec. 2.1.2) to generate hard scattering events over user-specified $p_T$ and rapidity ranges. Generated partons are then allowed to radiate as part of a QCD evolution phase governed by the leading-log approximation. The final phase involves hadronizing all final-state partons into hadrons using Field-Feynman fragmentation for light quarks ($u$,$d$,$s$) and Peterson fragmenation (see Sec. 2.3) for $b$ and $c$ quarks. Gluons are fragmented as a randomly selected light quark. For this analysis I use the conventional value of the Peterson fragmentation parameter, $\epsilon_p = 0.006$ [55, 56].

The CLEO Monte Carlo program [118] is used to decay $b$ hadrons with the world average [119] branching fractions. In order to speed up generation of events that will eventually contain a final-state muon, I modified the default code to re-decay events until one, or both, of the $b$ hadrons produces a muon at some stage in its decay chain. The branching fraction that exactly cancels in the cross section ratio is the fraction of all $b\bar{b}$ events that contain a muon, $\mathrm{Br}(b\bar{b} \to \mu X)$, which I find to be 36%. This method of treating the $b$ hadron decays provides a muon for every generated event and conveniently references the acceptance calculation to a common branching fraction between the forward and central samples.

Generated events are simulated with the fast CDF detector simulation program QFL$'$, which performs calorimetry, tracking, and central muon simulation. CTC simulation and tracking require significant processing time, so QFL uses a simplified CTC geometry and tracking package to speed up event simulation. One consequence of this choice is that the CTC track finding efficiency in QFL is $\approx 100\%$, so the true efficiency must be measured independently in the data. However, QFL does include a detailed simulation of the SVX [120], and the resulting CTC-SVX track linking efficiency is well-modeled.

In order to simulate the effect of the broad bunch length on the geometric acceptance, the event $z$ vertex position is chosen randomly from a gaussian distribution with $\bar{z} = 0$ and $\sigma_z = 29\,\text{cm}$. I determined these numbers by fitting the minimum bias vertex distribution to a gaussian over the interval $|z| < 30\,\text{cm}$, Fig. 6.3. Because the $z$ vertex cut efficiency cancels identically in the cross section ratio I only generate events with $|z| < 30\,\text{cm}$.

Forward muons are simulated with FMUSIM, a fast simulation module which includes the effects of multiple scattering, energy loss, and extra hits from delta rays and muon bremsstrahlung distributed around the muon trajectory according to the results of a detailed GEANT simulation [121]. Once the muon drift chamber hits have been simulated, track reconstruction proceeds as in the data. Reconstructed tracks are required to satisfy the same NUPU 100% trigger road as required in the level 1 trigger, while pad and scintillator hits are not simulated because they do not affect the kinematic acceptance for identifying forward muons. They are, however, included in the detector efficiency measurement (Sec. 6.1.1).

Central muons produce simulated hits in the CTC, CMU, and CMP detectors and are reconstructed as in the data. The simulation assumes 100% muon detector efficiency because the level 1 and level 2 trigger efficiencies have been measured in the data and parameterized as a function of muon $p_T$ (see Sec. 6.1.2). A dedicated

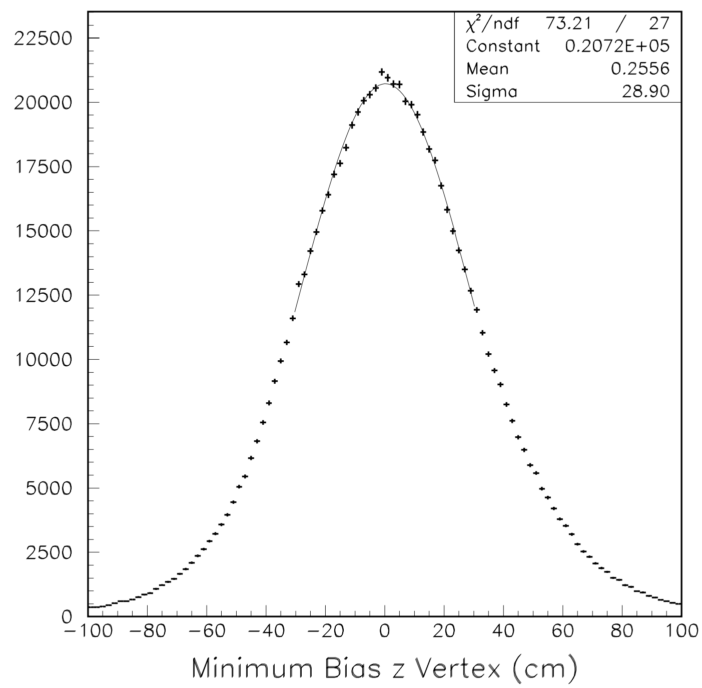


Figure 6.3: The $z$ vertex distribution from Run 1B minimum bias data.

central muon trigger simulation, DIMUTG [122, 123], applies the trigger curves to all simulated muons to account for the kinematic trigger efficiency. In addition, the track-stub matching is simulated and the same matching cuts are required. This program was originally designed for a dimuon analysis and only includes the low $p_T$ level 1 trigger curve. I therefore add by hand the probability of passing the level 1 high $p_T$ trigger given that the low $p_T$ trigger is satisfied ($0.987 \pm 0.022$) [124].

Due to varying run conditions and detector modifications the central muon trigger efficiencies varied over the course of Run 1B [125, 126, 127, 112]. To take this variation into account, DIMUTG divides the data-taking period into thirteen run ranges, where each range has a luminosity weight equal to the integrated CDF luminosity for the data runs in that range. For each simulated event, DIMUTG randomly chooses a run range based on the luminosity weighting and applies the

**CMUP DIMUTG Prescale Efficiencies**

| DIMUTG Run Range | CDF $\mathcal{L}\,(\,\mathrm{pb}^{-1})$ | Efficiency |
|---|---|---|
| 55273 - 56593 | 0.20 | 1.000 |
| 56594 - 58323 | 1.36 | 1.000 |
| 58324 - 60881 | 5.72 | 1.000 |
| 60882 - 62000 | 7.21 | 0.668 |
| 62001 - 63500 | 2.62 | 0.847 |
| 63501 - 64500 | 8.96 | 0.566 |
| 64501 - 65500 | 7.06 | 0.617 |
| 65501 - 67000 | 11.4 | 0.448 |
| 67001 - 67413 | 0.58 | 0.573 |
| 67414 - 68000 | 6.13 | 0.525 |
| 68001 - 69094 | 12.8 | 0.308 |
| 69095 - 70150 | 9.95 | 0.496 |
| 70151 - 71023 | 3.18 | 0.558 |

Table 6.1: CDF luminosity and CMUP prescale efficiency in DIMUTG.

corresponding trigger efficiency parameterizations from the chosen run. It was therefore necessary for me to include the CMUP level 2 prescale efficiencies measured in Sec. 4.3.1 since they modify the relative weight of each run range. The CDF integrated luminosity and CMUP prescale efficiency for each of the run ranges identified by DIMUTG are listed in Table 6.1.

Simulated events are treated in the same manner as real data. The primary vertex is found with the procedure described in Sec. 5.1, although the choice of vertex is unambigous since I do not simulate multiple interactions. Also, no jet reclustering is necessary. The SECVTX tagging algorithm (Sec. 5.3) is run on all jets, and all of the offline cuts outlined in Sec. 5.4 are applied, with the exception of those that are explicitly measured in the data (Sec. 6.1).

### 6.2.2 Acceptance

In this analysis I am measuring parton level cross sections which are to be compared with NLO QCD. The acceptance calculation must therefore correct the data back to the parton level. However, the correspondence between the fixed-order theory calculation and a fully exclusive event generator is not exact. This is because event generators factorize the production process into a hard scattering calculated at leading order, a phenomenological QCD evolution phase, and a fragmentation scheme to hadronize the partons. A problem arises when the analysis cuts conspire to give a different acceptance for each of the simulated production processes (direct, flavor excitation, and gluon splitting)[1], because the generator is not expected to give the "correct" relative normalization. This introduces a possible systematic bias that I would like to avoid. Fortunately, I find that the acceptance is the same for direct and flavor excitation production, and the gluon splitting process is excluded by the $\delta\phi(b\bar{b}) > 60°$ cut described in Sec. 5.4.3. I am therefore free to define the acceptance with respect to the direct production process only.

#### Direct Production

The direct production process is generated in ISAJET by requiring that the outgoing partons in the hard scattering are a $b\bar{b}$ pair. This process corresponds to leading order production plus radiative corrections involving real emission diagrams. The generation cuts are $p_T^b > 15\,\mathrm{GeV}/c$ for both quarks,$|y^b| < 1.65$ for central quarks, and $1.65 < |y^b| < 3.0$ for the forward quark. These cuts are designed to minimize any bias by extending into the regions of zero acceptance. The acceptance is then defined as the number of events passing all cuts, divided by the number

[1]These processes are defined in Sec. 2.1.

of generated events passing the cuts used to define the cross sections (Table 1.1). I determine these cuts based on the offline fiducial requirements placed on the muons and jets. First, the $b$ quark rapidity cut is defined to be equal to the muon $\eta$ cut for the $b$ quark producing the $\mu$-tag, and equal to the SVX-tag $\eta_D$ cut for the second quark. The $p_T^{\rm min}$ cut is then defined in the usual way by requiring that 90% of events satisfying all cuts come from $b\bar{b}$ events where both quarks have $p_T > p_T^{\rm min}$. The same $p_T^{\rm min}$ value of $25\,{\rm GeV}/c$ is obtained for both the forward and central Monte Carlo samples.

Since the stated intention is to use ISAJET direct production to define the acceptance, I must first verify that the shapes of the relevant kinematic variables agree with the MNR prediction. If they do not, the comparison with theory will not be consistent. In Fig. 6.4 I show distributions of $p_T^b$ and $\eta^b$ for ISAJET compared to MNR forward production. Fig. 6.5 shows the same comparison for central production. There is excellent agreement in all variables, giving confidence that the acceptance calculation is a faithful estimate of the fraction of $b\bar{b}$ events that pass the analysis cuts in both samples.

I generated 3.6 (9.5) million central (forward) events to obtain 7008 (6995) events after all cuts. Fig. 6.6 shows the generated and surviving events for the $b$ quark producing the muon in the forward and central samples. The solid histogram is the generated $b$ quark spectrum while the dashed histogram are the subset of events that survive all cuts. The $p_T^{\rm min}$ point is indicated by the arrow. These plots illustrate the much steeper $p_T$ spectrum in forward $b\bar{b}$ events due to the falling gluon distribution in the proton at large $x$ (Sec. 2.2).

The acceptance is calculated as the number of events satisfying all cuts divided by the number of generated events satisfying the cross section cuts. The resulting acceptance for the central topology is $(2.539 \pm 0.064) \times 10^{-2}$, while the forward topology has an acceptance of $(7.734 \pm 0.091) \times 10^{-3}$, which includes the FMU

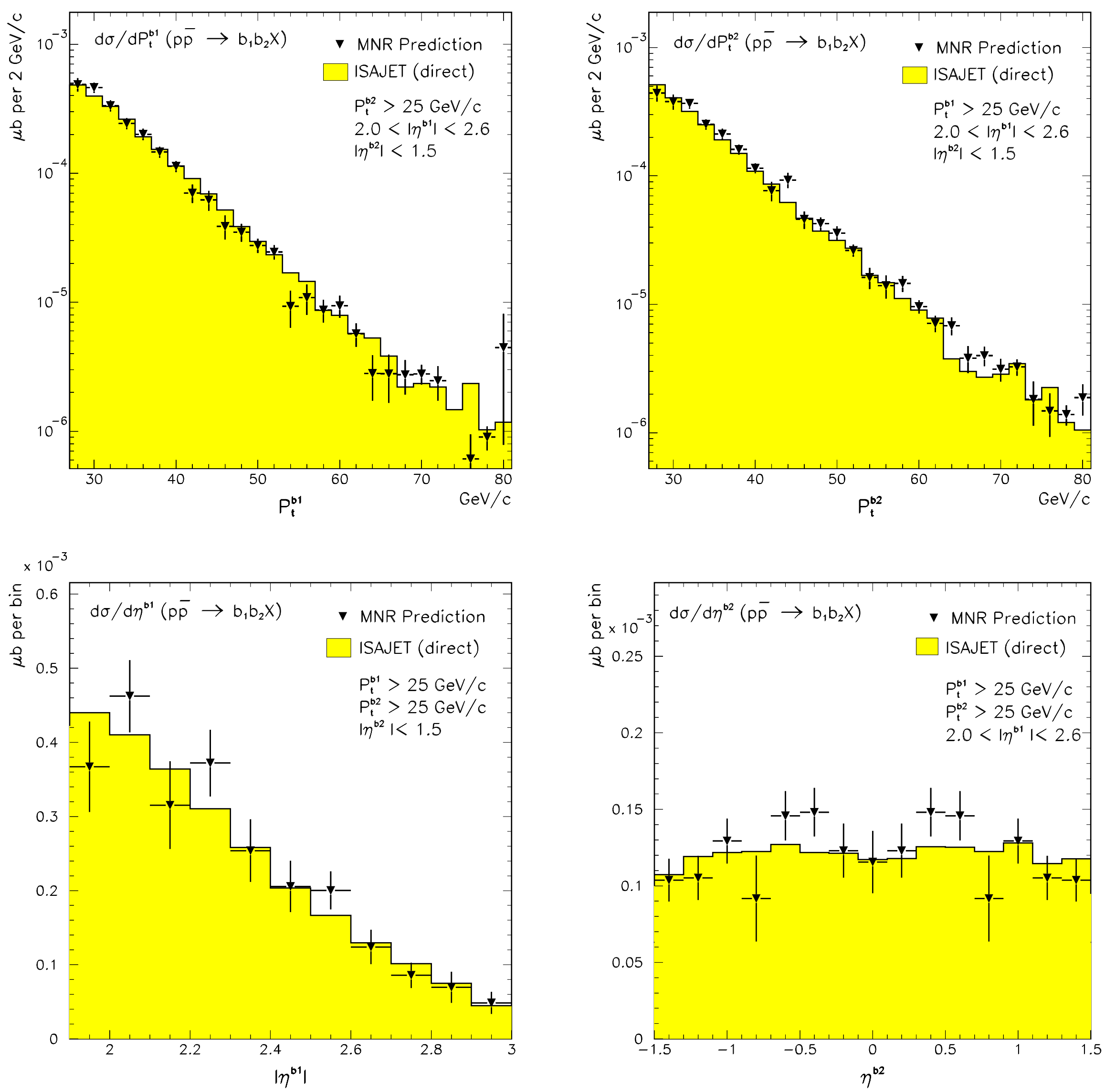


Figure 6.4: Comparison of ISAJET (hist) and MNR (points) $p_T^b$ and $\eta^b$ distributions in forward events.

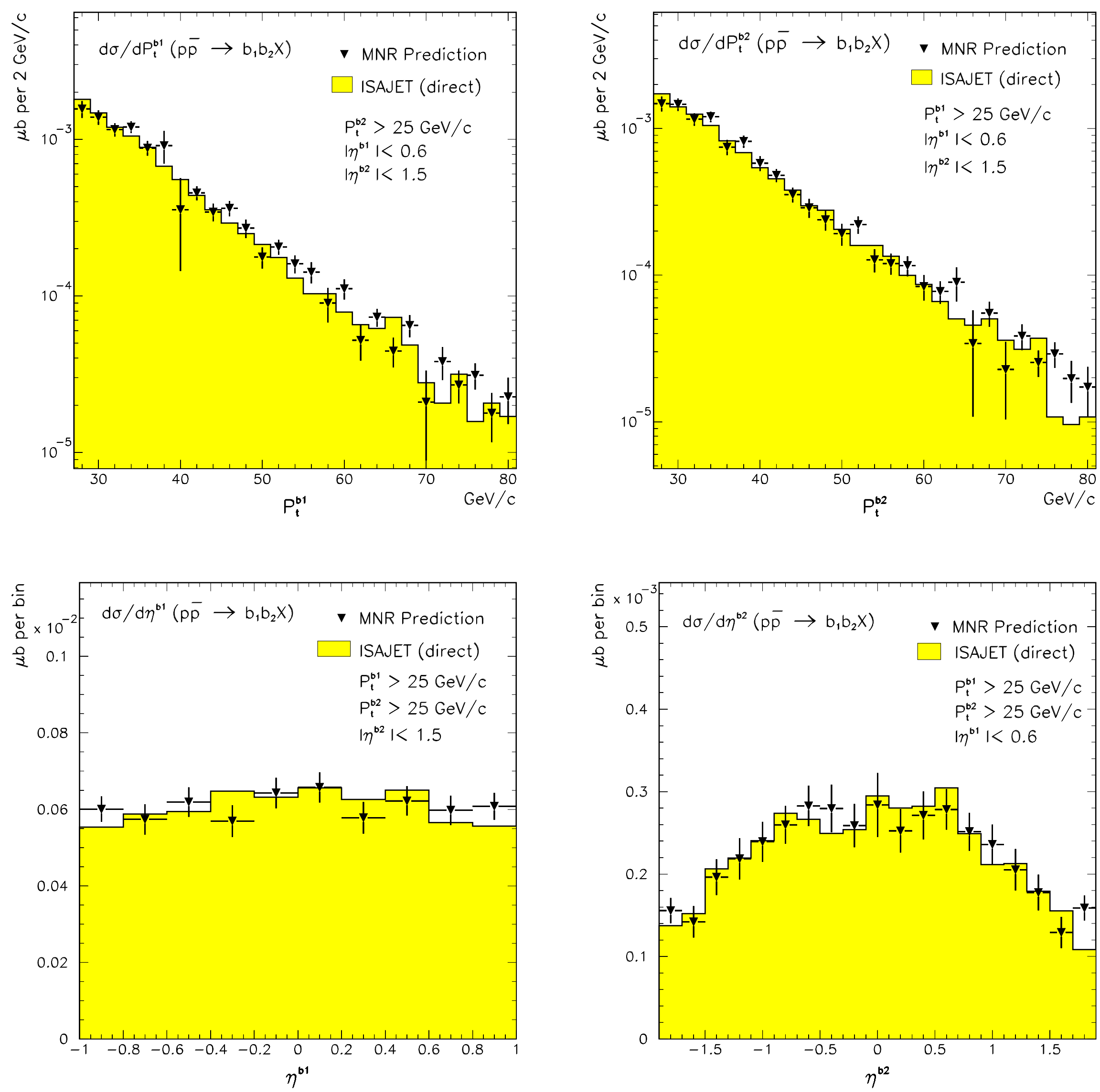


Figure 6.5: Comparison of ISAJET (hist) and MNR (points) $p_T^b$ and $\eta^b$ distributions in central events.

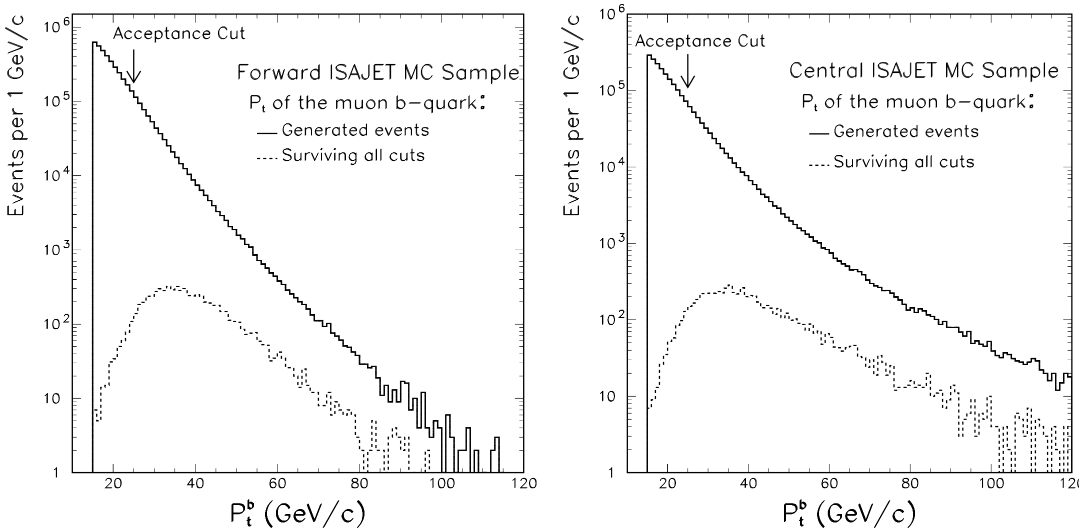


Figure 6.6: Transverse momentum distributions for the $b$ quark decaying to a muon in the forward (left) and central (right) Monte Carlo samples.

prescale efficiency (39.6%) calculated in Chapter 4. The large difference in acceptance is almost entirely due to the combined effects of the steeper $p_T$ spectrum in the forward data and the lower kinematic acceptance of the toroids with respect to the central detector.

**Flavor Excitation**

I have also run ISAJET flavor excitation events. This process is generated by requiring that one of the outgoing partons from the hard scattering is a $b$ (or $\bar{b}$) while the second is a gluon or light quark. Events were generated with $p_T^b > 15\,\mathrm{GeV}/c$ and $p_T^g > 5\,\mathrm{GeV}/c$, where the latter refers to the cut on the light parton. It is not possible to place cuts on the second $b$ quark. In a forward-central topology, the $b$ quark from the hard scattering is almost always the central quark, while its partner from the gluon splitting vertex is usually produced at small angles (large rapidity). I therefore generated events with the hard scattering $b$ quark in the rapidity interval $|y| < 1.65$, while no cut was placed on the light parton. The same cuts were used for the central sample. The resulting samples contain about 3000 events satisfying all cuts. The acceptance is found to be $(2.66 \pm 0.17) \times 10^{-2}$ in the central sample, and $(8.16 \pm 0.63) \times 10^{-3}$ in the forward sample. Both results are consistent with the corresponding acceptances for direct production quoted above.

## 6.3 Total Efficiency

The total efficiency to detect either the forward or central topologies defined in this thesis is calculated as the product of the acceptance and efficiency. Table 6.2 summarizes the efficiency calculation for the forward sample. I find the total efficiency to detect a forward-central $b\bar{b}$ pair passing my cuts to be $(4.43 \pm 0.12) \times 10^{-3}$. Table 6.3 summarizes the efficiency calculation for the central sample, where I find a total efficiency of $(2.32 \pm 0.07) \times 10^{-2}$.

**Forward Efficiency**

| Cut | Efficiency |
|---|---|
| Acceptance | $(7.734 \pm 0.091) \times 10^{-3}$ |
| Level 1 | $0.714 \pm 0.016$ |
| Level 3 occupancy | $0.885 \pm 0.004$ |
| Level 3 jet | $0.986 \pm 0.003$ |
| Prob($\chi^2$) | $0.920 \pm 0.010$ |
| Total efficiency ($\epsilon_{\mathrm{f}}$) | $(4.43 \pm 0.12) \times 10^{-3}$ |

Table 6.2: Summary of the total efficiency for the forward sample. Errors are statistical only.

**Central Efficiency**

| Cut | Efficiency |
|---|---|
| Acceptance | $(2.539 \pm 0.064) \times 10^{-2}$ |
| Stub/Matching | $0.966 \pm 0.004$ |
| Level 3 | $0.985 \pm 0.010$ |
| Tracking | $0.962 \pm 0.009$ |
| Total efficiency ($\epsilon_{\mathrm{c}}$) | $(2.32 \pm 0.07) \times 10^{-2}$ |

Table 6.3: Summary of the total efficiency for the central sample. Errors are statistical only.

# Chapter 7

# Signal Determination and Results

Having determined both the luminosity (Chapter 4) and total efficiency (Chapter 6) corresponding to the datasets defined in Chapter 5, a glance back at Eq. 1.2 reveals that in order to complete the cross section measurement, only a determination of the signal content remains. In this chapter I describe the fitting procedure used to extract the signal content, the cross section results, and comparison with theory.

## 7.1 Fitting Procedure

Although it is a powerful tool for increasing the $b$ fraction in the data, the SECVTX tag requirement does not guarantee that both the $\mu$-tag and SVX-tag are descendant from a $b$ quark decay. There are several physics processes besides $b\bar{b}$ production that contribute to the final data samples. These include $c\bar{c}$ production, heavy quark production in association with a high $p_T$ gluon or light quark jet that fakes a $\mu$-tag or SVX-tag, generic dijet events producing two fake tags, and $Z^0 \to b\bar{b}$ decay. The $b\bar{b}c\bar{c}$ process has been calculated to leading order [128] and is estimated to be negligible. The fraction of events in each sample consisting of two real $b$ tags is determined by simultaneously fitting the $p_T$ of the muon relative to the $\mu$-jet direction, and the transverse proper decay length of the $b$-jet. The number of $b\bar{b}$ events due to $Z^0$ decay is then estimated using the CDF measured cross section and a Monte Carlo acceptance calculation. Finally, several consistency checks on the fit results are presented.

### 7.1.1 Templates

**Pseudo-$c\tau$**

The transverse proper decay length of the secondary vertex is estimated with the following equation,

$$\text{pseudo}-c\tau = L_{xy}\frac{M}{p_T}, \tag{7.1}$$

where the transverse decay length $L_{xy}$ was defined in Sec. 5.3, and the mass $M$ and $p_T$ of the secondary vertex are calculated with the assumption that all tracks in the tag are pions. The term "pseudo" reflects the fact that the $b$ hadron is not fully reconstructed, and therefore, Eq. 7.1 is only approximate. For notational convenience, in the remainder of this thesis I will use $c\tau$ and pseudo-$c\tau$ interchangeably, with the understanding that I refer always to the latter definition.

Fig. 7.1 shows the pseudo-$c\tau$ distributions for bottom, charm, and fake SVX-tags, where "fake" refers to all tagged jets which do not contain a heavy quark. I obtain the shape of the $b$ quark distribution from the Monte Carlo samples used in the acceptance calculation (Sec. 6.2), while a similar Monte Carlo simulation is used to generate forward and central samples of direct $c\bar{c}$ events passing all of the same requirements as the $b\bar{b}$ samples. The bottom and charm templates shown in Fig. 7.1 are from the central Monte Carlo samples, the distributions in the forward sample are similar. The heavy quark $c\tau$ distributions show the characteristic exponential decay corresponding to the respective average lifetimes for bottom (470$\mu$m) and charm (125–300$\mu$m) hadrons [44]. The dip at $c\tau = 0$ is due to the requirement $L_{xy}/\sigma > 2.0$, which produces a gradual fall off rather than a sharp cut. The negative tags, amounting to a few percent of the total, are due to events where the heavy quark decayed promptly and the finite resolution of the SVX leads to a reconstructed vertex behind the primary (cf. Fig. 5.4).

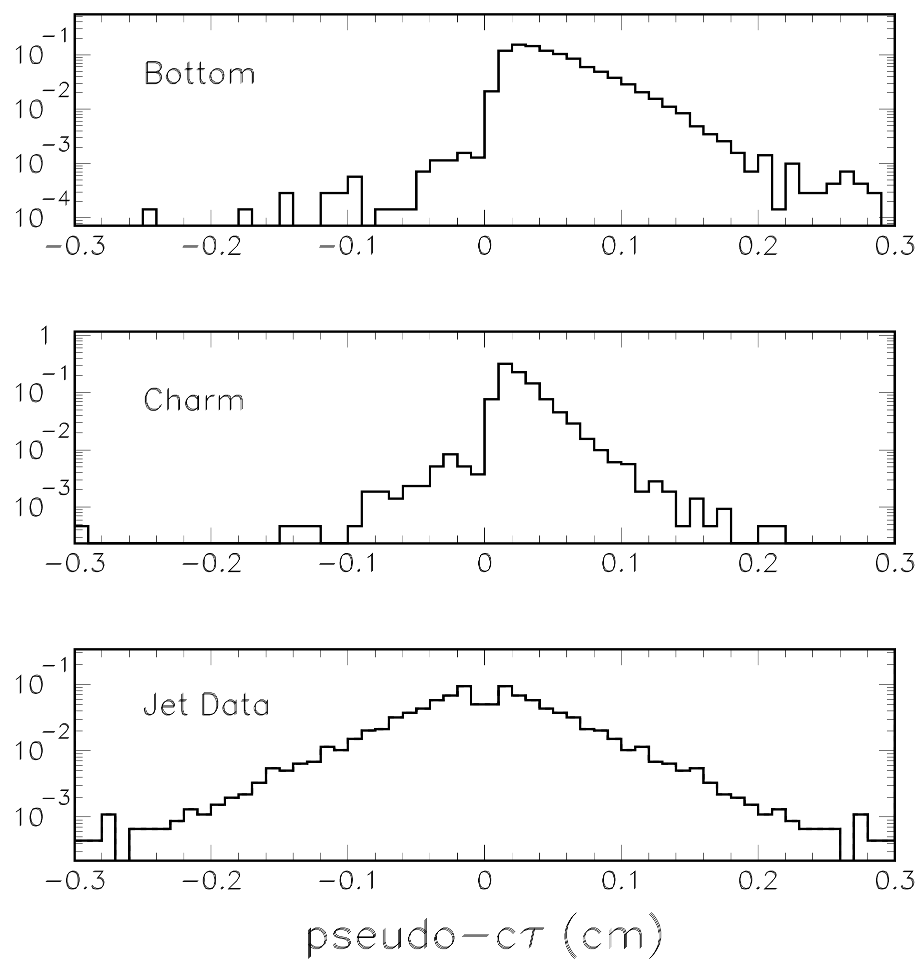


Figure 7.1: Pseudo-$c\tau$ distributions for the SVX-tag in bottom and charm CMUP Monte Carlo, and for the symmetrized negative tags in jet data.

The fake tag distribution is constructed in the following way. First, I note that fake tags from random track combinations are due to the finite resolution of the SVX and are symmetric with respect to $c\tau = 0$ [107]. Second, the fraction of heavy flavor tags with $L_{xy} < 0$ is only a few percent. I therefore derive the fake $c\tau$ distribution by symmetrizing the negative $L_{xy}$ tags in a sample of generic jet events collected with the CDF jet triggers [129]. The resulting distribution is the bottom plot in Fig. refctautemplates. Although this procedure ignores sources of real secondary vertices from the decay of long-lived particles, the tagging algorithm explicitly removes the majority of $K_S$ and $\Lambda$ decays (Sec. 5.3), and the track reconstruction algorithm removes tracks with a large kink that would arise from $\pi$ or $K$ decays.

$p_T^{\mathrm{rel}}$

Due to the large $b$ quark mass, muons from $b$ decay are, on average, more energetic and have a larger opening angle relative to the remaining decay products than do muons from the decay of hadrons containing charm or lighter quarks. This information is contained in the variable $p_T^{\mathrm{rel}}$, defined as the muon $p_T$ relative to the $\mu$-jet axis, Fig. 7.2. I calculate $p_T^{\mathrm{rel}}$ with the following equation,

$$p_T^{\mathrm{rel}} = p^{\mu} \sin\alpha, \tag{7.2}$$

where $\alpha$ is the angle between the muon and $\mu$-jet momenta, and $p^{\mu}$ is the total muon momentum. When determining $\alpha$, the muon minimum ionizing energy deposited in the calorimeter is not subtracted from the $\mu$-jet momentum vector. Although more precise techniques for determining the $b$ fraction exist in the central region of the CDF, the absence of precision track information capable of identifying secondary vertices in the forward region leaves $p_T^{\mathrm{rel}}$ as the only variable capable of separating

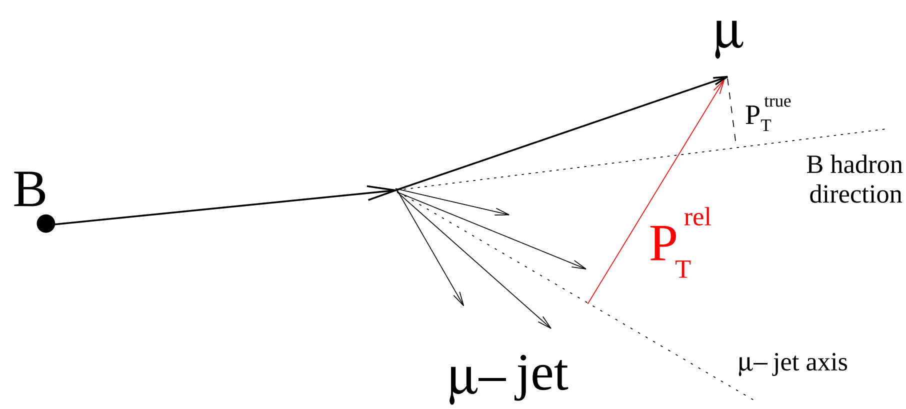


Figure 7.2: Diagram illustrating the definition of $p_T^{\rm rel}$.

$b$ decays from background. Using the same method in both samples acts as an indirect check on the forward fit result.

Fig. 7.3 shows a comparison between the $p_T^{\rm rel}$ distribution obtained from the central $b\bar{b}$ Monte Carlo sample and the subset of CMUP data events where the $\mu$-jet is also tagged by SECVTX. The double-tagged sample is expected to be dominated by $b$ decays, but the shape of the Monte Carlo distribution does not agree with the data. The forward $b\bar{b}$ Monte Carlo sample produces a $p_T^{\rm rel}$ distribution that looks identical to the central sample, and a similar discrepancy with the forward data is observed. Fig. 7.4 shows an attempt to fit the $p_T^{\rm rel}$ distributions in the forward and central samples using the default Monte Carlo. The forward fit prefers 100% $b\bar{b}$, while the central fit can accommodate a 15% charm component. In these plots the charm template was obtained from the same Monte Carlo sample used to produce the $c\tau$ templates. Clearly the shape of the $p_T^{\rm rel}$ distributions predicted by the simulation are not reproducing the shape observed in the data.

I have performed several checks to try and determine the source of the discrepancy between data and Monte Carlo $p_T^{\rm rel}$ distributions. Given the simple definition in Eq. 7.2, the problem is either with the muon momentum vector (magnitude or direction), the jet axis determination, or an unaccounted for background in the

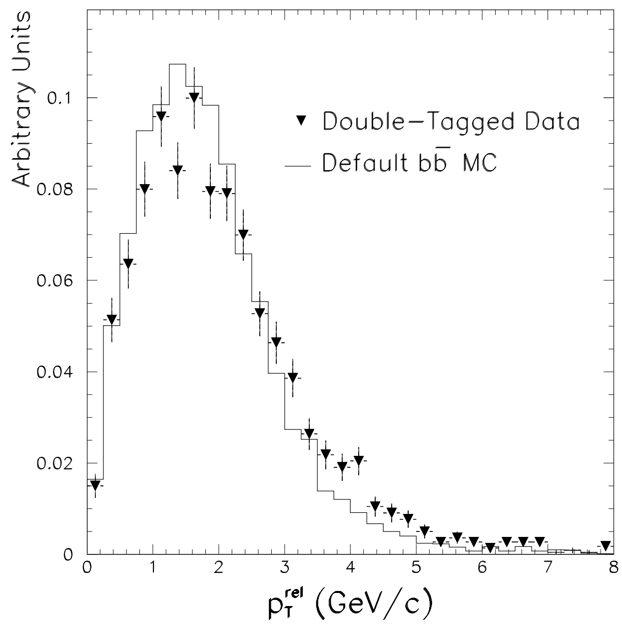


Figure 7.3: Comparison of $P_T^{\rm rel}$ distributions in $b\bar{b}$ Monte Carlo (hist) and double-tagged central data (points).

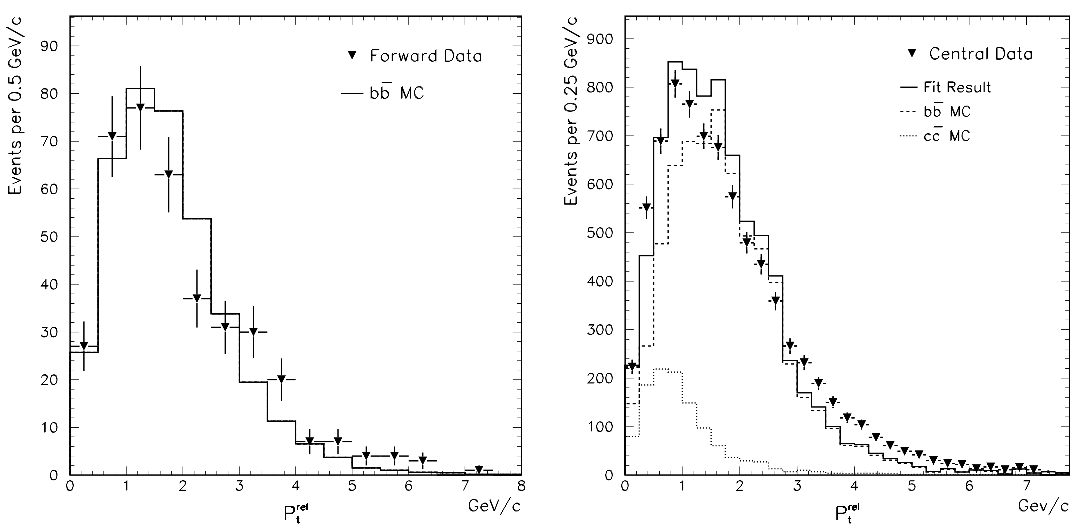


Figure 7.4: Forward $b\bar{b}$ Monte Carlo $p_T^{\rm rel}$ normalized to data (left), and the result of a fit to the central data using $b\bar{b}$ and $c\bar{c}$ Monte Carlo tempates (right).

data. As a check on the muon momentum determination, in Fig. 7.5 I show a comparison between the FMU and CMUP $p_T$ spectra in data and Monte Carlo using a combination of bottom and charm components taken from the fit results that will be obtained in the next section. The shape agrees in both samples, indicating that the problem does not lay in the generation and simulation of either forward or central muon momenta.

The central muon momentum direction is determined from the CTC track fit and the forward muon direction comes from the FMU track fit (for $\eta$) and pad hit correlation (for $\phi$). In both cases, the physics simulation is that of tracing a single charged particle through a known amount of material, which is a well understood procedure. Since the FMU pad hits are not simulated, the $\phi$ position is assigned to the center of the pad through which the generated muon passed. The azimuthal position is therefore known to an accuracy of $5^\circ/\sqrt{12}$ in the simulation. The same procedure is used in the data if a set of pad hits is successfully correlated with the track, and this is true for over 95% of the events in the forward data sample. I conclude that the problem does not lay in the simulation of the muon momentum vector.

A possible source of jet direction smearing not present in the Monte Carlo is additional energy in the jet cone from multiple interactions. To check whether the presence of multiple interactions is affecting the $p_T^{\mathrm{rel}}$ distribution, I divide the central data into events with 1 or 2 class 12 vertices, and events with 3 or more vertices. In Fig. 7.6 I compare the $p_T^{\mathrm{rel}}$ distributions in the two subsamples and find no significant dependence on number of vertices. This result eliminates extra energy in the jet cone as a possible source of the discrepancy between data and simulation. I therefore conclude that a problem exists in the simulation of the $\mu$-jet direction.

To test this hypothesis, in the central region I can define $p_T^{\mathrm{rel}}$ using tracking information, rather than calorimeter information, to determine the $\mu$-jet direction.

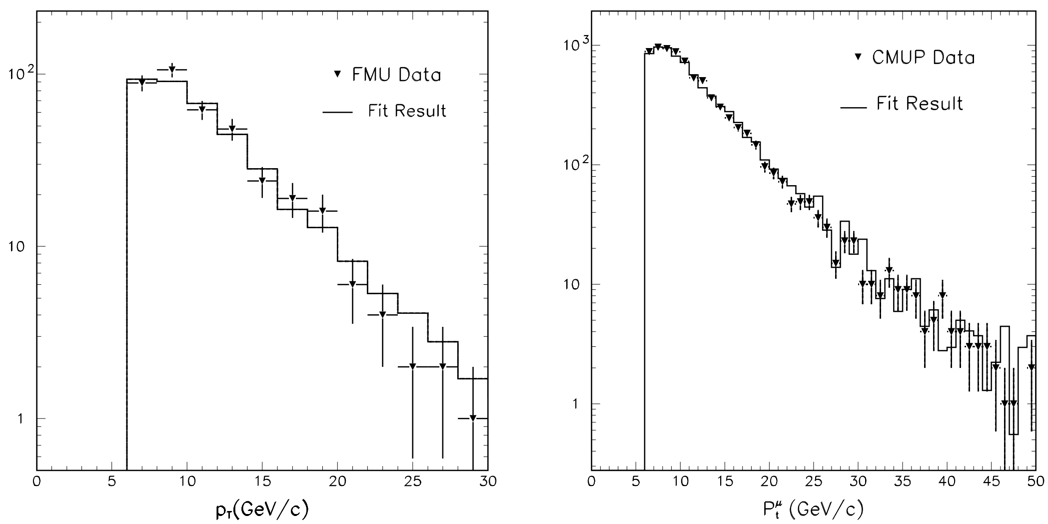


Figure 7.5: FMU (left) and CMUP (right) muon $p_T$ spectra compared to the sum of bottom and fake Monte Carlo with relative weights from the fit results in Table 7.1.

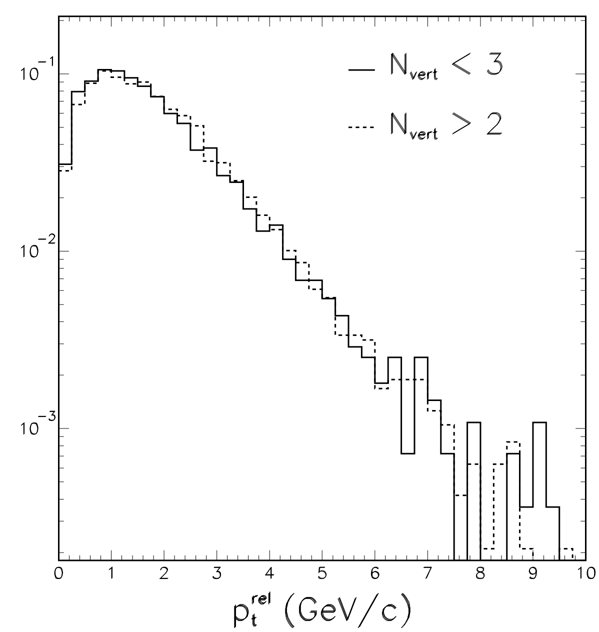


Figure 7.6: Comparison of the central data $p_T^{\mathrm{rel}}$ distribution for events with 1 or 2 (solid) vs. 3 or more (dash) class 12 vertices.

The track-based method has been used successfully in the CDF jet-charge $\Delta m_d$ measurement [130]. The track clustering algorithm is very similar to the energy clustering algorithm described in Sec. 3.2.2, with tracks replacing calorimeter towers. CTC tracks with $p_T > 1\,\mathrm{GeV}/c$ are used as seeds, to which other tracks with $p_T > 0.5\,\mathrm{GeV}/c$ are attached if they are within a cone of radius 0.4 in $\eta$-$\phi$ space. The $\mu$-jet is then unambiguously defined as the jet containing the muon track. I require the $\mu$-jet to have at least two additional tracks and calculate $p_T^{\mathrm{rel}}$ after subtracting the muon momentum from the jet.

In Fig. 7.7 I compare the track-based $p_T^{\mathrm{rel}}$ distribution obtained from double-tagged Monte Carlo events with the corresponding distribution obtained from the central double-tagged data. Very good agreement is found, which I interpret as evidence that there exists no unaccounted for background process in the data that is causing the discrepancy between the calorimeter-based $p_T^{\mathrm{rel}}$ shape predicted by Monte Carlo and the distribution observed in the data.

Given that the only difference between the two definitions of $p_T^{\mathrm{rel}}$ discussed above is the use of tracking information rather than calorimeter information, I conclude that the Monte Carlo does not accurately simulate the cluster centroid position resolution. Furthermore, the comparison in Fig. 7.3 indicates that the $\mu$-jet direction is more precisely known in the Monte Carlo than in the data. I have therefore developed a tuning procedure to correct for this deficiency on average by smearing the Monte Carlo calorimeter $\mu$-jet direction according to an unbiased calibration variable. The smearing procedure is described in detail in Appendix B. As a calibration variable I use the $\Delta\phi$ and $\Delta\eta$ between the calorimeter-based $\mu$-jet and the track-based $\mu$-jet. These distributions are more narrow in the Monte Carlo, which is exactly what one would expect if the position of the energy cluster centroid is known more precisely in the simulation than in the data. The procedure involves smearing the $\mu$-jet direction in $\eta$ and $\phi$ according to a gaussian distribution for some fraction of the events. The width of the gaussian and fraction of jets to

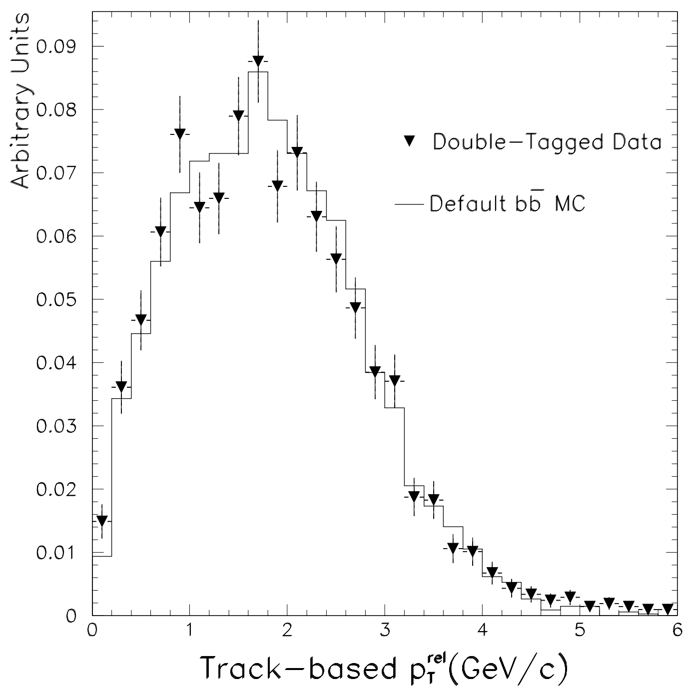


Figure 7.7: Comparison of the track-based $p_T^{\rm rel}$ template (hist) obtained from the default $b\bar{b}$ Monte Carlo, and the double-tagged central data (points).

smear are then tuned to reproduce the $\Delta\eta$ and $\Delta\phi$ distributions observed in data.

Fig. 7.8 shows a comparison between the resulting smeared $b\bar{b}$ Monte Carlo $p_T^{\rm rel}$ template and the central double-tagged data. The smeared distribution does a better job of describing the data than the default Monte Carlo. Since the default Monte Carlo predicts similar $p_T^{\rm rel}$ shapes in the forward and central samples, I apply the same smearing procedure to the forward sample. The distributions obtained from the forward and central smeared Monte Carlo samples are plotted together in Fig. 7.9, and these are the distributions I use as the $b\bar{b}$ $p_T^{\rm rel}$ templates.

Fig. 7.10 shows the $p_T^{\rm rel}$ template distributions for muons from charm and light meson decay, obtained with the same smearing procedure applied to the $b\bar{b}$ Monte Carlo events. Muons from $\pi$ and $K$ decay are modeled by generating gluon and

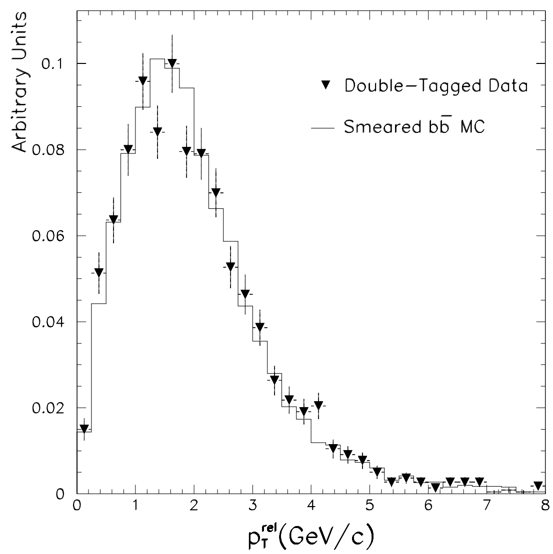


Figure 7.8: Same comparison as Fig. 7.3 showing the result of the smearing procedure on the Monte Carlo $b\bar{b}$ $p_T^{\mathrm{rel}}$ template.

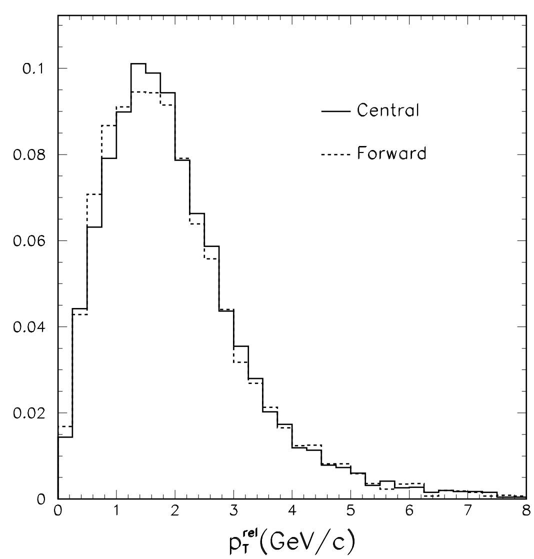


Figure 7.9: Comparison of the central (solid) and forward (dashed) smeared Monte Carlo $p_T^{\mathrm{rel}}$ distributions used as $b\bar{b}$ templates in the fits.

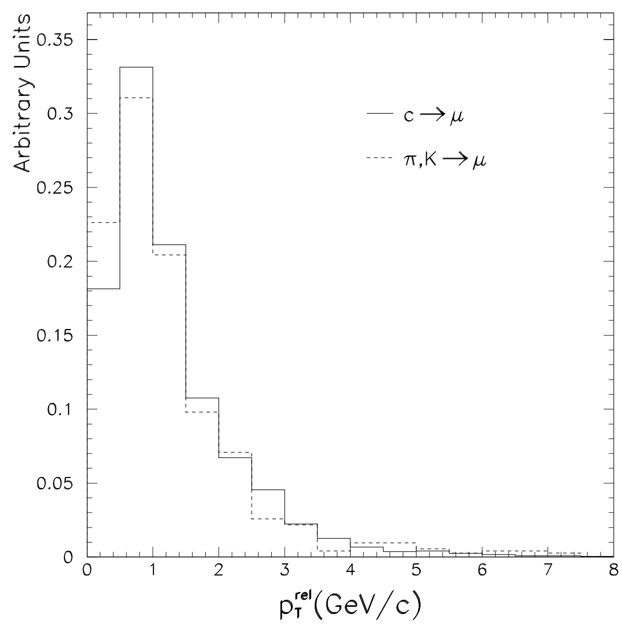


Figure 7.10: Distributions of $p_T^{\mathrm{rel}}$ for forward muons from charm (solid) and light mesons (dashed).

light quark events in ISAJET and decaying the produced mesons according to their respective muon branching fractions and lifetimes. Muons from mesons that decay before interacting in the calorimeter are simulated and subjected to the same requirements placed on muons from heavy quark decay. The comparison in Fig. 7.10 shows that $p_T^{\mathrm{rel}}$ cannot resolve the charm and decay-in-flight (DIF) components. I therefore use the charm distribution to represent both components in the fit and quote the difference obtained using the DIF template as a systematic uncertainty.

### 7.1.2 Fit Results

Since I am ignoring $b\bar{b}c\bar{c}$ production and the $p_T^{\mathrm{rel}}$ variable is unable to separate charm and DIF muons, there are five distinct components in the fit corresponding

**Fit Results**

| Component | Forward Fit | Central Fit |
|---|---|---|
| $f_{bb}$ | $0.815 \pm 0.060$ | $0.617 \pm 0.017$ |
| $f_{cc}$ | $0.083 \pm 0.051$ | $0.148 \pm 0.014$ |
| $f_{bf}$ | $0.000^{+0.059}_{-0.000}$ | $0.066 \pm 0.021$ |
| $f_{fb}$ | $0.017^{+0.047}_{-0.017}$ | $0.070 \pm 0.010$ |
| $f_{fc}$ | $0.086 \pm^{+0.035}_{-0.046}$ | $0.099 \pm 0.010$ |

Table 7.1: Fitted fractions for each component in the forward and central fits.

to the five combinations of $\mu$-tag and SVX-tag. I label these five components $f_{bb}$, $f_{cc}$, $f_{bf}$, $f_{fb}$, and $f_{fc}$, where the first and second indices indicate bottom ($b$), charm ($c$), and fake ($f$) SVX-tags and $\mu$-tags respectively. I perform a simultaneous binned maximum likelihood fit using pseudo-$c\tau$ and $p_T^{\mathrm{rel}}$. I exploit the fact that negative $L_{xy}$ tags are predominantly from non-heavy-flavor jets by separating the $p_T^{\mathrm{rel}}$ fit into two samples based on whether the accompanying SVX-tag has positive or negative $L_{xy}$. This procedure enables the individual determination of the two components with fake SVX-tags, $f_{fb}$ and $f_{fc}$.

The only constraint on the fit is that each component must be positive. The fit results are listed in Table 7.1. The $\chi^2$ per degree of freedom is 1.1 and 1.4 for the forward and central fits respectively. Combining the fitted signal fractions with the total number of events in each dataset, I determine that $311 \pm 23$ forward, and $4655 \pm 128$ central events are due to $b\bar{b}$ production where both quarks are correctly identified.

I show the pseudo-$c\tau$ and $p_T^{\mathrm{rel}}$ fit results for the forward and central samples in Figs. 7.11–7.14. For the $p_T^{\mathrm{rel}}$ results, the main plot shows the distribution in events where the SVX-tag has positive $L_{xy}$, while the inset shows the events with a negative $L_{xy}$ tag. As was mentioned, the negative SVX-tags are predominantly from non-heavy-flavor jets, and the sum $f_{fb}+f_{fc}$ is constrained by the total number of negative $L_{xy}$ events in each sample. The fraction of fake SVX-tags accompanied by a real $b$ decay on the $\mu$-tag side is then determined by the $p_T^{\rm rel}$ fit for the negative $L_{xy}$ events. Within the large statistical uncertainty, I find this fraction to be consistent with 50% in both samples. With $f_{fb}$ constrained in this way, the signal fraction $f_{bb}$ is then essentially determined by the total $b$ fraction on the $\mu$-tag side. Overall, the fit results are very reasonable. In particular, the fake SVX-tag template obtained from jet data fits the shape of the negative pseudo-$c\tau$ distribution in both samples, and the smeared Monte Carlo $p_T^{\rm rel}$ templates provide a good fit on the $\mu$-tag side.

### 7.1.3 $Z^0 \to b\bar{b}$ Subtraction

The expected number of events from $Z^0 \to b\bar{b}$ decay in both samples is calculated with the following equation,

$$N(Z^0 \to b\bar{b}) = \sigma(p\bar{p} \to Z^0 \to e^+e^-) \cdot \frac{Br(Z^0 \to b\bar{b})}{Br(Z^0 \to e^+e^-)} \cdot \mathcal{L}(\text{CDF}) \cdot \epsilon_{\rm tot}, \qquad (7.3)$$

where $\sigma$ is the $Z^0 \to e^+e^-$ cross section at the Tevatron, the ratio corrects for branching fractions, $\mathcal{L}(\text{CDF})$ is the CDF luminosity for this dataset $(77.1 \pm 6.2)\,\text{pb}^{-1}$, and $\epsilon_{\rm tot}$ is the total efficiency times acceptance for detecting a $b\bar{b}$ pair from $Z^0$ decay in each sample.

The most recent published CDF cross section for $Z^0 \to e^+e^-$ is $231 \pm 12$ pb [131]. The $b\bar{b}$ branching fraction is $(15.46 \pm .14)\%$ and the $e^+e^-$ branching fraction is $(3.366 \pm 0.008)\%$ [44]. The acceptance calculation is identical to that described in Section 6.2.2, with $Z^0$ production replacing QCD production in ISAJET. No cuts are placed on the $b\bar{b}$ pair so that the acceptance corrects back to the total $Z^0$ production cross section corresponding to the CDF measured value. The acceptance

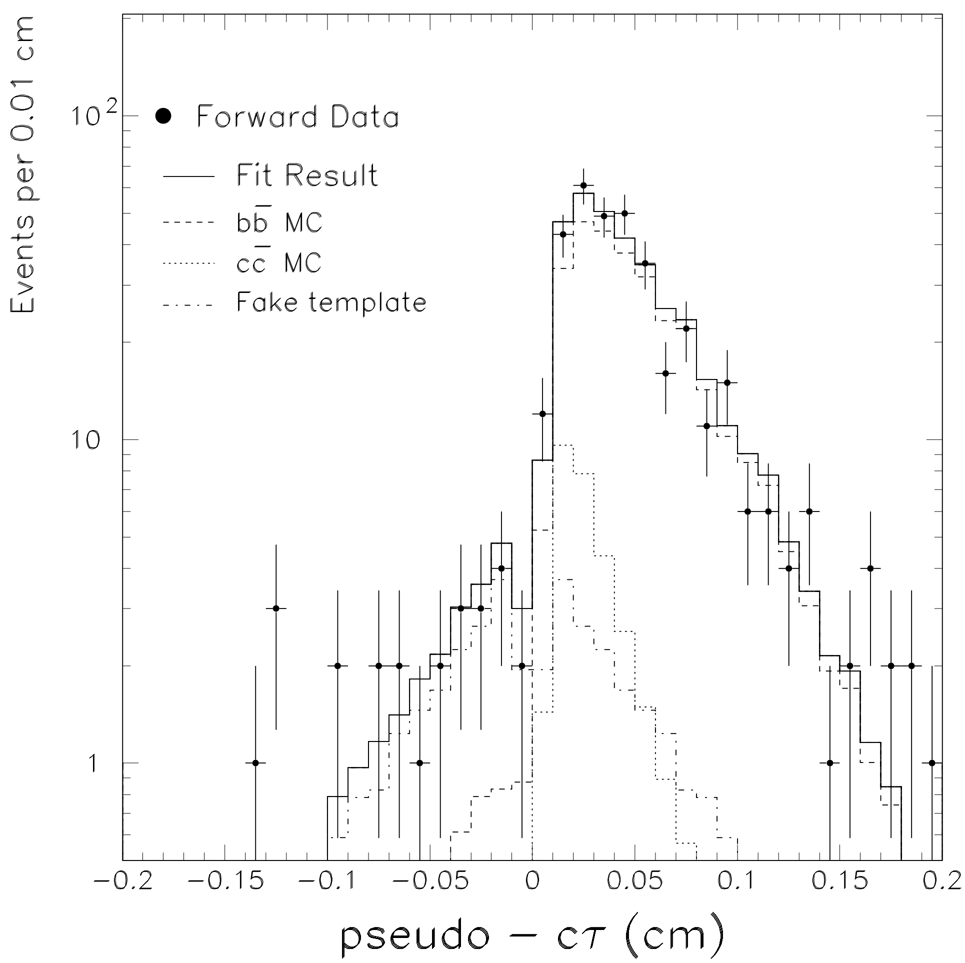


Figure 7.11: Forward data fit result for pseudo-$c\tau$.

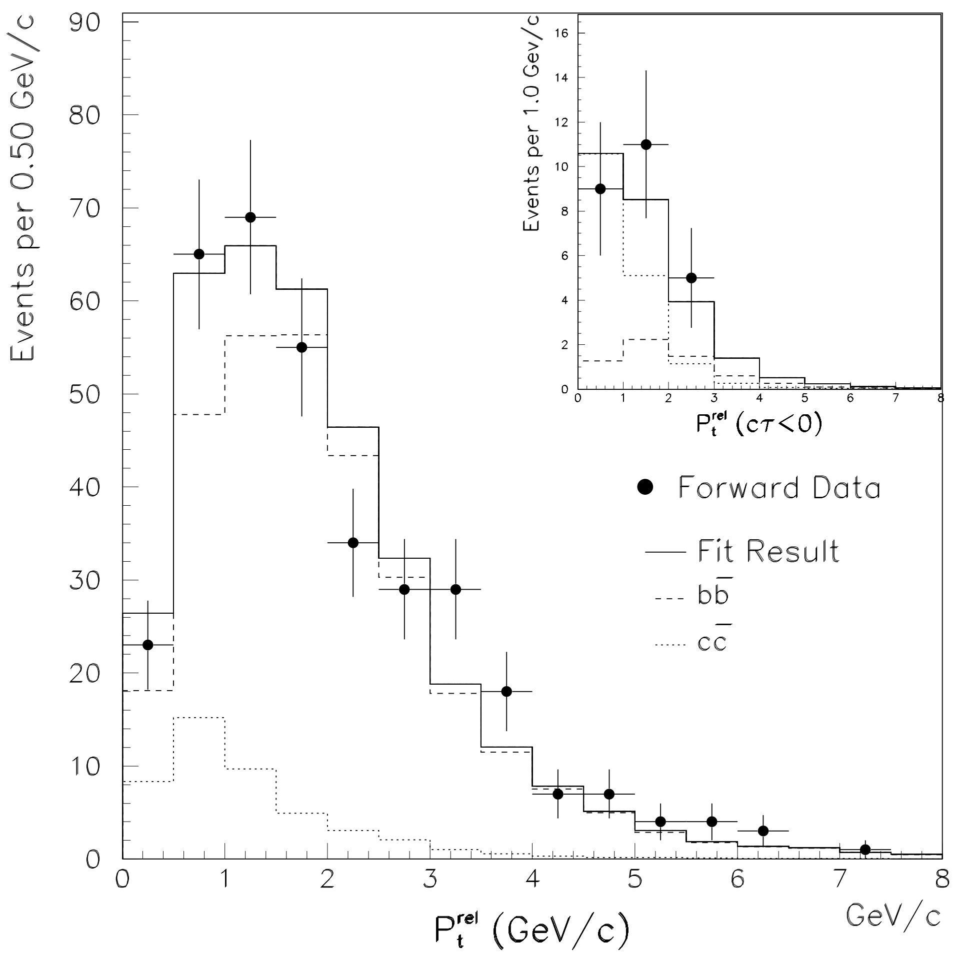


Figure 7.12: Forward data fit result for $p_T^{\rm rel}$. The main plot shows the distribution for events with $L_{xy} > 0$, while the inset is for events with $L_{xy} < 0$.

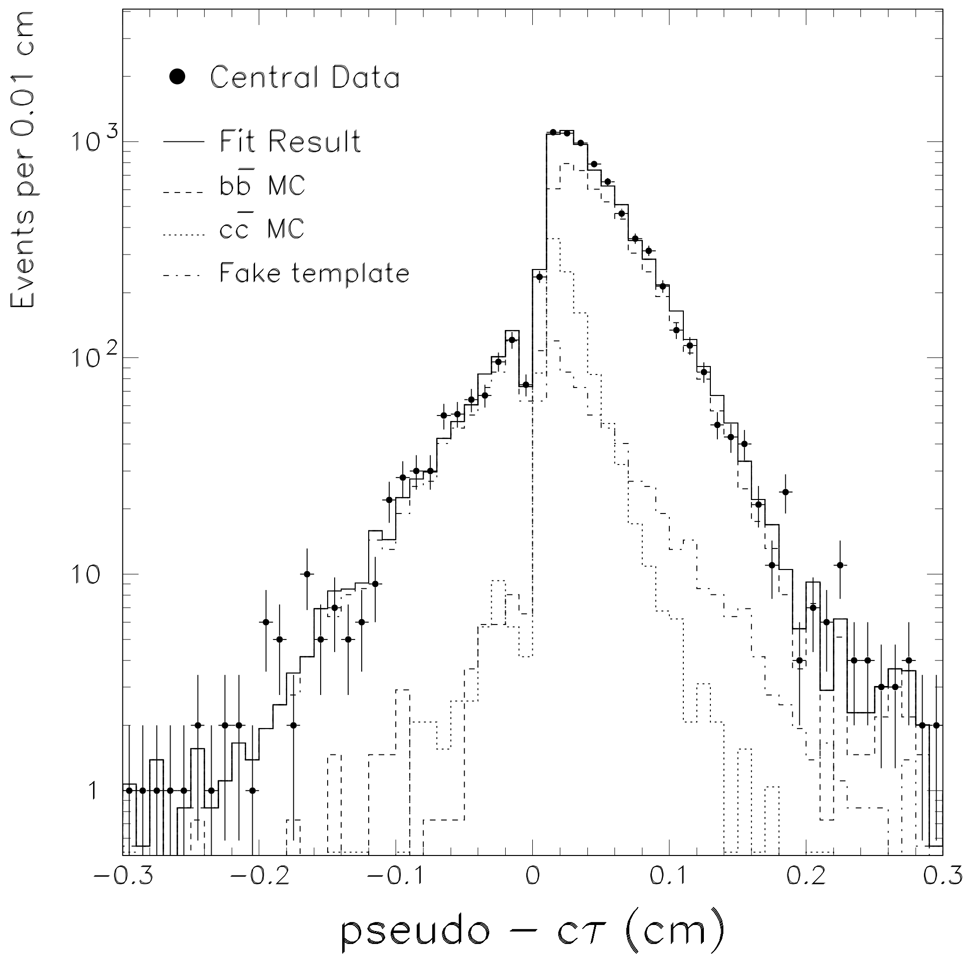


Figure 7.13: Central data fit result for pseudo-$c\tau$.

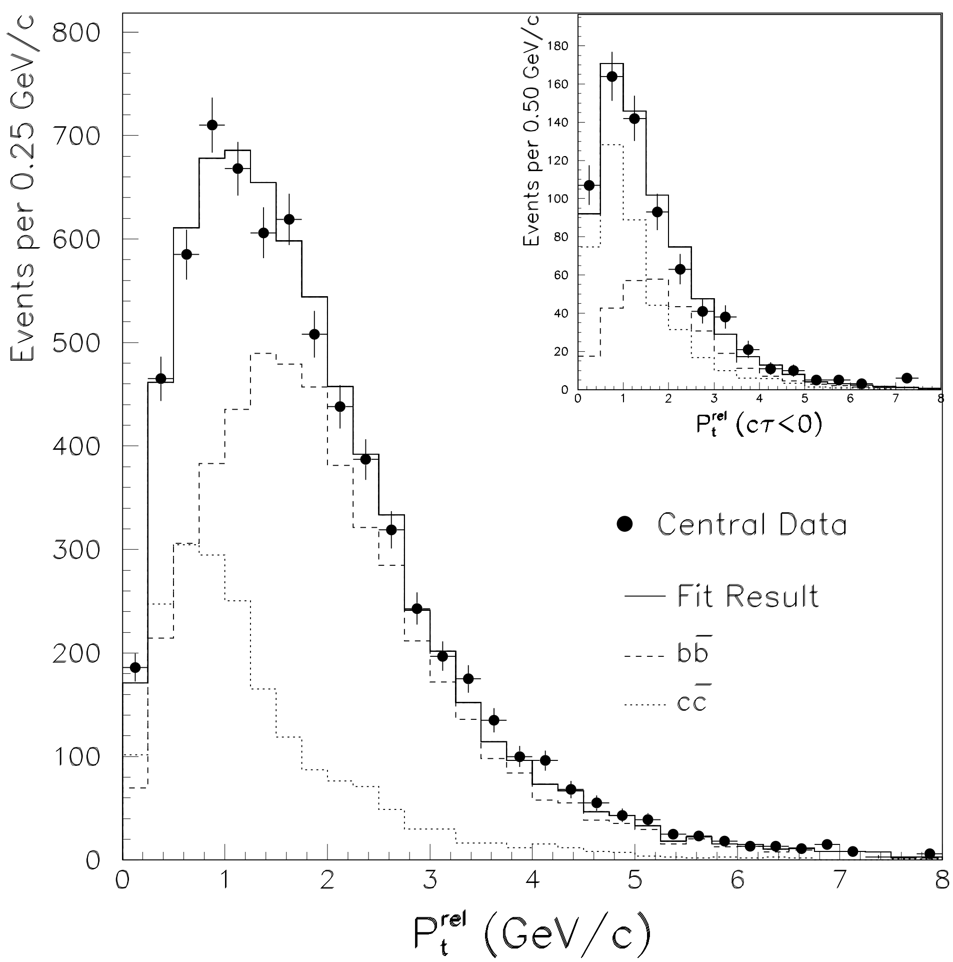


Figure 7.14: Central data fit result for $p_T^{\mathrm{rel}}$. The main plot shows the distribution for events with $L_{xy} > 0$, while the inset is for events with $L_{xy} < 0$.

is found to be $(1.30 \pm .05) \times 10^{-2}$ for the central sample, and $(1.05 \pm .05) \times 10^{-3}$ for the forward sample. Including the efficiency numbers in Tables 6.2 and 6.3, the vertex cut efficiency $(0.683 \pm 0.047)$ [132], the QFL′+SECVTX tagging efficiency scale factor[1] $(0.86 \pm 0.07)$ [133], and the $b\bar{b} \rightarrow \mu X$ branching fraction $(36 \pm 2.3)\%$, the total efficiency to detect a $b\bar{b}$ pair from $Z^0$ decay is $(2.53 \pm .33) \times 10^{-3}$ for the central sample, and $(5.07 \pm .69) \times 10^{-5}$ for the forward sample.

Putting all the numbers together, I determine that $203 \pm 33$ central, and $4.1 \pm .7$ forward events are due to $Z^0$ decay. Subtracting these events from the fitted number of signal events found in the previous section gives a final signal yield of $307 \pm 23$ forward, and $4452 \pm 132$ central $b\bar{b}$ events.

### 7.1.4 Consistency Checks

I use the symmetrized negative $L_{xy}$ tags in jet data for the shape of the fake SVX-tag background, a choice which relies on the assumption that the fake background is symmetric. To check this assumption I compare in Fig. 7.15 the jet data template with SECVTX-tagged generic Monte Carlo jets. The Monte Carlo sample was obtained by running the tagging algorithm on gluon and light quark jets generated in ISAJET. I did not require a $\mu$-tag in addition to the SVX-tag as the acceptance for this process is too small to simulate in a reasonable time. The comparison shows some disagreement near $c\tau = 0$. However, replacing the jet data template with the Monte Carlo template and refitting the data results in signal fractions of $0.806 \pm 0.059$ and $0.613 \pm 0.017$ for the forward and central data respectively. These results are in excellent agreement with the fits using the jet data template (cf. Table 7.1).

[1] The scale factor takes into account differences between the SECVTX tagging efficiency in data and Monte Carlo. I do not include this in the cross section ratio measurement because the effect cancels.

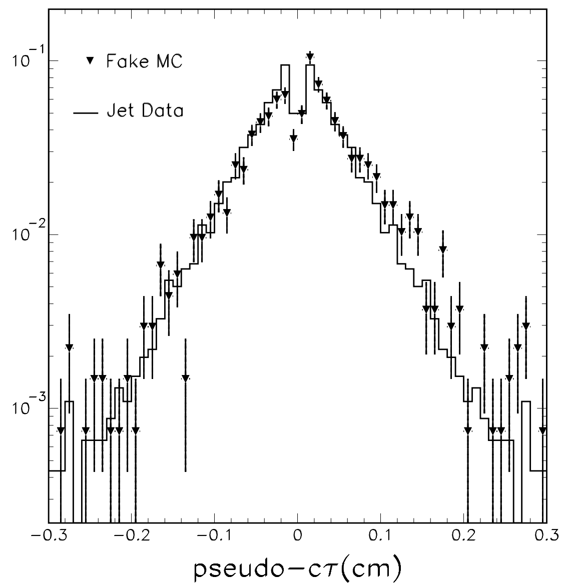


Figure 7.15: The pseudo-$c\tau$ distribution for Monte Carlo gluon and light quark jets, compared to the fake SVX-tag template derived from data.

As a second check on the pseudo-$c\tau$ fit, I substitute the mass $M$ of the secondary vertex for $c\tau$ and refit the data. As shown in Fig. 7.16, the mass and pseudo-$c\tau$ variables are largely uncorrelated, and therefore, represent independent estimators of the $b$ fraction in the SVX-tag. I use the same generic Monte Carlo sample described above to obtain the shape of the fake SVX-tag mass distribution. The bottom and charm templates come from the same samples used to obtain the pseudo-$c\tau$ templates. I find that the fit cannot independently separate the charm and fake components. The relative contribution of these two components are therefore fixed by the result obtained using $c\tau$. With this constraint, I find $b\bar{b}$ fractions of $0.767 \pm 0.051$ and $0.616 \pm 0.017$ for the forward and central fits respectively, which are consistent with the results using pseudo-$c\tau$. The mass fits are displayed in Fig. 7.17.

The $p_T^{\rm rel}$ variable is unable to separate muons from charm and light meson decay

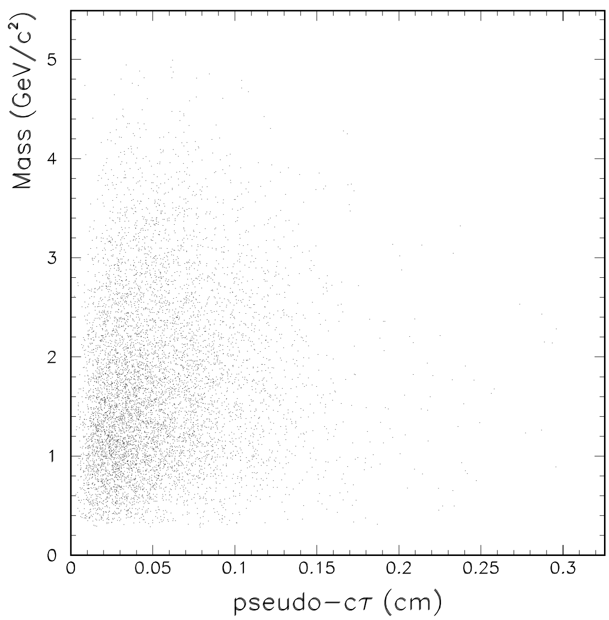


Figure 7.16: Scatter plot of SVX-tag mass vs. $c\tau$ in the forward sample.

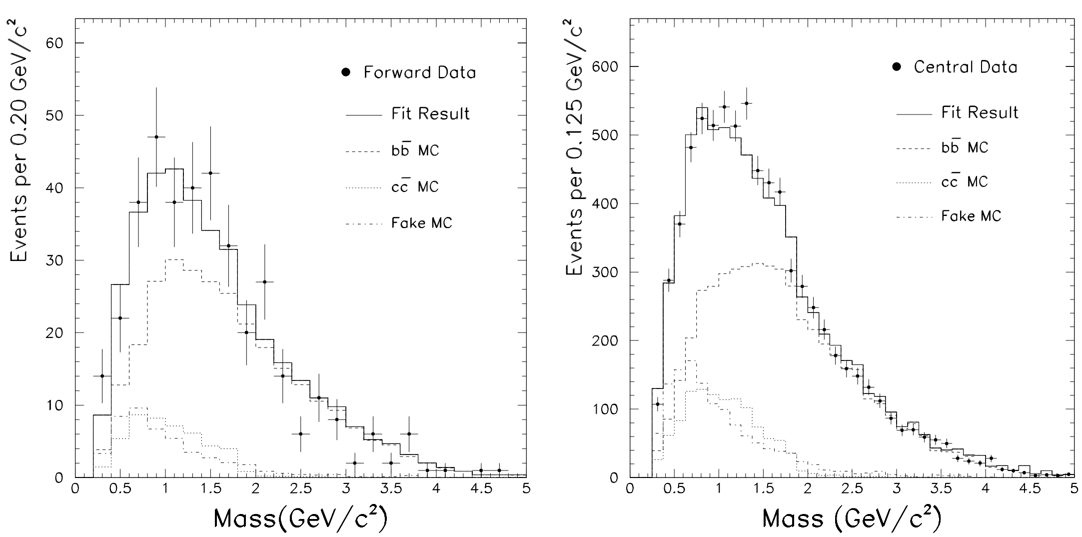


Figure 7.17: Fit results for the forward (left) and central (right) data using the mass of the secondary vertex and $p_T^{\rm rel}$.

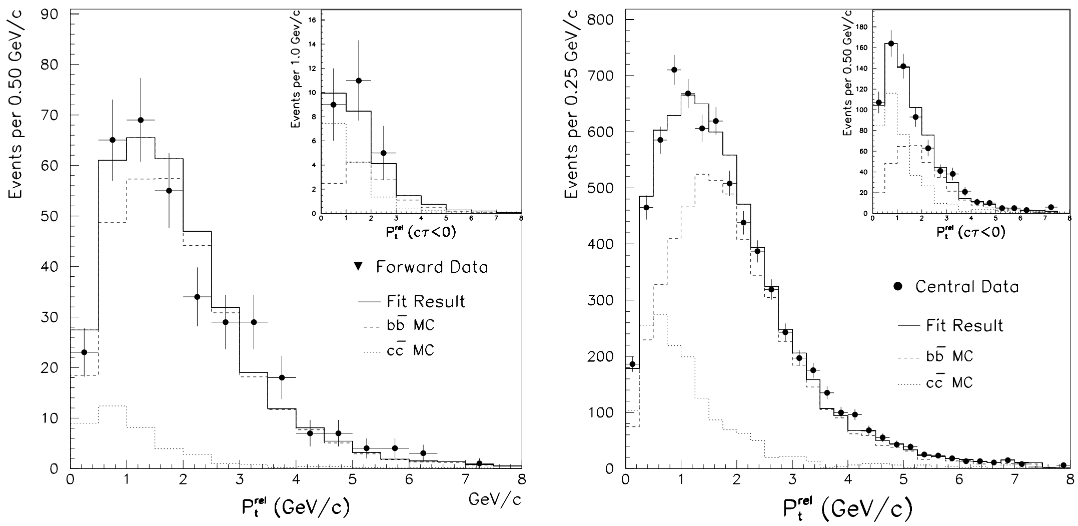


Figure 7.18: Fit results for the forward (left) and central (right) data using the decay-in-flight $p_T^{\rm rel}$ template instead of charm. Inset shows events with $L_{xy} < 0$.

(cf. Fig. 7.10). I therefore use the charm template to represent both components in the fits. This choice is somewhat arbitrary, so as a check I have substituted the DIF template and refit the data. The results are displayed in Fig. 7.18, where I find $b\bar{b}$ fractions of $0.822 \pm 0.056$ and $0.658 \pm 0.015$ in the forward and central samples respectively. The forward result is consistent with the fit using the charm $p_T^{\rm rel}$ template, but there is a systematic shift in the central sample. The relative difference in the ratio of $b\bar{b}$ events from the nominal fit is $-5.4\%$, and I include this as a systematic uncertainty.

As a final check, I refit the central data using the track-based $p_T^{\rm rel}$ definition described in Sec. 7.1.1. Since it was not necessary to modify the default Monte Carlo in order to obtain agreement with the data, the track-based $p_T^{\rm rel}$ fit is an independent check on the smearing procedure for the central sample. I find a $b\bar{b}$ fraction of $0.641 \pm 0.014$, which is approximately a $+1.5\sigma$ shift from the fit using smeared Monte Carlo, and I include this as a systematic uncertainty. The

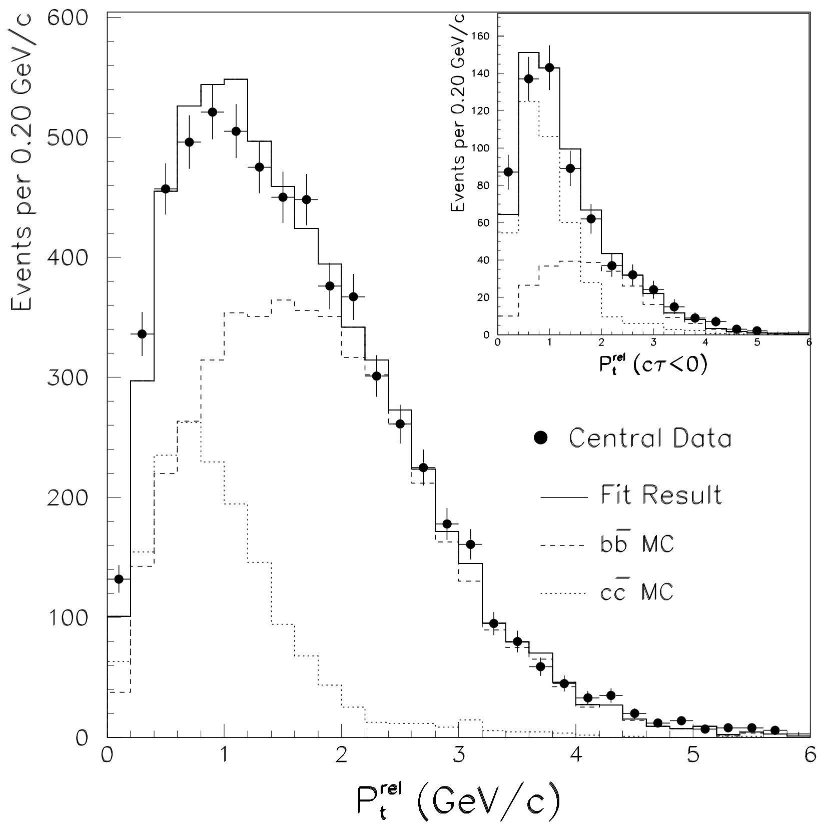


Figure 7.19: Result of the central muon data fit using $c\tau$ and track-based $p_T^{\mathrm{rel}}$.

track-based $p_T^{\mathrm{rel}}$ fit result is shown in Fig. 7.19.

The track-based $p_T^{\mathrm{rel}}$ fit results in a shift of $-3.9\%$ on the measured cross section ratio. I combine this result with the $-5.4\%$ shift due to using the DIF $p_T^{\mathrm{rel}}$ template and determine a total systematic uncertainty on the cross section ratio from the fitting procedure of $-6.7\%$.

## 7.2 Cross Section Results

The measured cross section ratio $R_{\text{data}}$ is defined and calculated with the following formula,

$$R_{\text{data}} = \frac{\sigma(p\bar{p} \to b_1 b_2 X; 2.0 < |y_{b_1}| < 2.6)}{\sigma(p\bar{p} \to b_1 b_2 X; |y_{b_1}| < 0.6)} = \frac{N^{\text{f}}_{bb}}{N^{\text{c}}_{bb}} \cdot \frac{\epsilon_{\text{c}}}{\epsilon_{\text{f}}}, \tag{7.4}$$

where $p_T(b_1, b_2) > 25\,\text{GeV}/c$, $|y_{b_2}| < 1.5$, and $\delta\phi(b_1 b_2) > 60°$ for both cross sections, $N^{\text{f(c)}}_{bb}$ are the number of background subtracted signal events in the forward (central) datasets, and $\epsilon_{\text{f(c)}}$ are the total efficiencies. Combining the efficiency results from Chapter 6 and the signal yields from Sec. 7.1.3, I find $R_{\text{data}} = 0.361 \pm 0.033$, where the error is statistical only.

### 7.2.1 Systematic Uncertainty and Final Result

The primary motivation for presenting the ratio of forward and central $b\bar{b}$ production rather than absolute cross sections is that many of the experimental uncertainties cancel; including the luminosity, the vertex $|z| < 30\,\text{cm}$ requirement, the muon branching fraction, and the SECVTX $b$-tagging efficiency. The remaining uncertainties are either reduced or were small to begin with. In this section I describe the estimation of these uncertainties.

#### Energy Scale

The uncertainty on the jet energy scale receives contributions from both the absolute and relative ($\eta$-dependent) corrections [106, 134]. The main sources of uncertainty on the absolute $E_T$ scale are calorimeter response, fragmentation, and underlying event. The combined systematic uncertainty for these effects is estimated to be 3.6% for corrected jet $E_T = 15\,\text{GeV}$, decreasing with increasing $E_T$,

Fig. 7.20. Fluctuating the $\mu$-jet and SECVTX-tagged jet $E_T$ cuts $\pm 3.6\%$ changes the event event yield by $^{+9.2}_{-10}\%$ and $^{+7.8}_{-7.3}\%$ in the forward and central samples respectively. The resulting shift in $R_{\rm data}$ is $^{+1.4}_{-3.2}\%$.

Uncertainty on the relative jet energy correction arises from finite statistics in the dijet balancing analysis. Since the correction, and therefore the uncertainty, depends on $\eta_D$, the effect of this uncertainty is determined by fluctuating the $E_T$ correction for all jets $\pm 1\sigma$(stat) and observing the change in event yield. I find the relative change in the number of events to be $^{+1.5}_{-0.5}\%$ in the forward data, and $\pm 0.6\%$ in the central data. The resulting change in $R_{\rm data}$ is $+1.0\%$.

### Fragmentation

For this analysis I have used the traditional value for the Peterson fragmentation parameter, $\epsilon = 0.006 \pm 0.002$ [55, 56]. Fluctuating $\epsilon$ within this uncertainty changes the acceptance by $^{+10}_{-7.2}\%$ and $^{+7.4}_{-7.6}\%$ for the forward and central samples respectively, resulting in an overal shift of $-2.7\%$ on $R_{\rm data}$. However, more recent experimental studies by the OPAL [135] and ALEPH [136] collaborations at LEP favor a value of $\epsilon$ closer to 0.003, and a theoretical study [137] using NLO evolution for the perturbative part of the fragmentation function obtained $\epsilon = 0.0015 \pm 0.0002$ using $\Lambda_5 = 200\,\mathrm{MeV}$. For future comparison with different theoretical results, I have evaluated the acceptance taking the limit $\epsilon \to 0$. I find individual shifts of $+78\%$ and $+52\%$ for the forward and central acceptance respectively. This results in a $-15\%$ shift in $R_{\rm data}$, which can be taken as the maximum range of uncertainty due to fragmentation effects.

### Tracking Efficiency

The CTC tracking efficiency systematically decreased over the course of the run due to increasing luminosity from the Tevatron and aging of the detector [116].

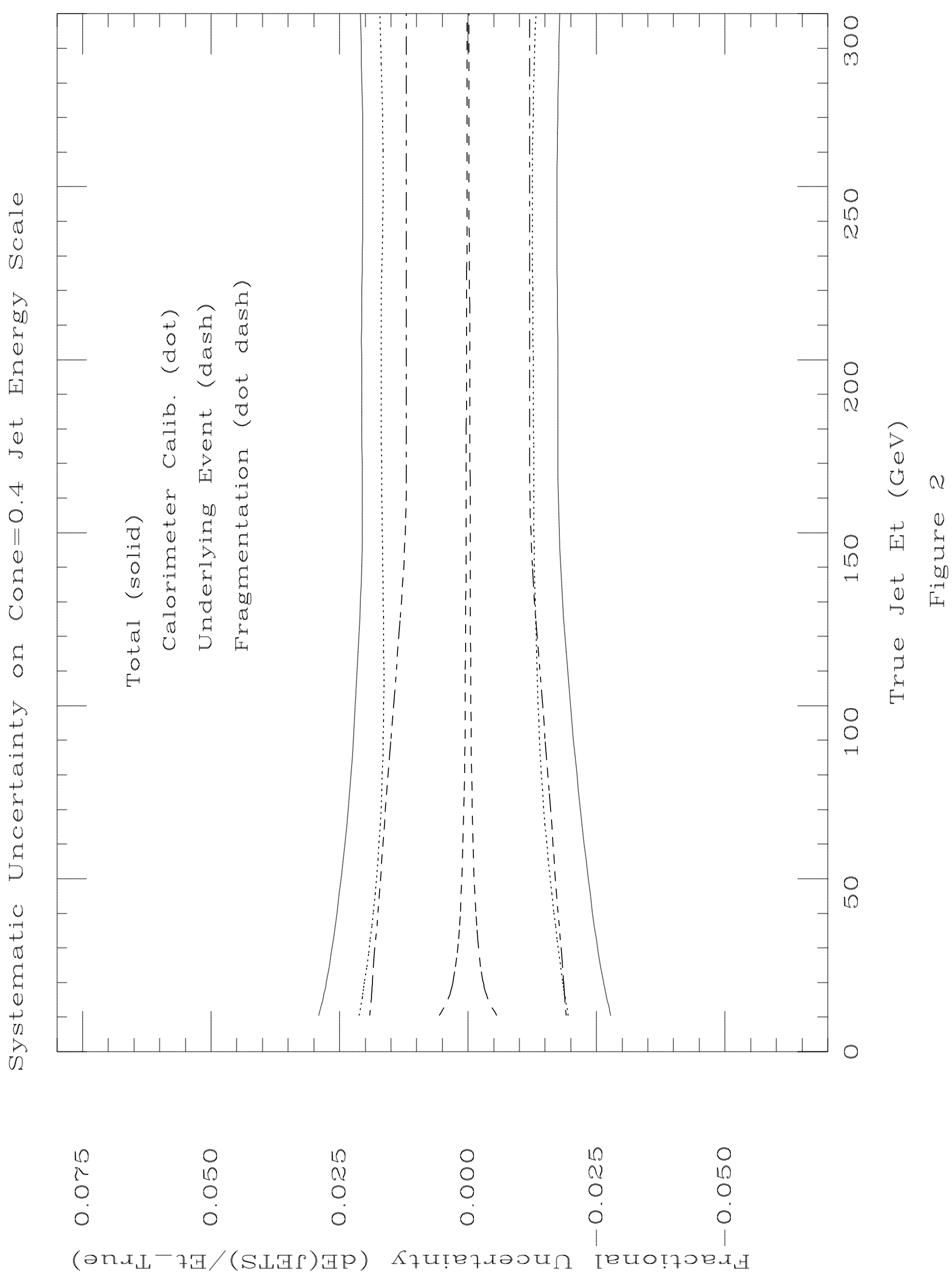


Figure 7.20: Individual and combined absolute jet energy scale uncertainties.

In Sec. 6.1.2, the efficiency was calculated as the luminosity-weighted average of the measured tracking efficiencies in three separate run ranges. I estimate the systematic uncertainty due to luminosity effects by taking the difference between the average luminosity and the high luminosity efficiencies, which is 1.4% [117]. I also include the systematic uncertainty quoted in [116], which was determined by taking the difference between the tracking efficiency obtained by using the CTC superlayer hit efficiencies measured in data, and the result assuming 100% hit efficiency. This uncertainty is 2.9%, which results in a total systematic uncertainty of 3.3% on the CTC tracking efficiency.

### Central Muon Trigger Efficiency

The uncertainty on the CMUP acceptance calculation was estimated by fluctuating the trigger curve parameters within their statistical uncertainties. In order to be conservative, the errors on all variables parameterizing a given trigger efficiency curve were assumed to be 100% correlated. The resulting systematic uncertainty is 1.7%.

### Total Systematic Uncertainty and Final Result

Finally, in Sec. 6.1.1 I found the uncertainty on the FMU level 3 occupancy cut to be $\pm 0.6\%$ by fluctuating the slope fit within its uncertainty, and the consistency checks in Sec. 7.1.4 resulted in an estimated uncertainty of $-6.7\%$ on the fit results. Table 7.2 summarizes the various sources of systematic uncertainty on $R_{\mathrm{data}}$. Adding the individual uncertainties in quadrature I determine a total systematic uncertainty of $^{+4.1}_{-8.7}\%$. The final result for the measured cross section ratio is

$$R_{\mathrm{data}} = 0.361 \pm 0.033\,(\mathrm{stat})^{+0.015}_{-0.031}\,(\mathrm{syst}). \tag{7.5}$$

**Summary of Systematic Uncertainties**

| Source | Uncertainty (%) |
|---|---|
| Jet $E_t$ scale (absolute) | $^{+1.4}_{-3.2}$ |
| Jet $E_t$ scale (relative) | $+1.0$ |
| Fragmentation | $-2.7$ ($-15$) |
| CTC tracking efficiency | $\pm 3.3$ |
| CMUP trigger efficiency | $\pm 1.7$ |
| FMU level 3 occupancy cut | $\pm 0.6$ |
| Fitting procedure | $-6.7$ |
| Total Systematic | $^{+4.1}_{-8.7}$ |

Table 7.2: Summary of systematic uncertainties on the cross section ratio. The fragmentation systematic in parentheses indicates the change on $R_{\mathrm{data}}$ when $\epsilon \to 0$.

## 7.3 Comparison with Theory

I compare the measured ratio to the NLO QCD prediction of Ref. [19] using MRSA$'$ PDFs, $m_b = 4.75\,\mathrm{GeV}/c^2$, and renormalization/factorization scale $\mu_0 = \sqrt{m_b^2 + \langle p_T \rangle^2}$, where $\langle p_T \rangle$ is the average $p_T$ of the $b$ and $\bar{b}$. In calculating the theoretical result, $R_{QCD}$, I apply the cross section definition cuts from Table 1.1. The results are listed in Table 7.3 for three values of the scale factor. I take $\mu = \mu_0$ to be the central value, and I use the extreme values to estimate the systematic uncertainty. The theory prediction is $R_{QCD} = 0.338^{+0.014}_{-0.097}$, in good agreement with the experimental result.

In Fig. 7.21 I compare the measured result (error bar) with the predicted shape of $R_{QCD} = \sigma(y_{b_1})/\sigma(|y_{b_1}| < 0.6)$ as a function of $y_{b_1}$ (filled boxes) integrated over rapidity bins of width 0.6 and normalized to the central bin. To illustrate that the $b$ quark rapidity distribution does not change significantly between LO and NLO,

**Theory Prediction**

| Scale | Central (nb) | Forward (nb) | Forward/Central |
|---|---|---|---|
| $\mu_0$ | $5.11 \pm 0.12$ | $1.72 \pm 0.06$ | $0.338 \pm 0.014$ |
| $2\mu_0$ | $6.32 \pm 0.17$ | $1.92 \pm 0.09$ | $0.304 \pm 0.017$ |
| $\mu_0/2$ | $1.88 \pm 0.21$ | $0.455 \pm 0.078$ | $0.241 \pm 0.049$ |

Table 7.3: Theory predictions for the central, forward, and ratio of cross sections obtained from the HVQ code.

the Born cross section is shown as a dashed line in each bin. Due to the strong rapidity correlation between the $b$ and $\bar{b}$, the predicted $d\sigma/dy_{b_1}$ distribution falls off rapidly once the trigger $b$ is detected outside the rapidity range occupied by the second $b$ ($|y_{b_2}| < 1.5$). The good agreement between our measurement and theory is the first direct evidence that the rapidity correlation predicted by QCD is correct.

As mentioned in Sec. 1.1, the shape of the rapidity distribution at large $y$ is sensitive to the gluon distribution in the proton at large $x$. In Fig. 7.22 I plot the fraction of proton momentum carried by the colliding partons in ISAJET forward $b\bar{b}$ events satisfying the cross section definition, where the $x$ values were calculated at the generator level using Eq. 2.8. For this final state topology, the parton travelling in the direction of the forward $b$ quark has momentum in the range $0.1 < x < 0.7$, while the second parton is in the range $0.005 < x < 0.1$. This measurement is therefore sensitive to $G(x, Q^2)$ in the region where it is not currently well-known ($x > 0.15$).

To get an idea of the variation in gluon distributions in the region probed by this analysis, in Fig. 7.23 I show the gluon luminosity $G(x_1)G(x_2)$ as a function of $y_{b_1}$ for the MRSR2 [138] (dashed), CTEQ4HJ[24] (dotted), and MRST [139] (dot-dash) PDFs normalized to the MRSA$'$ gluon. The transformation from momentum

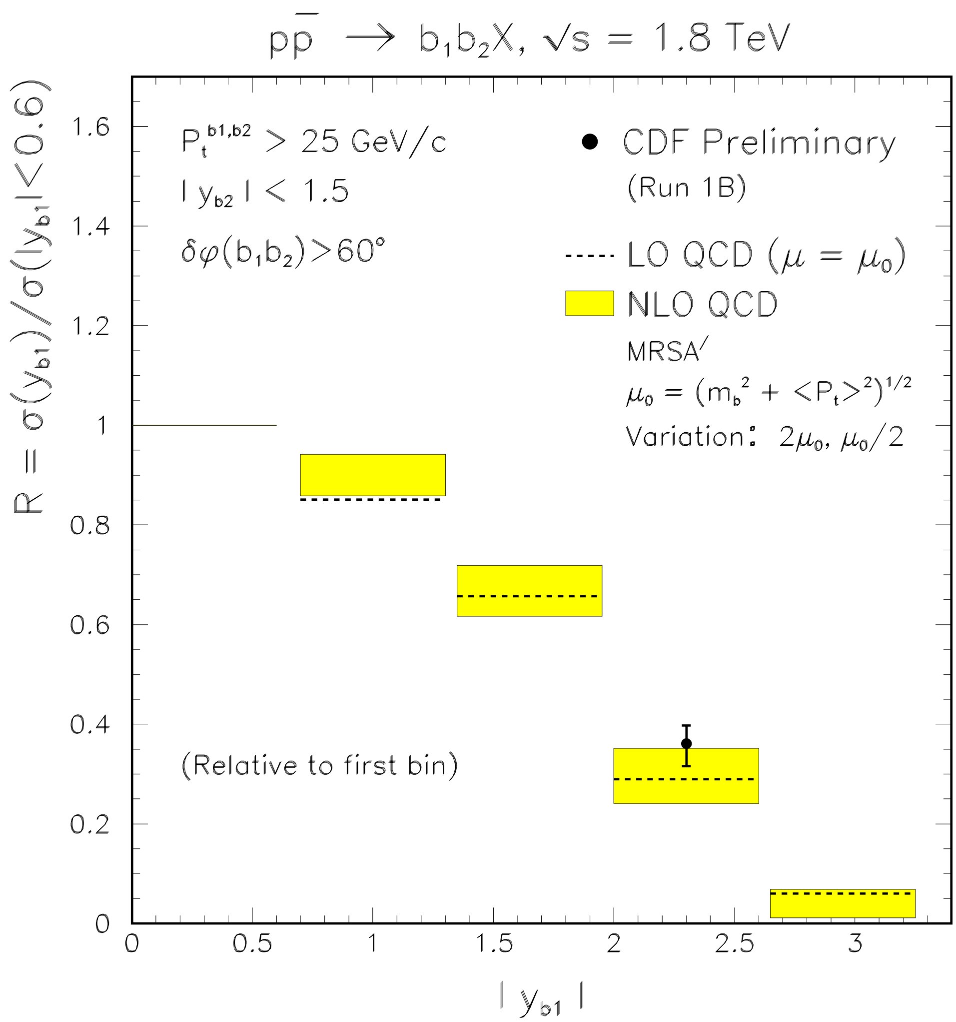


Figure 7.21: The normalized rapidity distribution of the trigger $b$.

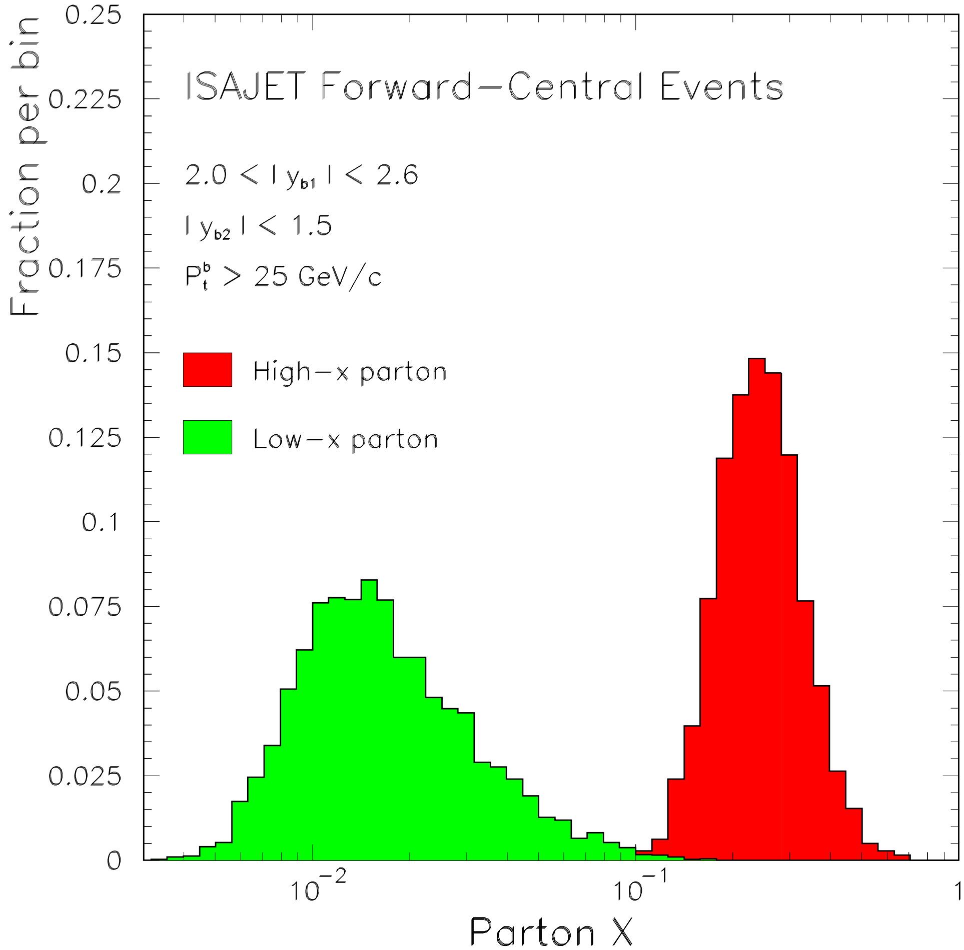


Figure 7.22: The fraction of hadron momentum carried by the colliding partons in ISAJET forward $b\bar{b}$ production.

fraction to rapidity is facilitated by setting $y_{b_2} = 0$ and $Q = 40\,\mathrm{GeV}$ in Eq. 2.8, where the $Q$ value is approximated by the mean $p_T$ of $b$ quarks in the Monte Carlo samples. To simulate the cross section ratio measurement, all of the curves are normalized to unity at $y_{b_1} = 0$. The rapidity range sampled by this measurement is indicated by the arrows.

Fig. 7.23 shows significant differences between the various gluon parameterizations, which arise from the different constraints used in the global fits. The MRSR2 PDFs are a modern version of the MRSA$'$ set, which utilize more recent HERA data and a value of $\alpha_s$ more consistent with the world average (0.120). There is correspondingly little difference between the two gluon parameterizations from these sets. In contrast, the CTEQ4HJ gluon was specifically designed to fit the high $E_T$ jet data measured by CDF [140] and DØ [141]. The result is a rapid rise at high-$x$, or equivalently, large rapidity. Since the total momentum carried by gluons is well-constrained, the increase at large $x$ must be accompanied by a decrease at lower momentum fraction, which happens to occur in the region sampled by this measurement.

The MRST parton set represents the first systematic attempt to include $k_T$ smearing when fitting prompt photon data as part of a global parton distribution analysis. They obtain three different parameterizations corresponding to $\langle k_T \rangle$ values of 0.0, 0.4, and $0.64\,\mathrm{GeV}/c$. Since a larger $\langle k_T \rangle$ is compensated by a smaller gluon distribution, the three parameterizations are referred to as MRST($g\uparrow$), MRST, and MRST($g\downarrow$). I show in Fig. 7.23 the MRST gluon, which is significantly smaller than MRSA$'$ in the region dominated by prompt photon data. Although not shown, the MRST($g\uparrow$) gluon, which includes no $k_T$ smearing, is consistent with MRSA$'$, while MRST($g\downarrow$) is approximately 60% lower. Also not shown in Fig. 7.23 is the CTEQ4M [24] gluon, which is a "best fit" parameterization similar to MRSA$'$ and MRSR2. In Fig. 7.24 I compare the measured cross section ratio with the NLO QCD predictions using the PDFs described above. To better discern

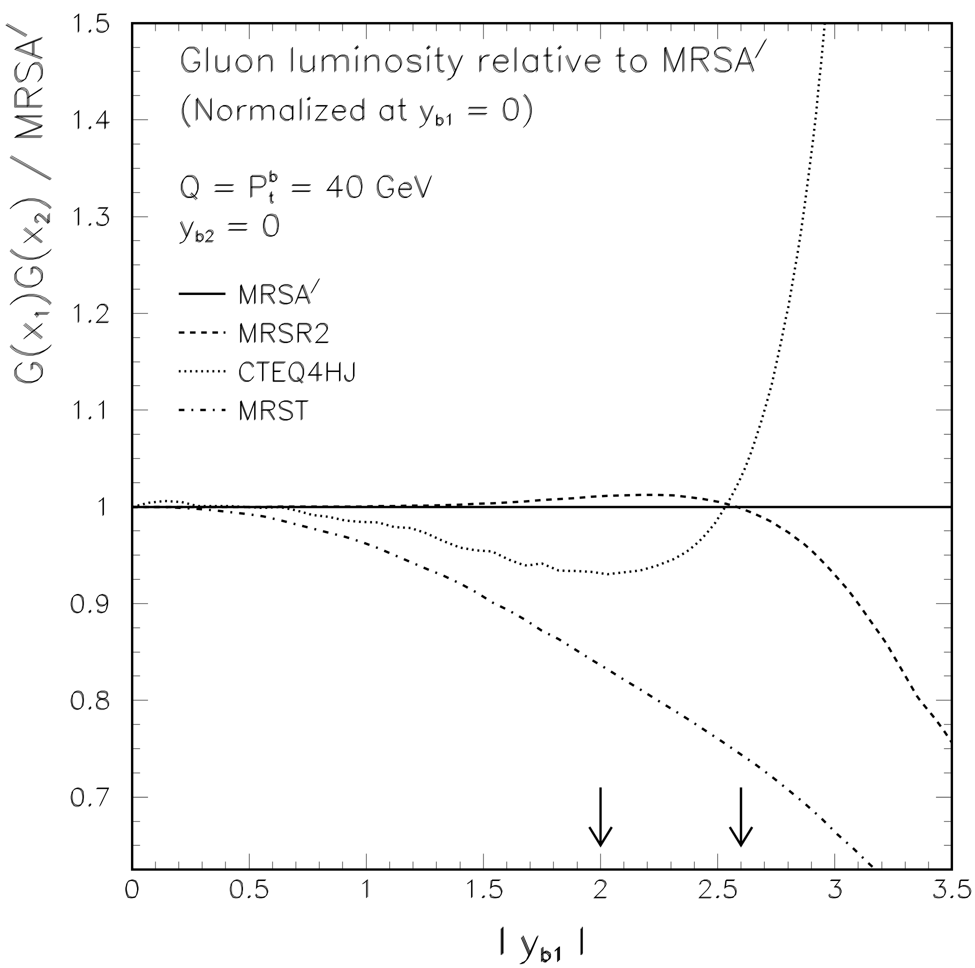


Figure 7.23: Comparison of the gluon luminosity for MRSR2, CTEQ4HJ, and MRST PDFs relative to MRSA′, as a function of $|y_b|$.

the differences between the various theory curves, the results are presented in the format data/theory, where the data point and the theory curves are divided by the result using MRSA$'$. The vertical error bars at the end of each theory curve indicate the statistical uncertainty from the Monte Carlo integration, I do not include the variation with scale in this plot. The measurement error is combined statistical and systematic.

As suggested by the comparison in Fig. 7.23, good agreement is found between data and QCD using the MRSR2 PDFs, while the CTEQ4HJ and MRST results are lower by approximately 1.5 and 2.0$\sigma$ respectively. However, I note that taking the extreme value of Peterson $\epsilon = 0$ decreases $R_{\mathrm{data}}$ by 15% (Sec. 7.2.1), which would bring the measured result into agreement with the CTEQ4HJ prediction, and within 1$\sigma$ of the MRST result. I conclude that it would be premature to claim that this result excludes either of these two parton distribution functions. The current ambiguity in the exact form of the $b$ quark fragmentation function limits the precision with which the gluon distribution can be constrained by this forward $b$ production measurement. However, the result does represent an independent constraint on the gluon distribution in a region of $x$ sampled by only a few experiments directly sensitive to $G(x, Q^2)$. Whether the "correct" gluon distribution is CTEQ4HJ or MRST, this measurement confirms the QCD prediction within the $\approx$ 15% fragmentation uncertainty.

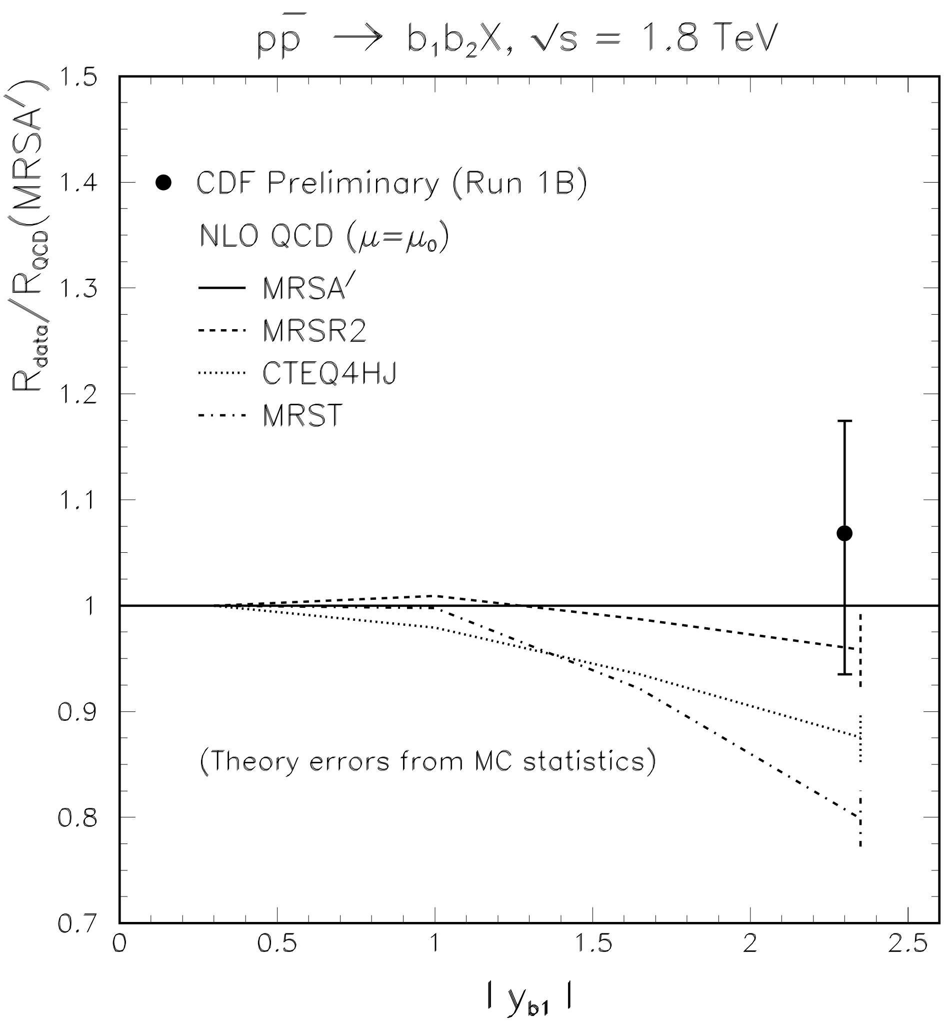


Figure 7.24: Comparison of the ratio $R = \sigma(|y_{b_1}|)/\sigma(|y_{b_1}| < 0.6)$ between data and theory using MRSA′, MRSR2, CTEQ4HJ, and MRST PDFs.

# Chapter 8

# Summary

In this thesis I have presented the first measurement of $b\bar{b}$ rapidity correlations at a hadron collider. Using data collected with the CDF forward and central high-$p_T$ muon triggers, two independent samples were accumulated corresponding to events enriched in forward and central $b$ decays respectively. The SECVTX $b$-tagging algorithm was then used to identify central jets likely to contain a heavy quark. The fraction of events in each sample due to $b\bar{b}$ production was determined by simultaneously fitting $p_T^{\mathrm{rel}}$ between the muon and $\mu$-jet, and the transverse decay length of the tagged $b$-jets. The resulting signal purity was 80% and 60% in the forward and central data respectively.

I have measured the ratio of forward-central to central-central $b\bar{b}$ production and find $R_{\mathrm{data}} = 0.361 \pm 0.033^{+0.015}_{-0.031}$, where the first uncertainty is statistical and the second is systematic. This result is in good agreement with the NLO QCD prediction using MRSA$'$ PDFs, $R_{\mathrm{QCD}} = 0.338^{+0.014}_{-0.097}$, and represents the first experimental evidence confirming the strong $b\bar{b}$ rapidity correlation predicted by theory. A comparison with the theory result using MRSR2 PDFs also shows good agreement, while the predctions using CTEQ4HJ and MRST PDFs indicate reasonable agreement within the large (15%) estimated uncertainty due to ambiguity in the exact shape of the $b$ quark fragmentation function. This uncertainty is comparable to the current variation in the gluon distribution due to uncertainty in the correct parameterization of initial state $k_T$ smearing when analyzing prompt photon data. Given the small number of measurements directly sensitive to the gluon distribution at high-$x$, the result presented in this thesis represents an important additional constraint that could reduce the range of possible gluon parameterizations at high-$x$ once it is encorporated into the global analyses.

# Appendix A

# File-Weighted vs. Run-Weighted Prescale Efficiencies

Prescaling introduces an inefficiency which can be calculated from the number of triggers before and after the prescale factor is applied. The effective luminosity is the product of the prescale efficiency and the CDF luminosity, and can be calculated in two ways, by run or file. In the run-weighted method the CDF luminosity in each run is weighted by the average prescale efficiency for that run. If $N_{ij}^{\mathrm{b}}$ and $N_{ij}^{\mathrm{a}}$ are the trigger counts in file $j$, run $i$, before and after prescaling, and $\mathcal{L}_i^{\mathrm{CDF}}$ is the CDF luminosity for run $i$, the prescaled luminosity is given by

$$\mathcal{L}_{\mathrm{rw}} = \sum_i \frac{\sum_j N_{ij}^{\mathrm{a}}}{\sum_j N_{ij}^{\mathrm{b}}} \mathcal{L}_i^{\mathrm{CDF}}. \tag{A.1}$$

The scaler values, $N_i^{\mathrm{a(b)}} = \sum_j N_{ij}^{\mathrm{a(b)}}$, are obtained from the last (or close to the last) event in each run. This is the method used by LUM_CONTROL. Alternatively, the prescaled luminosity can be calculated by weighting the CDF luminosity in each file by the average prescale efficiency for that file,

$$\mathcal{L}_{\mathrm{fw}} = \sum_i \sum_j \frac{N_{ij}^{\mathrm{a}}}{N_{ij}^{\mathrm{b}}} \mathcal{L}_{ij}^{\mathrm{CDF}}, \tag{A.2}$$

where $\mathcal{L}_{ij}^{\mathrm{CDF}}$ is the CDF luminosity in file $j$ of run $i$. In this case, the scaler values are obtained from the first and last events in a given file. This method will be referred to as the file-weighted method.

For non-dynamically prescaled triggers the efficiency is $1/p$, where $p$ is the prescale factor, within statistical fluctuations, which implies that

$$\frac{N_{ij}^{\mathrm{a}}}{N_{ij}^{\mathrm{b}}} \stackrel{\mathrm{all}\, j,k}{=} \frac{N_{ik}^{\mathrm{a}}}{N_{ik}^{\mathrm{b}}} = \frac{\sum_l N_{il}^{\mathrm{a}}}{\sum_l N_{il}^{\mathrm{b}}}, \tag{A.3}$$

and consequently, $\mathcal{L}_{\mathrm{rw}} = \mathcal{L}_{\mathrm{fw}}$. So for triggers with a constant prescale factor, both methods yield the same answer and LUM_CONTROL remains the best estimate. Conversely, if the prescale varies over the course of a run then the efficiency will also vary from file to file. The question arises as to what condition(s) must hold for the two methods to give the same result for dynamically prescaled triggers. Substituting $N_{ij}^{\mathrm{b}} = \sigma_{ij}\mathcal{L}_{ij}^{\mathrm{CDF}}$ in Eqs. A.1 and A.2 gives

$$\mathcal{L}_{\mathrm{rw}} = \sum_i \frac{\sum_j N_{ij}^{\mathrm{a}}}{\sum_j \sigma_{ij}\mathcal{L}_{ij}^{\mathrm{CDF}}} \mathcal{L}_i^{\mathrm{CDF}}, \tag{A.4}$$

and

$$\mathcal{L}_{\mathrm{fw}} = \sum_i \sum_j \frac{N_{ij}^{\mathrm{a}}}{\sigma_{ij}\mathcal{L}_{ij}^{\mathrm{CDF}}} \mathcal{L}_{ij}^{\mathrm{CDF}}, \tag{A.5}$$

where $\sigma$ is the trigger cross section. It is clear from these two equations that the only sufficient condition for obtaining $\mathcal{L}_{\mathrm{rw}} = \mathcal{L}_{\mathrm{fw}}$, is if the trigger cross section is constant. It is important to note that even if the integrated luminosity per file were exactly equal, if the trigger cross section varies in a systematic way over the course of a run, the two methods will not give equal answers. This is because the file-weighted method takes into account variations in the trigger cross section, while the run-weighted method does not.

To illustrate this point, in Figure A.1 I show a luminosity summary for Run 70627. The horizontal axis in each plot is integrated luminosity and each point

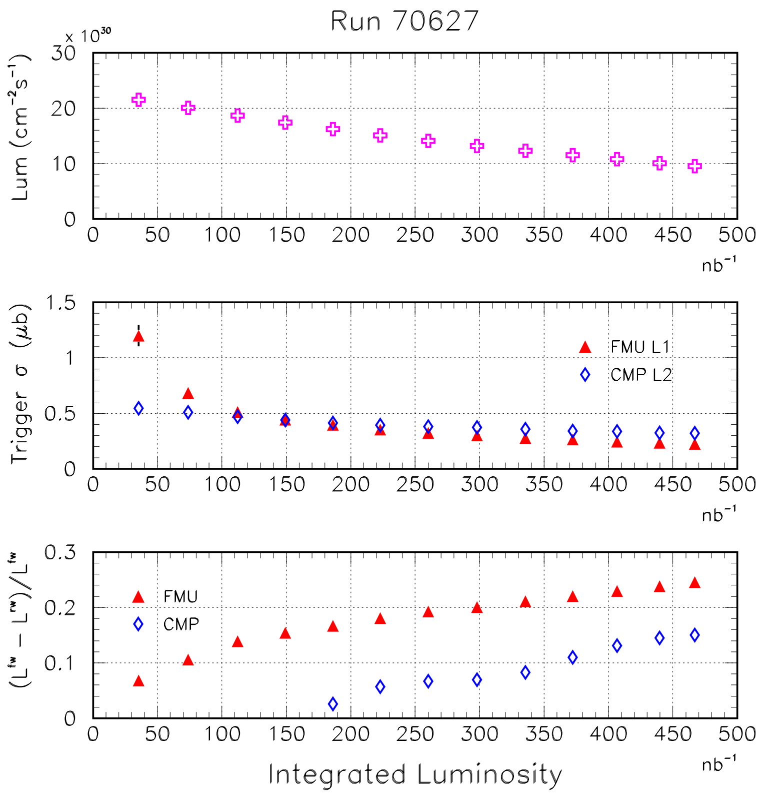


Figure A.1: Luminosity information from Run 70627. See text for details.

| $\mathcal{L}(10^{30}\,\mathrm{cm}^{-2}\,\mathrm{s}^{-1})$ | Prescale Factor |
|---|---|
| 22.2 | 32 |
| 17.9 | 31 |
| 16.3 | 13 |
| 15.5 | 8 |
| 12.3 | 4 |
| 11.5 | 2 |
| 10.6 | 1 |

Table A.1: Variation of CMUP prescale factor in Run 70627.

represents the combined data of five files. The top plot shows the instantaneous luminosity, which fell from an initial value of 22 to $10 \times 10^{30}\,\mathrm{cm}^{-2}\mathrm{s}^{-1}$ over the course of the run. The middle plot shows the trigger cross section, obtained by dividing the number of triggers before the prescale by the integrated luminosity for that file. The large initial cross section for the FMU level 1 trigger was due to background from Tevatron losses at high luminosity. The central muon trigger cross section drops from 550 to 300 nb. Finally, the bottom plot shows the relative difference between $\mathcal{L}_{\mathrm{fw}}$ and $\mathcal{L}_{\mathrm{rw}}$ for the two triggers, where $\mathcal{L}_{\mathrm{rw}}$ was calculated at each point by assuming the run had ended there.

Table A.1 shows how the CMUP trigger prescale changed over the course of this run. Referring to the bottom plot in Fig. A.1, the first four bins are zero for the CMUP trigger because the prescale value did not change significantly. After the instantaneous luminosity fell to $16 \times 10^{30}$ the prescale value changed by over a factor of two and the run-weighted method began to underestimate the integrated luminosity. Since the FMU trigger was rate-limited, the instantaneous prescale value was proportional to $\sigma\mathcal{L}^{\mathrm{inst}}$ and the difference between the two methods could be seen immediately.

The plots in Figure A.1 show that even though the integrated luminosity per file was roughly constant, as can be seen from the equal spacing between data points, the falling trigger cross sections caused the run-weighted method to underestimate the luminosity relative to the file-weighted method. This was evident immediately for the FMU trigger, and after each change in the prescale factor for the CMUP trigger. Again, this is because the run-weighted method ignores file-to-file variations in the trigger cross section. Earlier files, where the prescale efficiency is lower, carry more weight in the denominator of Eq. A.4, and consequently, the run-weighted method understimates the average prescale efficiency. In contrast, the ratio in Eq. A.5 weights the prescale efficiency for each file equally, giving a more accurate estimate of the average prescale efficiency.

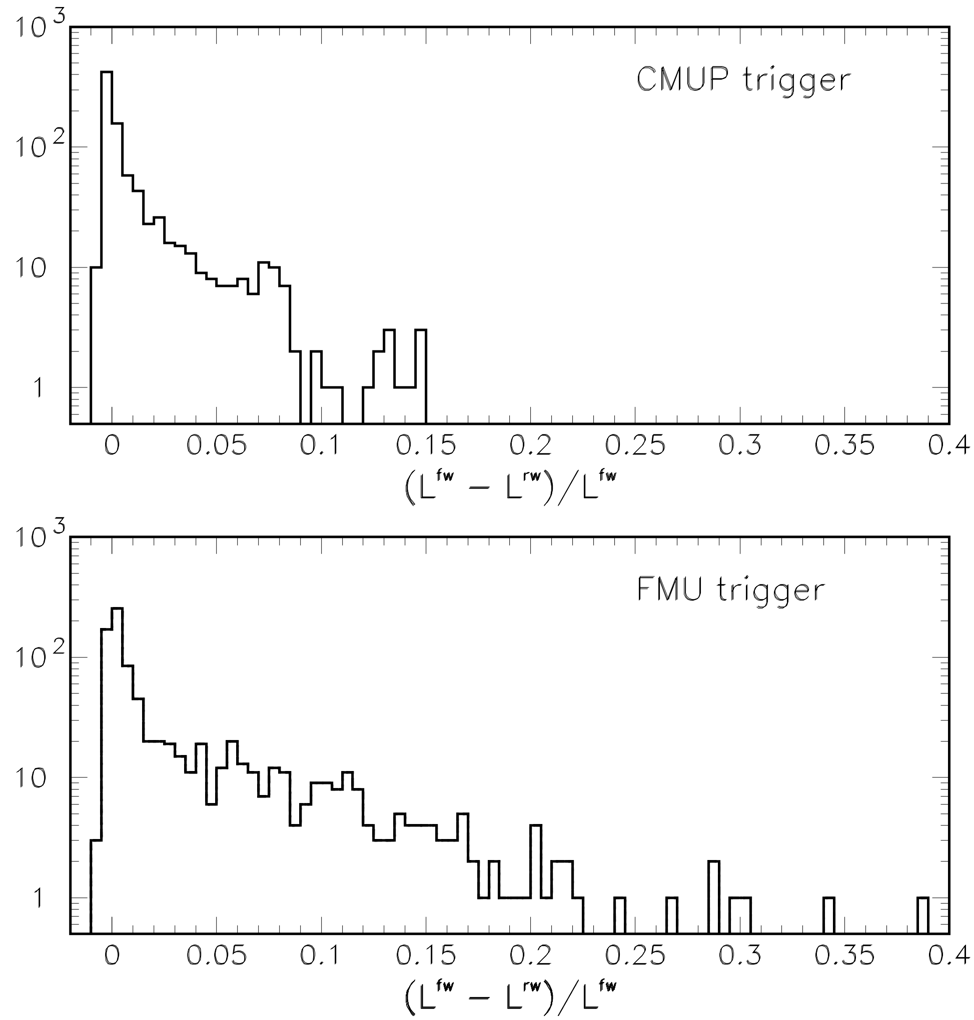


Figure A.2: Relative difference per run between prescaled luminosity calculated with the file-weighted and run-weighted methods.

For this particular run, which began at high luminosity and had a long livetime, the descrepancy between the two methods is +15% for the CMUP trigger and +25% for the FMU trigger, which is two and three times the total uncertainty on the CDF luminosity, respectively. Of course, most runs did not have such high luminosity and the average difference is only a few percent for both triggers, Fig. A.2.

# Appendix B

# Monte Carlo Smearing Procedure

In Section 7.1.1 it was shown that the default $b\bar{b}$ Monte Carlo using calorimeter-based jets does not reproduce the $p_T^{\rm rel}$ distribution observed in the central double-tagged data (Fig. 7.3). It was also shown that if track-based jets are used to define $p_T^{\rm rel}$ good agreement is found (Fig. 7.7). The conclusion is that the default Monte Carlo does not accurately simulate the calorimeter $\mu$-jet direction relative to the muon. In this appendix I describe a smearing procedure designed to correct for this effect.

In order to calibrate the Monte Carlo a variable is needed that can be compared in both data and Monte Carlo. Since I find good agreement in the $p_T^{\rm rel}$ variable using track-based jets, I choose as calibration variables the difference in azimuth ($\delta\phi$) and pseudorapidity ($\delta\eta$) between the calorimeter and track-based $\mu$-jets. In Fig. B.1 I show the $\delta\phi$ distributions obtained in Monte Carlo and data. The distributions are well-reproduced by the sum of two gaussians, and as suspected, the Monte Carlo distribution is narrower than the corresponding data, indicating that the $\mu$-jet direction is known with better precision than is observed in the data. The $\delta\eta$ distributions show a similar discrepancy.

I correct the Monte Carlo on average by smearing the $\mu$-jet direction in $\eta$ and $\phi$ in order to reproduce the $\delta\eta$ and $\delta\phi$ distributions observed in data. Since these distributions are parameterized by the sum of two gaussians, simply smearing all events with a single gaussian is insufficient. I determined by trial and error that smearing the $\mu$-jet $\eta$ and $\phi$ in 25% of the events according to a gaussian with $\bar{x} = 0$

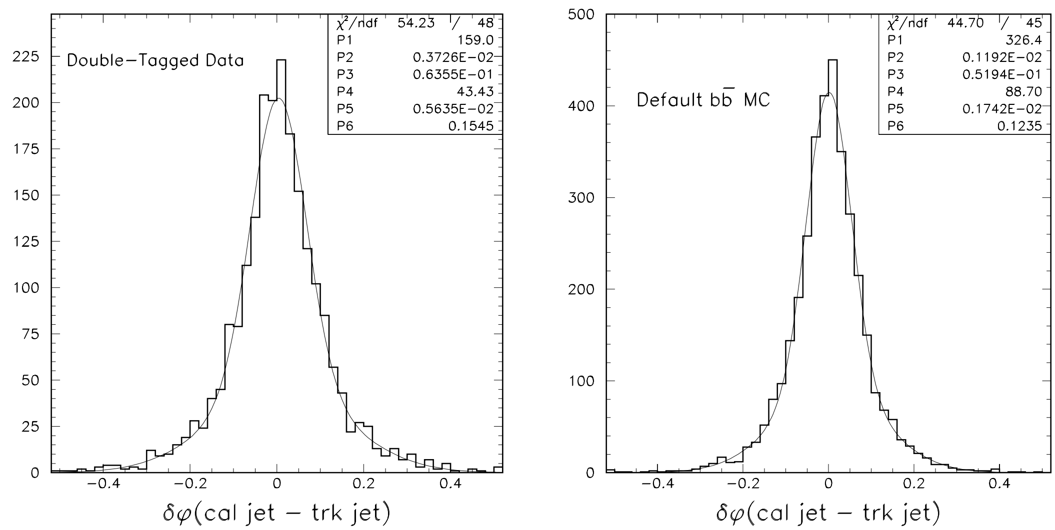


Figure B.1: The azimuthal difference between the track-based $\mu$-jet and the calorimeter $\mu$-jet in the double-tagged sample (left) and in default $b\bar{b}$ Monte Carlo (right).

and $\sigma = 0.12$ reproduces the $\delta\eta$ and $\delta\phi$ distributions seen in the data. Fig. B.2 shows the resulting smeared Monte Carlo distributions compared with data.

The effect of the smearing procedure on $p_T^{\rm rel}$ is illustrated in Fig. B.3, where I compare the $b\bar{b}$ Monte Carlo before and after smearing. Since randomly smearing the $\mu$-jet direction will lead, on average, to an increase in the opening angle with respect to the muon, the overall effect on $p_T^{\rm rel}$ is to broaden the width and lengthen the tail, which is exactly the effect needed to bring the Monte Carlo shape into agreement with the data. As already mentioned in the discussion of Fig. 7.8, the agreement with the double-tagged data is indeed much improved. This smearing procedure is applied to all of the Monte Carlo samples used to generate $p_T^{\rm rel}$ templates for the fits described in Sec. 7.1.2.

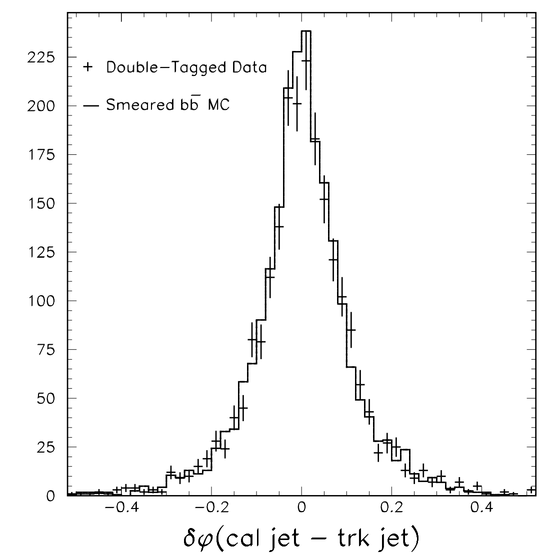


Figure B.2: Comparison of $\delta\phi$ in smeared $b\bar{b}$ Monte Carlo and double-tagged central data.

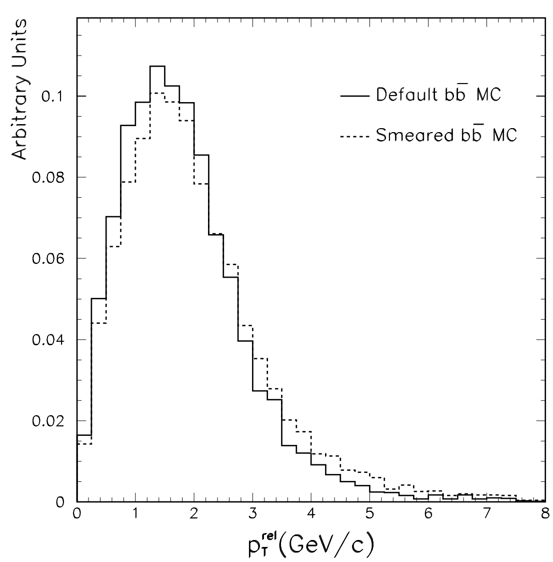


Figure B.3: Comparison of $p_T^{\rm rel}$ distributions for the default (solid) and smeared (dashed) central Monte Carlo samples.

# Bibliography


[1] H. Geiger and E. Marsden, Proc. Roy. Soc. **82**, 495 (1909).

[2] E. Rutherford, Phil. Mag. **21**, 669 (1911).

[3] R. W. McAllister and R. Hofstadter, Phys. Rev. **102**, 851 (1956).

[4] M. Breidenbach *et al.*, Phys. Rev. Lett. **23**, 935 (1969).

[5] J. D. Bjorken, Phys. Rev. **179**, 1547 (1969).

[6] R. P. Feynman, *Photon-Hadron Interactions*, 1st ed. (Benjamin, New York, 1972).

[7] R. N. Cahn and G. Goldhaber, *The Experimental Foundations of Particle Physics*, 1st ed. (Cambridge University Press, New York, 1989).

[8] M. Gell-Mann, Phys. Lett. **8**, 214 (1964).

[9] G. Zweig, CERN Preprint 8182/TH401 (unpublished).

[10] R. Brandelik *et al.*, Phys. Lett. B **86**, 243 (1979).

[11] G. Arnison *et al.*, Phys. Lett. B **122**, 103 (1983).

[12] M. Banner *et al.*, Phys. Lett. B **122**, 476 (1983).

[13] G. Arnison *et al.*, Phys. Lett. B **126**, 398 (1983).

[14] C. Albajar *et al.*, Phys. Lett. B **129**, 130 (1983).

[15] S. L. Glashow, Nucl. Phys. B **22**, 579 (1960).

[16] S. Weinberg, Phys. Rev. Lett. **19**, 1264 (1967).

[17] A. Salam, in *Elementary Particle Theory: Relativistic Groups and Analyticity*, edited by N. Svartholm (Almqvist and Wiksell, Stockholm, 1968), pp. 367–377.

[18] E. L. Berger, Phys. Rev. D **37**, 1810 (1988).

[19] M. Mangano, P. Nason, and G. Ridolfi, Nucl. Phys. B **373**, 295 (1992).

[20] S. Erhan *et al.*, Nucl. Instr. and Meth. A **333**, 101 (1993).

[21] A. Santoro *et al.*, Fermilab Note 660 (unpublished).

[22] H. Albrecht *et al.*, Phys. Lett. B **192**, 245 (1987).

[23] F. Paige and S. Protopopescu, Brookhaven Internal Report BNL-38034 (unpublished).

[24] H. L. Lai *et al.*, Phys. Rev. D **55**, 1280 (1997), and references therein.

[25] E. Eichten, K. Lane, and M. Peskin, Phys. Rev. Lett. **50**, 811 (1983).

[26] J. Huston *et al.*, hep-ph 9801444, (unpublished), submitted to Phys. Rev. D.

[27] J. Huston *et al.*, Phys. Rev. D **51**, 6139 (1995).

[28] L. Apanasevich *et al.*, hep-ex 9711017 (unpublished).

[29] C. Albajar *et al.*, Phys. Lett. B **213**, 405 (1988).

[30] C. Albajar *et al.*, Phys. Lett. B **256**, 121 (1991).

[31] C. Albajar *et al.*, Z. Phys. C **61**, 41 (1994).

[32] F. Abe *et al.*, Phys. Rev. D **45**, 1448 (1992).

[33] F. Abe *et al.*, Phys. Rev. Lett. **71**, 500 (1993).

[34] F. Abe *et al.*, Phys. Rev. Lett. **71**, 2396 (1993).

[35] F. Abe *et al.*, Phys. Rev. Lett. **75**, 1451 (1995).

[36] S. Abachi *et al.*, Phys. Rev. Lett. **74**, 2422 (1995).

[37] S. Abachi *et al.*, DØ Internal Note 3022, (unpublished), submitted to the 28$^{\text{th}}$ *International Conference on High Energy Physics*, Warsaw, Poland, July 25–31, 1996.

[38] S. Frixione *et al.*, hep-ph 9702287, (unpublished), to appear in *Heavy Flavours II*, A. J. Buras and M. Lindner, Advanced Series on Directions in High Energy Physics, World Scientific, Singapore.

[39] M. L. Mangano, hep-ph 9711337, (unpublished), presented at the International School of Physics "E. Fermi", Course CXXXVII, *Heavy Flavour Physics: A Probe of Nature's grand Design.*

[40] F. I. Olness, R. J. Scalise, and W. K. Tung, hep-ph 9712494 (unpublished).

[41] J. C. Collins, D. E. Soper, and G. Sterman, Nucl. Phys. B **263**, 37 (1986).

[42] R. K. Ellis, W. J. Stirling, and B. R. Webber, *QCD and Collider Physics*, 1st ed. (Cambridge University Press, New York, 1996).

[43] G. Sterman *et al.*, Rev. Mod. Phys. **67**, 157 (1995).

[44] T. C. Caso *et al.*, Euro. Phys. J. C **3**, 1 (1998).

[45] B. L. Combridge, Nucl. Phys. B **151**, 429 (1979).

[46] M. L. Mangano, CDF Internal Note 1783, (unpublished), code is available from the author.

[47] J. D. Bjorken, Phys. Rev. **185**, 1975 (1969).

[48] H. D. Politzer, Phys. Rep. **14**, 129 (1974).

[49] F. Halzen and A. D. Martin, *Quarks and Leptons*, 1st ed. (Wiley, New York, NY, USA, 1984).

[50] G. Altarelli and G. Parisi, Nucl. Phys. B **126**, 298 (1977).

[51] A. D. Martin, W. J. Stirling, and R. G. Roberts, Phys. Lett. B **354**, 155 (1995).

[52] M. Suzuki, Phys. Lett. B **71**, 139 (1977).

[53] J. D. Bjorken, Phys. Rev. D **17**, 171 (1978).

[54] C. Peterson *et al.*, Phys. Rev. D **27**, 105 (1983).

[55] J. Chrin, Z. Phys. C **36**, 163 (1987).

[56] D. Decamp *et al.*, Phys. Lett. B **244**, 551 (1990).

[57] L. W. Alvarez *et al.*, Rev. Sci. Instr. **26**, 111 (1955).

[58] E. A. Knapp *et al.*, Rev. Sci. Instr. **39**, 979 (1968).

[59] M. Harrison, in *Fourth Topical Workshop on Proton-Antiproton Collider Physics*, edited by H Hänni and J. Schacher (CERN, Geneva, 1984), p. 2638.

[60] S. van der Meer, CERN Internal Report ISR-PO/72-31 (unpublished).

[61] D. Mohl, in *Advances of Accelerator Physics and Technologies*, edited by H. Schopper (World Scientific, Singapore, 1993), pp. 358–429.

[62] F. Abe *et al.*, Phys. Rev. D **57**, 5382 (1998).

[63] R. Johnson, in *Frontiers of Particle Beams; Observation, Diagnosis, and Correction*, edited by M. Month and S. Turner (Springer-Verlag, Berlin, Germany / Heidelberg, Germany / London, England / etc., 1989), pp. 167–185.

[64] C. Grosso-Pilcher and S. White, Technical Report 550, FERMILAB (unpublished).

[65] F. Abe *et al.*, Nucl. Instr. and Meth. A **271**, 387 (1988).

[66] D. H. Perkins, *Introduction to High Energy Physics*, 3rd ed. (Addison-Wesley, Reading, MA, USA, 1987).

[67] D. Amidei *et al.*, Nucl. Instr. and Meth. A **350**, 73 (1994).

[68] P. Azzi *et al.*, Nucl. Instr. and Meth. A **360**, 137 (1995).

[69] F. Bedeschi *et al.*, Nucl. Instr. and Meth. A **268**, 51 (1988).

[70] H. Wenzel, CDF Internal Note 1790 (unpublished).

[71] R. C. Fernow, *Introduction to Experimental Particle Physics*, 1st ed. (Cambridge University Press, New York, 1986).

[72] L. Balka *et al.*, Nucl. Instr. and Meth. A **267**, 272 (1988).

[73] S. Bertolucci *et al.*, Nucl. Instr. and Meth. A **267**, 301 (1988).

[74] Y. Fukui *et al.*, Nucl. Instr. and Meth. A **267**, 280 (1988).

[75] G. Brandenburg *et al.*, Nucl. Instr. and Meth. A **267**, 257 (1988).

[76] S. Cihangir *et al.*, Nucl. Instr. and Meth. A **267**, 249 (1988).

[77] K. Byrum *et al.*, Nucl. Instr. and Meth. A **268**, 46 (1988).

[78] L. Zhang, Ph.D. thesis, University of Wisconsin, Madison, 1996.

[79] J. Skarha, Ph.D. thesis, University of Wisconsin, Madison, 1988.

[80] G. Ascoli *et al.*, Nucl. Instr. and Meth. A **268**, 33 (1988).

[81] J. Lewis *et al.*, CDF Internal Note 2858 (unpublished).

[82] D. Amidei *et al.*, Nucl. Instr. and Meth. A **269**, 51 (1988).

[83] G. W. Foster *et al.*, Nucl. Instr. and Meth. A **269**, 93 (1988).

[84] C. Grosso-Pilcher, CDF Internal Note 4350 (unpublished).

[85] H. Wiedemann, *Particle Accelerator Physics, Basic Principles and Linear Beam Dynamics* (Springer-Verlag, Berlin, Germany / Heidelberg, Germany / London, England / etc., 1993).

[86] A. A. Hahn, Conference Proceedings FERMILAB-CONF-97/188, (unpublished), presented at the *Particle Accelerator Conference PAC97*, Vancouver, Canada, May 12-16, 1997.

[87] A. Arbuzov *et al.*, Phys. Lett. B **383**, 238 (1996).

[88] G. M. Dallavalle, Acta. Phys. Pol. B **28**, 3 (1997), presented at the *Cracow Symposium on Radiative Corrections* (CRAD96), Cracow, Poland, August 1-5, 1996.

[89] S. Belforte *et al.*, CDF Internal Note 2361 (unpublished).

[90] M. M. Block and R. N. Cahn, Rev. Mod. Phys. **57**, 563 (1985).

[91] N. A. Amos *et al.*, Phys. Lett. B **243**, 158 (1990).

[92] F. Abe *et al.*, Phys. Rev. D **50**, 5518 (1994).

[93] F. Abe *et al.*, Phys. Rev. D **50**, 5535 (1994).

[94] F. Abe *et al.*, Phys. Rev. D **50**, 5550 (1994).

[95] N. A. Amos *et al.*, Phys. Rev. Lett. **68**, 2433 (1992).

[96] F. Abe *et al.*, Phys. Rev. Lett. **76**, 3070 (1994).

[97] M. Dell'Orso, CDF Internal Note 792 (unpublished).

[98] A. Beretvas *et al.*, CDF Internal Note 3418 (unpublished).

[99] J. Olsen, CDF Internal Note 4409 (unpublished).

[100] F. Bedeschi *et al.*, CDF Internal Note 1789 (unpublished).

[101] F. Bedeschi *et al.*, CDF Internal Note 2055 (unpublished).

[102] H. Wenzel, CDF Internal Note 4066 (unpublished).

[103] F. Bedeschi *et al.*, CDF Internal Note 2084 (unpublished).

[104] F. Abe *et al.*, Phys. Rev. D **47**, 4857 (1993).

[105] F. Abe *et al.*, Phys. Rev. Lett. **80**, 2767 (1998).

[106] N. Eddy, CDF Internal Note 3534 (unpublished).

[107] F. Abe *et al.*, Phys. Rev. D **50**, 2966 (1994).

[108] W. Yao, CDF Internal Note 2716 (unpublished).

[109] C. Miao and W. Yao, CDF Internal Note 3542 (unpublished).

[110] J. Bellinger *et al.*, CDF Internal Note 3410 (unpublished).

[111] F. Abe *et al.*, , to be submitted to Phys. Rev. Lett.

[112] S. Pappas, J. D. Lewis, and G. Michail, CDF Internal Note 4076 (unpublished).

[113] J. P. Done *et al.*, CDF Internal Note 4017 (unpublished).

[114] T. J. LeCompte and J. D. Lewis, CDF Internal Note 2588 (unpublished).

[115] A. Clark *et al.*, CDF Internal Note 2946 (unpublished).

[116] A. Warburton, CDF Internal Note 4139 (unpublished).

[117] A. Warburton and W. Trischuk, CDF Internal Note 4423 (unpublished).

[118] P. Avery, K. Read, and G. Trahern, Cornell Internal Report 212 (unpublished).

[119] T. R. M. Barnett *et al.*, Phys. Rev. D **54**, 1 (1996).

[120] H. Y. Chao *et al.*, CDF Internal Note 3715 (unpublished).

[121] K. Byrum, Ph.D. thesis, University of Wisconsin, Madison, 1992.

[122] S. Pappas, CDF Internal Note 3537 (unpublished).

[123] S. Pappas, Ph.D. thesis, Yale, 1998.

[124] T. J. LeCompte and W. Sakumoto, CDF Internal Note 3028 (unpublished).

[125] T. J. LeCompte and D. Glenzinski, CDF Internal Note 2985 (unpublished).

[126] K. Pitts and L. Qi, CDF Internal Note 4000 (unpublished).

[127] J. Lewis and K. T. Pitts, CDF Internal Note 3999 (unpublished).

[128] V. Barger, A. Stange, and R. Phillips, Phys. Rev. D **44**, 1987 (1991).

[129] K. Hoffman, Ph.D. thesis, Purdue University, 1998.

[130] M. Paulini *et al.*, CDF Internal Note 3757 (unpublished).

[131] F. Abe *et al.*, Phys. Rev. Lett. **76**, 3070 (1996).

[132] J. Olsen, CDF Internal Note 4105 (unpublished).

[133] G. Unal, CDF Internal Note 3563 (unpublished).

[134] S. Behrends, CDF Internal Note 3550 (unpublished).

[135] G. Alexander *et al.*, Phys. Lett. B **364**, 93 (1995).

[136] D. Buskulic *et al.*, Phys. Lett. B **357**, 699 (1995).

[137] M. Cacciari and M. Greco, Phys. Rev. D **55**, 7134 (1997).

[138] A. D. Martin, R. G. Roberts, and W. J. Stirling, Phys. Lett. B **387**, 419 (1996).

[139] A. D. Martin, R. G. Roberts, W. J. Stirling, and R. S. Thorne, Euro. Phys. J. C **4**, 463 (1998).

[140] F. Abe *et al.*, Phys. Rev. Lett. **77**, 438 (1996).

[141] S. Abachi *et al.*, Conference Report FERMILAB-CONF-96132-E (unpublished).